

Development of a Fully Coupled Zonal RANS/LES Method for the Simulation of a Turbulent Backward Facing Step Flow

Junoh Jung

Supervisors:

M.Sc. Marian Albers

M.Sc. Simon Loosen

Univ.-Prof. Dr.-Ing. Wolfgang Schröder

Aerodynamisches Institut Aachen

RWTH Aachen

A thesis submitted for the degree of
Master of Science Aerospace Engineering

July 2018

Abstract

The computational fluid dynamics(CFD) research at high Reynolds numbers is performed using different methods. Most of them are based on the Reynolds Averaged Navier-Stokes(RANS) equations as they are straightforward and computationally efficient or Large-Eddy Simulation(LES) when the flow requires a complex higher order turbulence modeling in order to achieve a reliable solution. In this study a method which combines the advantages of RANS and LES will be performed, a so-called zonal method. Zonal methods to connect two or more numerical domains of different mesh resolutions and different computational methods are embedded into the Zonal Flow Solver (ZFS) framework, a massive-parallel flow solver developed at the Aerodynamic Institute Aachen(AIA). A fully-coupled zonal simulation of a turbulent backward-facing step problem will be conducted, investigating the accuracy of the new method.

Contents

List of Figures	iii
List of Tables	v
Glossary	vii
1 Introduction	1
1.1 Background	1
1.2 Motivation	2
1.3 Structure of the work	3
2 Physical Description of Turbulence	5
2.1 Basic characteristics of turbulence	5
2.2 The scales of turbulent motion	6
2.2.1 The energy cascade	6
2.2.2 Kolmogorov hypotheses	6
2.3 Turbulent boundary layers	8
2.4 Turbulent flow over a backward facing step	10
3 Governing Equations and Mathematical Models	13
3.1 Equations of unsteady compressible flow	14
3.2 Turbulence modeling	18
3.2.1 Large-Eddy Simulation	19
3.2.2 Time-averaged Navier-Stokes equations	21
4 Numerical Methods	25
4.1 Spatial discretization of finite volume	25
4.2 Transformation to Curvilinear coordinates	26
4.3 Discretization of the inviscid fluxes	30
4.3.1 AUSM	30

CONTENTS

4.3.2	MUSCL scheme	32
4.4	Discretization of the viscous fluxes	33
4.5	Temporal discretization	34
4.6	Turbulence model for large-eddy simulations	35
4.7	Turbulence model for Reynolds-averaged Navier-Stokes equations	36
4.7.1	Spalart-Allmaras one-Equation turbulence model	36
4.8	Additional treatments for the simulation	38
4.8.1	Ghost-cell approach	38
4.8.2	Boundary conditions	39
5	Zonal RANS-LES Method	43
5.1	Zonal boundary conditions	44
5.1.1	First zonal interface	44
5.1.2	Second zonal interface	48
5.2	Zonal variable exchange	48
5.2.1	Trilinear interpolation	49
5.2.2	Grid connection for the zonal method	52
5.2.3	Zonal exchange	55
6	Results	59
6.1	Validation of the zonal method in a flat plate flow	59
6.1.1	Computational set-up	59
6.1.2	Comparison and analysis of the results	61
6.2	Space launcher simulation	74
6.2.1	Computational set-up	74
6.2.2	Validation of the Zonal RANS-LES method	78
7	Summary and conclusion	91
	References	93
A	Reference Values	95

List of Figures

1.1	European heavy-lift space launcher Ariane 5 ECA	2
2.1	Velocity profile of a turbulent boundary layer	9
2.2	Geometry of the backward facing step flow	10
2.3	Characteristics of the backward facing step flow	10
2.4	Schematic of cross-pumping and cross-flapping	11
4.1	Transformation between Cartesian and curvilinear coordinates	27
4.2	Active cells and ghost cells	38
5.1	Sketch of the zonal RANS-LES method	44
5.2	Overlapping zone between grids of different resolution	50
5.3	Isoparametric Mapping for the trilinear interpolation	52
5.4	Zonal grid connection in a complex case	53
5.5	Schematic diagram of the zonal grid connection	54
5.6	Schematic diagram of the zonal exchange procedure	56
5.7	Zonal exchange procedure	57
6.1	Zonal test case setup for the RANS-to-LES transition	60
6.2	Computational domain of the zonal test case	61
6.3	Streamwise development of the instantaneous velocity u	63
6.4	Plots of the instantaneous streamwise velocity component u at the stream- wise position $x/\delta_0 = 1.7$, where $Re_\theta = 1006$	64
6.5	Streamwise development of the Reynolds number Re_θ	65
6.6	Streamwise development of the skin friction coefficient c_f	67
6.7	Streamwise development of the shape factor H	68
6.8	Velocity u^+ at the position $x/\delta_0 = 1.7$, $Re_\theta = 1006$	69
6.9	Averaged streamwise velocity distribution at different streamwise positions	71
6.10	Reynolds stress components u_{rms}^+ , v_{rms}^+ , w_{rms}^+ , and $\langle uv \rangle^+$ at $Re_\theta = 1006$. .	72
6.11	Plot of the Reynolds stress components at the different streamwise points .	73
6.12	Geometery parameters of the investigated generic space launcher configuration	74

LIST OF FIGURES

6.13	Mach number field of the space launcher using the newly implemented zonal RANS-LES method with the turbulent backward facing step	75
6.14	Computational grid setup for the planar configuration	77
6.15	Instantaneous Mach number contour of the space launcher around the LES inflow	78
6.16	Distribution of the mean wall pressure coefficient	80
6.17	Streamwise development of the skin friction coefficient on the lower wall . .	81
6.18	Investigated streamwise different locations along the BFS in a Mach number field for the following plots	82
6.19	Distribution of velocity fluctuation component u'_{rms} in wall-normal direction at different streamwise positions	84
6.20	Distribution of velocity fluctuation component v'_{rms} in wall-normal direction at different streamwise positions	85
6.21	Distribution of velocity fluctuation component w'_{rms} in wall-normal direction at different streamwise positions	86
6.22	Streamwise development of the root-mean-square pressure fluctuation coefficient distribution on the lower wall	87
6.23	Distribution of the pressure fluctuation coefficient in wall-normal direction at the different streamwise positions	88
6.24	Development of the momentum thickness	89

List of Tables

2.1	Properties of the large and small scales in turbulent flow	6
6.1	Grid information of the zonal test case	59
6.2	Setup parameters of the zonal test case	62
6.3	Input parameters of the space launcher	75
6.4	Mesh size overview for the computational domain of the space launcher . .	76

GLOSSARY

Glossary

Roman Symbols

A_j^i	Cell interpolation coefficient in ξ -coordinate
a	Speed of sound
B_j^i	Cell interpolation coefficient in η -coordinate
C_j^i	Cell interpolation coefficient in ζ -coordinate
c_f	Skin friction coefficient
c_p	Specific heat capacity at constant pressure
c_p	Wall pressure coefficient
$c_{p,rms}$	Fluctuating pressure coefficient
c_v	Specific heat capacity at constant volume
d	Distance
E	Total specific energy per unit mass
\mathbf{E}	Flux vector in X-coordinate
e	Specific internal energy per unit mass
\mathbf{F}	Flux vector in Y-coordinate
f_l	Shape function
G	LES filter function
\mathbf{G}	Flux vector in Z-coordinate
\mathbf{H}	Flux vector
$\underline{\underline{I}}$	Identity tensor
J	Jacobian
k	Turbulent kinetic energy
k_j^i	Variables of the donor cells j on receiver cell i

GLOSSARY

L	Characteristic length
l	Length scale
l_k	Kolmogorov length
\mathbf{n}	Surface normal vector
N	Number of eddies inside virtual box
N_{cells}	Number of grid cells
O	Order of magnitude
\mathbf{P}	Vector of the primitive variables
p	Pressure
\mathbf{Q}	Vector of the conservative variables
q	Heat conduction term
R	Two-point correlation
R	Universal Gas Constant
S	Rate of strain tensor
S	Sutherland's constant
S_{ij}	Norm of the strain tensor
$S_{i,j}$	Cell surface
T	Temperature
t	Time
t_l	Time scale
\mathbf{U}	Contravariant velocity vector
u_l	characteristic velocity
\mathbf{v}	Flow velocity vector
u_τ	Friction velocity
V_i	Volume of the i-th cell
V_{virt}	Virtual box volume
\mathbf{x}	Vector of Cartesian coordinates
X	Mapping coordinate in ξ -coordinate
Y	Mapping coordinate in η -coordinate
Z	Mapping coordinate in ζ -coordinate

Greek Symbols

α_i	Runge-Kutta coefficients
β_i	Diffusive energy
ΔT	RANS time window
Δt	Physical time step
Δ	LES filter width
ΔS	Computational coordinate factor
$\Delta \mathbf{x}$	Distance
$\delta_{i,j}$	Kronecker delta
δ_0	99% boundary layer thickness
δ_1	Displacement thickness
θ	Momentum thickness
ϵ	Dissipation thickness
γ	Ratio of specific heats
κ	Exponential time averaging parameter
λ	Thermal conductivity
μ	Dynamic viscosity
∇	Nabla operator
ν	Kinematic viscosity
ν_t	Turbulent viscosity
Ω	Physical domain
ω	Turbulent frequency
Ψ	STG length scale parameter
ρ	Density
χ	Upwind coefficient
σ	viscous shear stress tensor
σ_{sp}	Sponge layer damping parameter
θ_m^i	Random operator
τ_w	Wall shear stress
ξ	Vector of computational space coordinates

Superscripts

'	Fluctuation
---	-------------

GLOSSARY

$+$	Nomalized wall quantity
$*$	Dimensional variable
$?$	Domainboundary
C	Convective part
p	Pressure part
T	Transpose
t	Time average
z	Spanwise average

Subscripts

0	Stagnation state
1/2	Cell surface
a	Active cell value
g	Ghost cell value
∞	Far field quantity
L/R	Left/right state
sgs	Subgrid-scale component
t	Turbulent quantity

Dimensional numbers

Ma	Mach number
Pr	Prandtl number
Re	Reynolds number
Re_{δ_0}	Boundary layer thickness Reynolds number
Re_{δ_1}	Displacement thickness Reynolds number
Re_{θ}	Momentum thickness Reynolds number

Abbreviations

AUSM	Advection Upstream Splitting Method
BFS	Backward facing step
CFD	Computational Fluid Dynamics
CPU	Central Processing Unit
DMD	Dynamic mode decomposition
DNS	Direct Numerical Simulation

LES	Large-Eddy Simulation
MCV	Modified Cell-Vertex
MOL	Method of lines
MUSCL	Monotone Upstream-centered Scheme for Conservation Laws
MILES	Monotonically Integrated Large-Eddy Simulation
MPI	Message Passing Interface
NSE	Navier-Stokes Equations
RANS	Reynolds-Averaged Navier-Stokes equations
RHE	Right Hand Side
RMS	Root Mean Square
RSTG	Reformulated synthetic Turbulence Generation
SA	Sparlart-Allmars
SEM	Synthetic eddy method
SGS	Subgrid-Scale
STG	Synthetic Turbulence Generation
TFS	The flow solver
ZFS	Zonal flow solver

GLOSSARY

Introduction

1.1 Background

Turbulent flows are abundant in natural phenomena, showcased as random and irregular, attracting the keen eye of many scientists. Ever since the first experiment of Osborne Reynolds in 1883 [1], the behavior of turbulent flow has attracted scientific attention. Moreover, in modern society, turbulent flows can be observed in almost all technical applications, for example, airplane aerodynamics, jet engines, cars, and gas turbines. Engineers are mainly interested in resolving the fluid-dynamical drawbacks in order to operate these machines more efficiently. This is done by computing quantitative values such as drag, noise and finding measures to decrease them. Experimental analysis has played an important role in fluid dynamics as one of the methods to investigate the turbulence. However, an experimental approach is restricted by the required equipment, scaling problems and enormous operating costs. Alternatively, theoretical methods have been successfully applied to certain flow types, but are limited to simple linear problems. For these reasons, computational fluid dynamics (CFD) has grown constantly over the years as an alternative of investigating turbulent flows, since the 1980s [2]. CFD is a field of physics that employs the numerical solution of the governing equations describing the fluid motion.

The numerical methods to simulate fluid flows using CFD have drastically progressed over the decades. The development of CFD has been characterized by a continual drive to higher fidelity and more accurate methods. From the 1970s to the 1990s, this began with panel methods, proceeding to linearized and nonlinear potential flow methods, inviscid flow (Euler) methods, and culminated with Reynolds-averaged Navier-Stokes (RANS) methods [3]. Direct numerical simulation (DNS) approach was then developed such that Navier-Stokes equations are numerically solved without a turbulence model. That is, all space and time scales of the turbulence are resolved. Therefore, DNS is computationally

1. INTRODUCTION

extremely expensive, even at low Reynolds numbers. Recently, more appropriate methods have been developed in consideration of the computational costs. Using a turbulence model, RANS simulation and large-eddy simulations (LES) are computationally efficient and result in accurate solutions. Hence, RANS and LES are often applied to investigate turbulent flows in industrial applications.

1.2 Motivation

To illustrate the benefits of CFD, the first flight accident of the European heavy-lift space launcher ARIANE 5 ECA manufactured by the European Space Agency (ESA) on 12 December 2002 can be considered. The main reason for the accident was a malfunction of the new VULCAIN-2 main engine, which resulted in aerodynamic problems within a complex turbulent flow. This specific scenario could not be investigated on the ground in wind tunnel tests, since undesirable interactions with the model supports take place locally at supersonic speeds due to the induced shock and expansion waves [4]. Furthermore, the experimental testing of an axisymmetric model is not straightforward, and as a result, the flow cannot be replicated in practice. For these reasons, a numerical analysis had to be performed, because all possible conditions could be investigated and the model will not be obstructed or altered by the presence of supports, as in physical testing.

Many different numerical methods can be utilized to simulate the flow field around a space launcher. One of the methods, DNS, is intractable for investigating turbulence at high Reynolds numbers, due to the excessive number of required grid points, computational power and time to resolve all temporal and spatial scales of motions. Therefore, straightforward and computationally efficient RANS and LES methods are most often used to solve flow problems at high Reynolds numbers. These methods are also used for optimization and for cases where it is difficult to obtain experimental data. However, if the flow cannot reach an equilibrium state, for instance, when the streamlines are extremely curved, or when strong adverse pressure gradients, detachment, or transition exist, the fidelity of the results of RANS simulations will be reduced [5]. Despite many attempts to improve RANS in non-equilibrium flows, an universal solution has not yet been found. In contrast to RANS simulations, LES models the dissipative scales of turbulence using the assumption of isotropy in small scale motions and the eddies associated with transporting energy to smaller scales are then resolved.



Figure 1.1: European heavy-lift space launcher Ariane 5 ECA [ESA]

Thus, LES is mainly performed for non-equilibrium flows, since it can be used to resolve the relevant turbulent scales [2].

To exploit the advantages of both methods and enhance the computational efficiency, when the turbulent flow problems are numerically solved, the region containing turbulent equilibrium should be solved using a RANS simulation, while the regions that require high-fidelity should be solved by LES. Using the example of the space launcher at high Reynolds numbers, it requires a very large control volume, but only a small region in the vicinity of the launcher nozzle is resolved by LES, whereas the major part of the launcher is simulated using RANS. Thus, RANS and LES can be implemented into one flow domain with lower computational cost and a physically reliable solution. This combined method is called zonal RANS-LES method and this approach is used in this work.

1.3 Structure of the work

The zonal RANS-LES method is embedded into the zonal flow solver (ZFS), which is a massive-parallel flow solver developed at the Aerodynamic Institute Aachen (AIA). In previous works a coupled zonal RANS-LES method was developed in the ZFS environment, however, only for grids that match perfectly at the zonal interface. In this work zonal interface is extended for overset meshes, i.e., meshes that overlap each other in every possible way. In addition, the method is developed for massive parallel simulations with multiple zonal interfaces. Finally, the zonal RANS-LES method is applied to a zero-pressure gradient turbulent boundary layer flow and a space launcher simulation and solution parameters are compared to the reliable method (DNS, pure RANS and pure LES) and the original solver (TFS).

The main works in this thesis are listed as follows.

1. Development of a method for the parallel connection of overset meshes.
2. Set up of a suitable interpolation procedure for the interpolation of variables at overset boundaries.
3. Application of the new zonal method to a zero-pressure gradient simulation.
4. Application of the new zonal method to space launcher simulation.

To complete the thesis, the work is organized into seven chapters. After the introduction, a short physical description of turbulence is presented in chapter two. Chapter three

1. INTRODUCTION

presents the governing equations and the mathematical models of the fluid flow. Subsequently, the numerical methods are introduced to solve the mathematical formulations in chapter four. In chapter five, the zonal RANS-LES method is introduced. Then, the validation of the zonal RANS-LES method is presented, applying to a flat plate flow for the zero-pressure gradient simulation and a space launcher simulation. Finally, in chapter seven planned future work will be discussed after a summation of the conclusions.

2

Physical Description of Turbulence

2.1 Basic characteristics of turbulence

The most important parameter for the characterization of viscous flows is the Reynolds number, defined as

$$Re = \frac{uL}{\nu} \quad (2.1)$$

where u is the velocity of the fluid with respect to the object, L is a characteristic linear dimension, and ν is the kinematic viscosity of the fluid. Whether a flow is laminar or turbulent depends on whether the viscosity or the flow inertia is more influential, i.e., for low Reynolds numbers most flows show a laminar behavior, whereas above certain values turbulent flow develops. This always depends on the characteristic length and the specific test case, giving a few examples, such that a transition to turbulence is at Reynolds number of 2,300 for internal flow, and 5-600,000 for external flow.

The basic characteristics of a turbulent flow are irregularity, three-dimensionality, diffusivity, high vorticity levels, dissipation, and high Reynolds number. Therefore, turbulent flows require statistical analysis since an intricate random problem cannot be solved through a deterministic approach. The diffusivity is also a critical characteristic as it causes drastic mixing and increased rates of momentum, heat and mass transfer in flows. Furthermore, turbulent flows show in high levels of fluctuating vorticity, which induces fluid particle rotation or spin. Another important feature of turbulence is dissipation. Viscous shear stresses cause deformation, increasing the internal energy of the fluid at the expense of kinetic energy. The deformed flow is required to recover the viscous losses, because if there is no additional energy, the turbulence will dissipate.

If all statistics are invariant under a shift in time and a position, the flow is stationary and homogeneous, respectively. Isotropic turbulence is characterized by an invariance of the statistic variables to rotations and reflections.

2. PHYSICAL DESCRIPTION OF TURBULENCE

2.2 The scales of turbulent motion

The turbulent length scales vary from the width of the flow domain down to molecular size. As the Reynolds number rises, the length scales of the turbulent motions decrease. Furthermore, the turbulent kinetic energy, i.e., the kinetic energy of the turbulent fluctuations, is related to the Reynolds stress tensor which is important term in the governing equations (see chap. 3). Therefore, this section presents how the turbulent energy is distributed over the wide-ranging length scales. Two theories (the energy cascade and the Kolmogorov hypotheses) are briefly introduced.

2.2.1 The energy cascade

One of the most important concepts in turbulent flow is an eddy, which is defined as a swirling structure of fluid, with various length scales in turbulent flows. The parameters representing the size of an eddy are a length scale l , a characteristic velocity u_l , and a timescale t_l . Richardson (1922) introduced the energy cascade, which explains that large eddies at the largest scales of turbulent motions obtain the kinetic energy via velocity gradient due to shear. This energy is then transferred to the smaller scales. The kinetic energy exchange is also continuously performed at the smallest scales and eventually the Re_l becomes sufficiently small such that the motions of eddies is stabilized. At the smallest scales, the kinetic energy is dissipated through viscous action for the last process.

Large scales	Small scales
generated by the mean flow	produced by large eddies
strongly affected by boundary configurations	universal
ordered (coherent structures)	random
inhomogeneous and anisotropic	homogeneous and isotropic
long-living	short-living
high energy content	low energy content
diffusive	dissipative
difficult to model	easier to model
universal model impossible	universal model more probable

Table 2.1: Properties of the large and small scales in turbulent flow [6].

2.2.2 Kolmogorov hypotheses

Kolmogorov's hypotheses provide explanations to fundamental questions regarding turbulent flows such as the size of the smallest eddies or the relation of time-, length-, and velocity scales [7]. However, two assumptions are necessary to formulate the Kolmogorov hypotheses. First, the turbulent motion at small scales is statistically isotropic at high

2.2 The scales of turbulent motion

Reynolds numbers. Second, the statistics of the motions at the small scales are assumed to be universal, depending on only the kinematic viscosity and the dissipation rate. Kolmogorov explained that loss of all information about the geometry of the large eddies occurs, and even the directions of large eddies becomes also unknown, transferring the energy of large scales to smaller scales [8]. That is, the information about the energy of large scales is no more available in small scales motions, therefore, it is concluded that the statistics of the small-scale motions are almost universal. This can be applied in high Reynolds number flows. The kinetic energy of the eddies at the smallest scales are consumed by viscous action. To describe the physical properties of the large scale motions, the integral scale l_0 is introduced, defined by the mean correlation distance R between two points in a turbulent flow [9]. That is, the integral length scale l_0 is defined as

$$l_0 = \int_0^\infty R(\mathbf{x}, r) dx. \quad (2.2)$$

where x is a position vector in the flow field. The smallest length scale of eddies l_k at the local flow Reynolds number is called the Kolmogorov scale, determined by

$$l_k = \left(\frac{\nu^3}{\epsilon} \right)^{1/4} \quad (2.3)$$

where ϵ is the dissipation rate and ν is the kinematic viscosity. By means of the Kolmogorov scale, a time- and a velocity scale for the smallest eddies can be determined by

$$t_{l_k} = \left(\frac{\nu}{\epsilon} \right)^{1/2} \quad \text{and} \quad u_{l_k} = (\epsilon \nu)^{1/4}, \quad (2.4)$$

where the dissipation rate ϵ is given by

$$\epsilon = u'^3 t_0, \quad (2.5)$$

2. PHYSICAL DESCRIPTION OF TURBULENCE

where u' denotes the velocity fluctuations. The relation between the smallest and the largest scales of eddies is obtained by Kolmogorov scale equations, such that

$$\begin{aligned}\frac{l_k}{l_0} &\sim Re_0^{-3/4} \\ \frac{t_{l_k}}{t_0} &\sim Re_0^{-1/2} \\ \frac{u_{l_k}}{u'} &\sim Re_0^{-1/4}\end{aligned}\tag{2.6}$$

where Re_0 denotes the Reynolds number of the largest eddies.

In addition, the number of grid-points N is an important factor, representing the computational costs for the computation of three dimensional flows, which can be estimated by $N \approx Re_0^{9/4}$, i.e., it grows more than square with the Reynolds number. Therefore, DNS resolving the Kolmogorov scales is practically impossible at high Reynolds numbers. In contrast, methods using a spatial filtering or time averaged formulation of the governing equations, i.e., LES and RANS can reduce the number of grid points by resolving only large scales and modeling the small scales.

2.3 Turbulent boundary layers

a boundary layer is an important concept and a fluid layer, which is required to be physically differently dealt with in immediate vicinity of a bounding surface, i.e., around region where a viscous effect is governed. Depending on Reynolds number of the flow, the boundary layer of fluid can be distinguished, such that a laminar boundary layer and a turbulent boundary layer.

The turbulent boundary layers can be divided into two different characteristic regions (see Fig. ??). The inner layer near the wall is dominated by viscous forces, whereas the outer layer, or logarithmic layer, is dominated by the turbulent stresses. The outer layer possesses outer length scales, while the inner layer is composed of inner length scales. In the inner layer a linear velocity distribution exists. This region is called the linear sub-layer. The inner-layer region located further from the wall is less affected by the viscosity, yielding the logarithmic law of the wall [2]. This region is also called log-law, such that

$$u^+ = \frac{1}{\kappa} \ln(y^+) + B.\tag{2.7}$$

The log law is used as a universal curve for the inner region of the flat plate turbulent boundary layer.

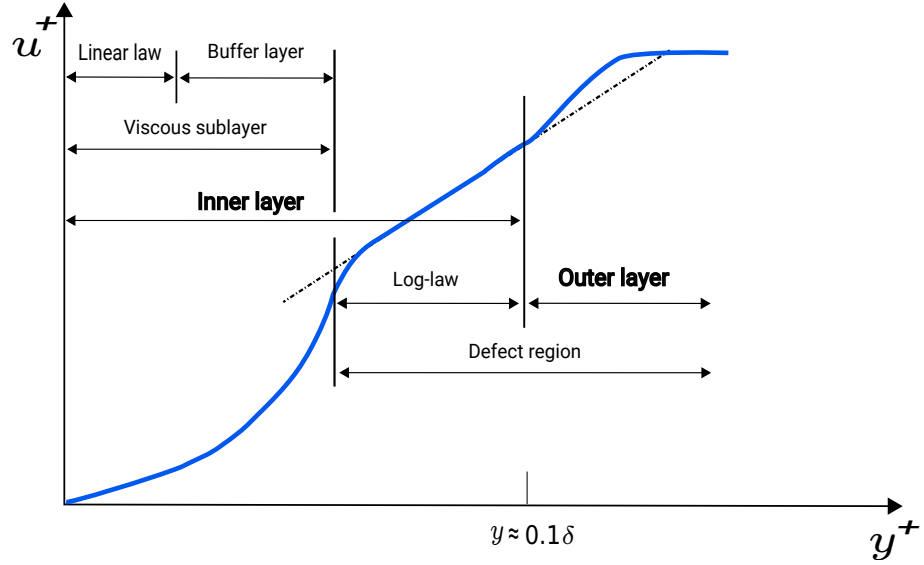


Figure 2.1: Velocity profile of a turbulent boundary layer using logarithmic scaling [10]

2. PHYSICAL DESCRIPTION OF TURBULENCE

2.4 Turbulent flow over a backward facing step

The turbulent flow over a backward facing step (BFS) (see Fig. 2.2) is a common used case to evaluate turbulence models for separated flows. The fundamental characteristics of the BFS flow are briefly introduced in this section.

The wake flow behind the BFS is divided into three regions, i.e., the shear layer region, the separation bubble or the recirculation zone, and the reattachment zone (see Fig. 2.3). As the flow develops, the size of the shear layer increases and an amalgamation of turbulent structures occurs. The area where the shear layer grows is called the shear layer region. The turbulent structures in the shear layer remove irrotational fluid from the non-turbulent region outside of the shear layer [11]. This results in the creation of a low velocity recirculation region in the separation bubble which is positioned between the shear layer zone and the wall. This zone is composed of a primary vortex taking up most of the area and a secondary vortex near the step edge (see Fig. 2.3). The secondary vortex rotates contrary to the primary vortex. Due to the favorable pressure gradient caused by the fluid entrainment [11], the shear layer moves towards the wall. In the first part of the shear layer the time averaged dividing streamline is not

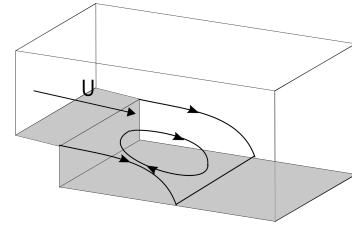


Figure 2.2: Geometry of the backward facing step flow.

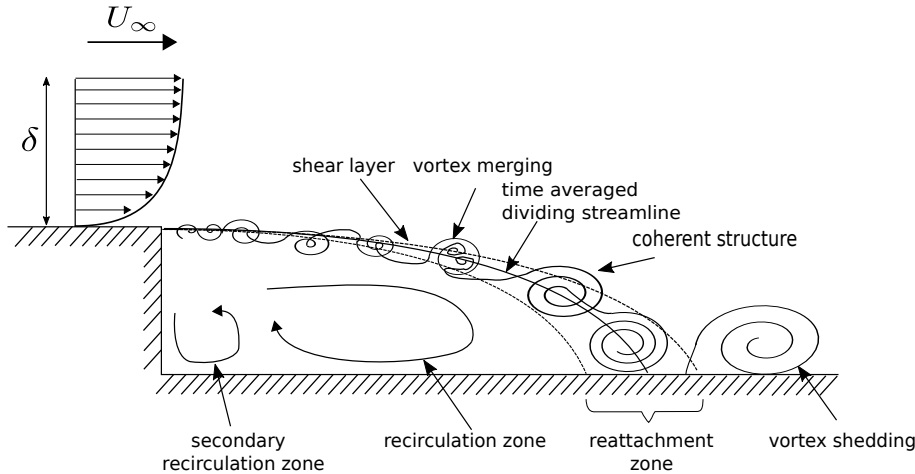


Figure 2.3: Characteristics of the backward facing step flow [12].

strongly curved, but almost seems linear. Furthermore, the free shear layer is so slender that the influence of the wall is not significant. That is, the flow behavior resembles a plane mixing-layer, yielding a good agreement between the growth-rate of the reattaching shear layer and a plane mixing-layer [13].

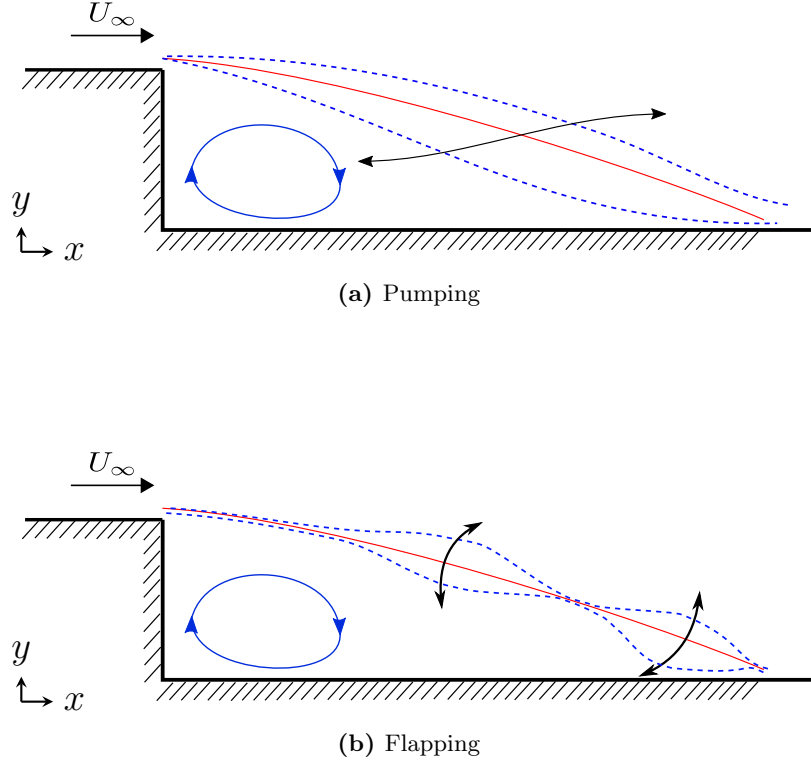


Figure 2.4: Schematic of cross-pumping and cross-flapping [18].

The distance between the edge of the step and the reattachment position is referred as the reattachment length. In previous studies [13, 14, 15, 16, 17], it is proven that the reattachment length is an important parameter when investigating the wake flow characteristics of the BFS flow. The reattachment length is in an unsteady state, due to the inherent oscillatory motion of the shear layer, which is called "flapping".

In the analysis of the three-dimensional shape of the dynamic mode decomposition (DMD) modes [18], an oscillating longitudinal pumping motion in the streamwise direction and the formation of wedge-shaped structures in the spanwise direction with a wave length of approximately two step heights is detected. It is denoted as cross-pumping (see Fig. 2.4a). In addition, there is a second higher frequency motion characterized by an undulating motion of the shear layer. This second mode denoted as cross-flapping also exhibits a pronounced variation in the spanwise direction [18] (see Fig. 2.4b). Both wake flow modes lead to a prominent nearly-periodical variation in the spanwise direction [18]. This is called the three-dimensional effect in this work.

In this work, the flow around a planar space launcher characterized by a BFS at the end of the main body is investigated using a zonal RANS-LES method (see chap. 5). A brief analysis is performed on the main flow features.

2. PHYSICAL DESCRIPTION OF TURBULENCE

3

Governing Equations and Mathematical Models

Mathematical models should be essentially derived for a numerical solution of the fluid flow. Assuming continuum flow, unsteady compressible viscous fluid flow is described by the Navier-Stokes equations. The continuum flow is characterized by small Knudsen numbers $Kn = \frac{l_{mol}}{l_k}$ [6], i.e., $Kn \ll 1$. Thus, it is valid when the molecular length scale l_{mol} is negligibly small, while the characteristic length scale l_k remains relatively large. This ratio can be approximated as

$$\frac{l_{mol}}{l_k} \sim \frac{Ma_t}{Re_t^{1/4}}. \quad (3.1)$$

In this work, since low Mach number flow at moderate Reynolds number is used, the Kn number is very small, justifying the continuum flow assumption.

The Navier-Stokes equations (NSE) are the governing equations in continuum flow. Additional equations are specified to close the system of equations. Furthermore, non-dimensionalization is used to reduce the number of physical and geometrical parameters of the NSE. Subsequently, spatial filtering for the large-eddy simulation (LES) approach and time averaging for the Reynolds-Averaged Navier Stokes (RANS) approach are introduced for the turbulence modeling.

3. GOVERNING EQUATIONS AND MATHEMATICAL MODELS

3.1 Equations of unsteady compressible flow

The Navier-Stokes equations are the governing equations for the conservation of mass, momentum, and energy under the assumption of a continuum flow. The governing equations that mathematically describe the dynamics of an unsteady, viscous and compressible turbulent flow are transformed to a non-dimensional form to normalize the different units and scales. In order to non-dimensionalize, stagnation point reference values are used (see Appendix A). As a result, the governing equations of unsteady compressible flow without external forces in integral form are given by

$$\int_{\tau} \frac{\partial \mathbf{Q}}{\partial t} d\tau + \oint_S \mathbf{H} \cdot \mathbf{n} dS = 0 \quad \text{with} \quad \mathbf{Q} = (\rho, \rho \mathbf{v}, \rho e)^T, \quad (3.2)$$

where τ is a finite control volume and S is the surface of the finite control volume. ρ is the density, $\rho \mathbf{v}$ is the specific momentum, and $\rho e = \rho(\epsilon + \frac{1}{2} \mathbf{v}^2)$ is the specific energy, which is composed of the inner energy and the kinetic energy. The vector of the velocity components in the Cartesian directions is denoted by $\mathbf{v} = (u, v, w)^T$. That is, the temporal change of the dimensionless conservation quantities \mathbf{Q} in a control volume τ and the generalized flux \mathbf{H} (fluxes, stresses) normal to the surface S are balanced due to non-external forces. By means of the Gauss theorem the integral form of the NSE is transformed into the partial differential form, yielding

$$\frac{\partial \mathbf{Q}}{\partial t} + \nabla \cdot \mathbf{H} = 0 \quad (3.3)$$

where the operator ∇ is the partial derivative in the Cartesian coordinates. Expanding the flux terms for the Cartesian components, eq. 3.3 becomes

$$\frac{\partial \mathbf{Q}}{\partial t} + \frac{\partial \mathbf{E}}{\partial x} + \frac{\partial \mathbf{F}}{\partial y} + \frac{\partial \mathbf{G}}{\partial z} = 0 \quad (3.4)$$

where \mathbf{E} , \mathbf{F} , and \mathbf{G} denote the flux vector in Cartesian coordinates. The flux vector \mathbf{H} can be divided into the inviscid flux \mathbf{H}_{inv} and the viscous flux \mathbf{H}_{vis} as each has different mathematical characteristic behavior, which needs to be dealt with in different ways. The inviscid fluxes have real characteristics, i.e., they exhibit hyperbolic character, whereas the viscous 4 fluxes have complex characteristics, i.e., they have an elliptic nature. Therefore,

3.1 Equations of unsteady compressible flow

the flux vector can be expressed as

$$\mathbf{H} = \mathbf{H}_{inv} - \mathbf{H}_{vis} = \begin{pmatrix} \rho \mathbf{v} \\ \rho \mathbf{v} \mathbf{v} + p \\ \rho \mathbf{v} (e + \frac{p}{\rho}) \end{pmatrix} - \frac{1}{Re_{ref}} \begin{pmatrix} 0 \\ \sigma \\ \sigma \cdot \mathbf{v} + \mathbf{q} \end{pmatrix}, \quad (3.5)$$

where \mathbf{q} is the heat flux and σ is the viscous shear stress tensor. That is, the equation 3.3 can be rewritten as

$$\frac{\partial \mathbf{Q}}{\partial t} + \nabla \cdot \mathbf{H}_{inv} = \nabla \cdot \mathbf{H}_{vis}. \quad (3.6)$$

The inviscid flux and viscous flux vectors are expressed for each Cartesian direction, such that

$$\mathbf{E}_{inv} = \begin{pmatrix} \rho u \\ \rho u u + p \\ \rho u v \\ \rho u w \\ u(\rho e + p) \end{pmatrix}, \quad \mathbf{E}_{vis} = \frac{1}{Re_{ref}} \begin{pmatrix} 0 \\ \sigma_{xx} \\ \sigma_{xy} \\ \sigma_{xz} \\ u\sigma_{xx} + v\sigma_{xy} + w\sigma_{xz} + q_x \end{pmatrix}, \quad (3.7)$$

$$\mathbf{F}_{inv} = \begin{pmatrix} \rho v \\ \rho v u \\ \rho v v + p \\ \rho v w \\ v(\rho e + p) \end{pmatrix}, \quad \mathbf{F}_{vis} = \frac{1}{Re_{ref}} \begin{pmatrix} 0 \\ \sigma_{yx} \\ \sigma_{yy} \\ \sigma_{yz} \\ v\sigma_{yx} + v\sigma_{yy} + w\sigma_{yz} + q_y \end{pmatrix}, \quad (3.8)$$

$$\mathbf{G}_{inv} = \begin{pmatrix} \rho w \\ \rho w u \\ \rho w v \\ \rho w w + p \\ w(\rho e + p) \end{pmatrix}, \quad \mathbf{G}_{vis} = \frac{1}{Re_{ref}} \begin{pmatrix} 0 \\ \sigma_{zx} \\ \sigma_{zy} \\ \sigma_{zz} \\ w\sigma_{zx} + v\sigma_{zy} + w\sigma_{zz} + q_z \end{pmatrix}. \quad (3.9)$$

The viscous shear stress tensor σ for a Newtonian fluid is given by

$$\sigma = \mu \left(\frac{\partial u_i}{\partial x_j} + \frac{\partial u_j}{\partial x_i} \right) - \frac{2}{3} \mu \delta_{ij} \frac{\partial u_i}{\partial x_j}, \quad (3.10)$$

where μ is the dynamic viscosity of the fluid. The symbol δ_{ij} denotes the Kronecker delta,

3. GOVERNING EQUATIONS AND MATHEMATICAL MODELS

such that

$$\delta_{ij} = \begin{cases} 0, & \text{if } i \neq j \\ 1, & \text{if } i = j. \end{cases} \quad (3.11)$$

The dynamic viscosity μ can be approximated by means of the Sutherland's law [19] under the assumption of a constant Prandtl number ($Pr = 0.72$) for air and is given by

$$\mu = \mu_{ref} \left(\frac{T}{T_{ref}} \right)^{\frac{T_{ref} + S}{T + S}}, \quad (3.12)$$

where S is the Sutherland constant ($S = 111K$ for a gas at moderate temperature). Furthermore, the heat flux is given by Fourier's law, such that

$$\mathbf{q} = \lambda \nabla T, \quad (3.13)$$

where λ is the thermal conductivity coefficient. However, the system of the equations (eq. 3.6) is not yet closed, as seven independent variables (ρ , $\mathbf{v}(u, v, w)$, e , T , and p) exist in the system of equations but only five independent equations are given by

$$\frac{\partial}{\partial t} \rho + \frac{\partial}{\partial x_i} (\rho u) + \frac{\partial}{\partial y} (\rho v) + \frac{\partial}{\partial z} (\rho w) = 0, \quad (3.14)$$

$$\frac{\partial}{\partial t} \rho u + \frac{\partial}{\partial x} (\rho u^2 + p + \sigma_{xx}) + \frac{\partial}{\partial y} (\rho uv + \sigma_{xy}) + \frac{\partial}{\partial z} (\rho uw + \sigma_{xz}) = 0, \quad (3.15)$$

$$\frac{\partial}{\partial t} \rho v + \frac{\partial}{\partial x} (\rho uv + \sigma_{xy}) + \frac{\partial}{\partial y} (\rho v^2 + p + \sigma_{yy}) + \frac{\partial}{\partial z} (\rho vw + \sigma_{yz}) = 0, \quad (3.16)$$

$$\frac{\partial}{\partial t} \rho w + \frac{\partial}{\partial x} (\rho uw + \sigma_{xz}) + \frac{\partial}{\partial y} (\rho vw + \sigma_{yz}) + \frac{\partial}{\partial z} (\rho w^2 + p + \sigma_{zz}) = 0, \quad (3.17)$$

3.1 Equations of unsteady compressible flow

$$\frac{\partial}{\partial t}\rho e + \frac{\partial}{\partial x}(L) + \frac{\partial}{\partial y}(M) + \frac{\partial}{\partial z}(N) = 0 \quad (3.18)$$

$$\begin{aligned} \text{with } L &= \rho u e + u p + u \sigma_{xx} + v \sigma_{xy} + w \sigma_{xz} + q_x, \\ M &= \rho v e + v p + u \sigma_{yx} + v \sigma_{yy} + w \sigma_{yz} + q_y, \\ N &= \rho w e + w p + u \sigma_{zx} + v \sigma_{zy} + w \sigma_{zz} + q_z. \end{aligned}$$

That is, additional relations are required to solve this system. Thermodynamic relations are cast into the system of the differential equations, assuming a thermal and calorically perfect gas. The ideal gas law is given by

$$p = \rho R T \quad (3.19)$$

with the gas constant per unit mass $R = c_p - c_v$ and the specific heats c_p and c_v at constant pressure and constant volume, respectively. Furthermore, the caloric state equation must be considered to relate temperature T and inner energy ϵ , such that

$$\epsilon = c_v T \quad \text{with} \quad c_v = \frac{R}{\gamma - 1}. \quad (3.20)$$

By means of the total specific energy equation $\rho e = \rho(\epsilon + \frac{1}{2}\mathbf{v}^2)$, the ideal gas law (Eq. 3.19), and the caloric state equation (Eq. 3.20), the relation between pressure p and the specific energy e becomes

$$p = (\gamma - 1) \left(\rho e - \frac{1}{2} \rho \mathbf{v}^2 \right). \quad (3.21)$$

The governing equations have to be transformed into dimensionless form (see Appendix A).

3. GOVERNING EQUATIONS AND MATHEMATICAL MODELS

Thus, viscous flux in the x-direction becomes

$$\mathbf{E}_{vis} = \frac{1}{Re_0} \begin{pmatrix} 0 \\ \sigma_{xx} \\ \sigma_{xy} \\ \sigma_{xz} \\ u\sigma_{xx} + v\sigma_{xy} + w\sigma_{xz} + q_x \end{pmatrix}. \quad (3.22)$$

The dimensionless heat flux (Eq. 3.13) is expressed by

$$\mathbf{q} = -\frac{\lambda}{(\gamma - 1)Pr_0} \nabla T, \quad (3.23)$$

and Sutherland's law (Eq. 3.12) can be written by

$$\mu = \mu_0 \left(\frac{T}{T_0} \right) \frac{T_0 + S}{T + S}. \quad (3.24)$$

Finally, the dimensionless governing equations are obtained and used for turbulence modeling, as described in next sections.

3.2 Turbulence modeling

The governing equations, which were derived in the above section are modeled to solve for the dynamics of almost all flow cases, laminar and turbulent, alike. In order to obtain accurate results, all spatial and temporal scales must be numerically discretized. The number of grid points N for resolution of all scales in a turbulent flow is proportional to $Re_\infty^{9/4}$, where the Reynolds number is based on the free stream variables and a characteristic length scale l_0 . DNS resolves all length scales and is not appropriate for analyzing the turbulent flow at high Reynolds numbers since the computational cost is extremely high and so DNS can be used only in a restricted region of the flow. Therefore, more efficient

methods, i.e., LES and RANS, were developed to avoid resolving the smallest scales, and instead model the dynamics of the motion in order to save computational effort. These two methods are explained in the following subsections.

3.2.1 Large-Eddy Simulation

As mentioned above, DNS is not suitable for investigating flows at high Reynolds numbers. The computational effort of DNS is consumed by the adequate resolution of the smallest and dissipative motions, while the energy and anisotropy are primarily involved in the larger scale motions. However, in the LES method the dynamics of the larger scale motion are computed explicitly, whereas the smaller scales are modeled. That is, the enormous expense of computation can be avoided via modeling of the subgrid-scale motions.

First, the unsteady flow variable $\Omega(\mathbf{x}, t)$ at the position $\mathbf{x} (x, y, z)$ is decomposed into a resolved component $\bar{\Omega}(\mathbf{x}, t)$ (large scales) and an unresolved component $\Omega'(\mathbf{x}, t)$ (subgrid-scale, SGS or residual), such that

$$\Omega(\mathbf{x}, t) = \bar{\Omega}(\mathbf{x}, t) + \Omega'(\mathbf{x}, t). \quad (3.25)$$

Furthermore, the resolved portion $\bar{\Omega}(\mathbf{x}, t)$ can be determined by the method of Leonard [20], such that

$$\bar{\Omega}(\mathbf{x}, t) = \int_{\tau} G(\mathbf{x} - \mathbf{y}, \Delta(\mathbf{x})) f(\mathbf{x} - \mathbf{y}, t) d^3 y, \quad (3.26)$$

where G is a filter function and Δ is a filter width which is defined as the step size of the computational grid. The normalization of the filter function G is performed by

$$\int_{\tau} G(\mathbf{x} - \mathbf{y}, \Delta(\mathbf{x})) d^3 y = 1. \quad (3.27)$$

Density weighted Favre averaging [21][22] is introduced to avoid additional correlations between flow quantities in the continuity equation, such that

$$\tilde{\Omega}(\mathbf{x}, t) = \frac{\overline{\rho\Omega}}{\bar{\rho}} = \frac{1}{\bar{\rho}} \int_{\tau} G(\mathbf{x} - \mathbf{y}, \Delta(\mathbf{x})) \rho(\mathbf{x} - \mathbf{y}, t) \Omega(\mathbf{x} - \mathbf{y}, t) d^3 y, \quad (3.28)$$

3. GOVERNING EQUATIONS AND MATHEMATICAL MODELS

where $(\tilde{\cdot})$ denotes the density weighted Favre filtering. Applying density weighted filtering, eq. 3.25 can be expressed as

$$\Omega(\mathbf{x}, t) = \tilde{\Omega}(\mathbf{x}, t) + \Omega''(\mathbf{x}, t), \quad (3.29)$$

where $\Omega''(\mathbf{x}, t)$ is the unresolved small scale component. Hence, using this filtering technique the conservative variables are given by

$$\tilde{\mathbf{Q}} = (\bar{\rho}, \bar{\rho}\tilde{\mathbf{v}}, \bar{\rho}\tilde{e})^T. \quad (3.30)$$

Therefore, the Favre-filtered governing equations in Cartesian coordinates are determined by

$$\frac{\partial \tilde{\mathbf{Q}}}{\partial t} + \nabla \cdot \tilde{\mathbf{H}}_{inv} = \nabla \cdot \tilde{\mathbf{H}}_{vis} \quad (3.31)$$

and the filtered flux vectors then read

$$\tilde{\mathbf{H}}_{inv,i} = \begin{pmatrix} \bar{\rho}\tilde{u}_i \\ \bar{\rho}\tilde{u}_i\tilde{u}_1 + \bar{p}\delta_{i1} \\ \bar{\rho}\tilde{u}_i\tilde{u}_2 + \bar{p}\delta_{i2} \\ \bar{\rho}\tilde{u}_i\tilde{u}_3 + \bar{p}\delta_{i3} \\ \bar{\rho}\tilde{u}_i(\tilde{e} + \bar{p}/\bar{\rho}) \end{pmatrix}, \quad \text{and} \quad \tilde{\mathbf{H}}_{vis,i} = \frac{1}{Re_0} \begin{pmatrix} 0 \\ \tilde{\sigma}_{x_ix_1} + \tau_{x_ix_1} \\ \tilde{\sigma}_{x_ix_2} + \tau_{x_ix_2} \\ \tilde{\sigma}_{x_ix_3} + \tau_{x_ix_3} \\ \tilde{\beta}_i + \bar{\rho}(\tilde{e}u_i - \tilde{e}u_i) \end{pmatrix}. \quad (3.32)$$

The filtered stress tensor $\tilde{\sigma}_{ij}$ is given by

$$\tilde{\sigma}_{x_ix_j} = -2\mu \left(\tilde{S}_{ij} - \frac{1}{2}\delta_{ij} \frac{\partial \tilde{u}_i}{\partial x_j} \right) \quad \text{with} \quad \tilde{S}_{ij} = \frac{1}{2} \left(\frac{\partial \tilde{u}_i}{\partial x_j} + \frac{\partial \tilde{u}_j}{\partial x_i} \right), \quad (3.33)$$

where \tilde{S}_{ij} is a strain tensor with the Favre-filtered operation. The dissipative energy flux contribution $\tilde{\beta}_i$ in the energy equation is resolved by the large scale motions of the flow and is given by

$$\tilde{\beta}_i = \overline{u_j \sigma_{x_i x_j}} + \frac{k}{Pr(\gamma) - 1} \frac{\partial \tilde{T}}{\partial x_i}. \quad (3.34)$$

The unresolved subgrid-scale (SGS) stress tensor $\tau_{x_i x_j}$ is given by

$$\tau_{x_i x_j} = \bar{\rho}(\widetilde{u_i u_j} - \tilde{u}_i \tilde{u}_j). \quad (3.35)$$

The filtered pressure \bar{p} can be computed by

$$\bar{p} = (\gamma - 1) \left(\bar{\rho} \tilde{e} - \frac{1}{2} \bar{\rho} \tilde{u}^2 \right) \quad \text{with} \quad \tilde{e} = c_v \tilde{T}. \quad (3.36)$$

3.2.2 Time-averaged Navier-Stokes equations

A time-averaged form of the Navier-Stokes equations was developed to compute turbulent flow at high Reynolds numbers with the purpose of saving computational effort similarly to the LES method. The RANS equations describe the large time scales of fluid motion, and do not resolve the small scale motion of the turbulent flow. Similar to the spatial filtering, a decomposition of a flow variable $\Omega(\mathbf{x}, t)$ into a resolved component $\langle \Omega \rangle(\mathbf{x}, t)$, i.e., a time average of the flow variable and an unresolved component $\Omega'(\mathbf{x}, t)$, i.e., the unsteady fluctuation is performed [23], such that

$$\Omega(\mathbf{x}, t) = \langle \Omega \rangle(\mathbf{x}, t) + \Omega'(\mathbf{x}, t), \quad (3.37)$$

3. GOVERNING EQUATIONS AND MATHEMATICAL MODELS

where the resolved component (time-averaged component) is determined by

$$\langle \Omega \rangle(\mathbf{x}, t) = \frac{1}{\Delta T} \int_T^{T+\Delta T} \Omega(\mathbf{x}, t) dt. \quad (3.38)$$

The time interval ΔT is determined by separating the time scales that affect the unsteady large scale motions from the time scales of the turbulent fluctuations. That is, the time interval ΔT is related to the small scales motion of a turbulent flow and can be altered depending on the numerical method (see chap. 4.7). The Favre density averaging $\Omega = \langle \rho \Omega \rangle / \langle \rho \rangle$ (see eq. 3.28) is necessary to avoid an additional correlation similar to the spatial-filtered method, such that

$$\Omega(\mathbf{x}, t) = \{\Omega\}(\mathbf{x}, t) + \Omega''(\mathbf{x}, t), \quad (3.39)$$

where

$$\{\Omega\}(\mathbf{x}, t) = \frac{\langle \rho \Omega \rangle}{\langle \rho \rangle} = \frac{1}{\Delta T} \int_T^{T+\Delta T} \frac{\Omega(\mathbf{x}, t) \rho(\mathbf{x}, t)}{\langle \rho \rangle(\mathbf{x})} dt. \quad (3.40)$$

The time-averaged approach enables mean linear terms to be equal to non-mean terms since the mean fluctuations will be zero as a mathematical rule, i.e.:

$$\frac{\partial u}{\partial x} = \left\langle \frac{\partial (\langle u \rangle + u')}{\partial x} \right\rangle = \frac{\partial (\langle \langle u \rangle \rangle + \langle u' \rangle)}{\partial x} = \frac{\partial \langle u \rangle}{\partial x}. \quad (3.41)$$

The system of the RANS equations is not closed yet, since additional terms in the non-linear momentum and energy equation still exist, similar to the LES. The Reynolds stress-tensor τ_t in the momentum equations is given by

$$\tau_t = -\langle \rho \mathbf{u}' \mathbf{u}' \rangle, \quad (3.42)$$

and the turbulent kinetic energy and heat transfer terms in the energy equation are computed by

$$\langle \rho \rangle k = \frac{1}{2} \langle \rho \mathbf{u}'' \mathbf{u}'' \rangle \quad \text{and} \quad q_t = \langle \rho \mathbf{u}'' e'' \rangle, \quad (3.43)$$

respectively. The system of equations derived above still requires additional equations to close the system. The turbulent viscosity ν_t is considered to solve the equations. Similar to LES, the behavior of non-resolved turbulent motions have to be modeled. In other words, the RANS equations require more complex turbulence modeling with a framework of theoretical and empirical considerations. The turbulence modeling for RANS is briefly explained in the chapter 4.7. RANS yields lower computational cost compared to DNS and LES. Furthermore, many technical turbulent flow problems can be accurately solved only using the mean flow behavior with no consideration of the turbulent fluctuations. The problem is that, in the case of the turbulent production and dissipation in unsteady flow that is not in equilibrium, the RANS equations are not capable of investigating high-fidelity flow behavior. Instead, more accurate LES methods can be used to predict the flow field in such flow regions.

3. GOVERNING EQUATIONS AND MATHEMATICAL MODELS

4

Numerical Methods

The mathematical model derived in chapter three is in the form of a system partial differential equations, and requires either analytical solutions, which exist only for a few specific flow cases, or a numerical solution is necessary. First, a spatial discretization of finite volume type for the governing equations of unsteady compressible flow is described. Subsequently, the physical space is discretized by a body-fitted structured mesh. The inviscid fluxes are then discretized by means of an advection upstream splitting method (AUSM) and a monotone upstream centered scheme for conservation laws (MUSCL) scheme, whereas the viscous fluxes are discretized by a modified cell-vertex (MCV) scheme. The turbulence model of the LES and RANS equations are numerically formulated. A five stage Runge-Kutta scheme is used for the temporal discretization. Finally, additional treatments for the simulations, such as the ghost-cell approach and the boundary conditions, are explained.

4.1 Spatial discretization of finite volume

The system of partial differential equations is transformed into the system of semi-discrete ordinary differential equations by means of the method of lines (MOL) [24]. That is, the spatial derivatives are discretized, leaving the temporal derivatives in a continuous form. This yields an ordinary differential equation and the temporal derivative is then discretized appropriately. The overlines of the filtered LES equations and the averaging operator of the temporal averaging in the RANS equations are dropped to simplify the notation in this work. On the computational grid Ω_C , which consists of finite control volumes Ω_i ,

4. NUMERICAL METHODS

where the conservative variables \mathbf{Q} are averaged over each cell volume, i.e.:

$$\hat{\mathbf{Q}} = \frac{1}{V_i} \int_{\Omega_i} \mathbf{Q}(\mathbf{x}_i, t) d\Omega, \quad (4.1)$$

where the cell center coordinate \mathbf{x}_i is the average of the coordinates of the surrounding eight grid points. The cell volume is then given by

$$V_i = \int_{\Omega_i} d\Omega. \quad (4.2)$$

The surfaces of the control volume are defined by $S_{i,j}$ and the approximated fluxes $\hat{\mathbf{H}}_i$ are determined by

$$\hat{\mathbf{H}}_i = \frac{1}{A_{i,j}} \int_{S_i} H_i \cdot \mathbf{n} dS. \quad (4.3)$$

Using the integral form of the NSE eq. 3.2, and eq. 4.1 and eq. 4.3, the system of ordinary differential equations is given by

$$\frac{d\hat{\mathbf{Q}}_i}{dt} = -\frac{1}{V_i} \sum_{j=1}^{n_s} \left(\hat{\mathbf{H}}_{i,j} \cdot \mathbf{n}_j \right) = RHS(\hat{\mathbf{Q}}). \quad (4.4)$$

The fluxes on the right-hand side (RHS) of the equation are computed at every time step.

4.2 Transformation to Curvilinear coordinates

The physical domain is transformed into a structured curvilinear grid using body-fitted meshes. The body-fitted mesh offers many advantages in comparison to Cartesian coordinates. For instance, the mesh is easily and accurately fitted to the wall geometry since grid lines are not required to align with the axes of the Cartesian grid. Therefore, boundary conditions can be easily applied compared to a Cartesian cut-cell method [25].

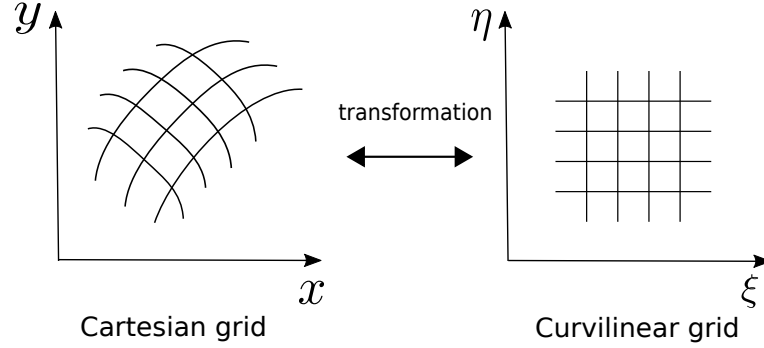


Figure 4.1: Transformation between Cartesian and curvilinear coordinates in two-dimensions. The grid is transformed from physical space (left) to computational space (right). The grid in computational coordinates (ξ, η) has uniform spacing.

The cells in a curvilinear grid can stretch independently in the space directions. That is, the number of cells can be kept low due to a significant reduction in the cell numbers within unimportant directions, e.g., the flow over an airfoil does not require the same grid resolution in the spanwise direction as in the streamwise direction.

The governing equations eq. 3.4 were derived for a Cartesian coordinate system, therefore a transformation into curvilinear coordinates is necessary. The coordinates of the computational mesh are given by

$$\xi = \xi(x, y, z), \quad \eta = \eta(x, y, z), \quad \zeta = \zeta(x, y, z), \quad (4.5)$$

where the grid distribution in the computational domain is required to have uniform spacing and unit length, i.e., $\Delta\xi$, $\Delta\eta$ and $\Delta\zeta = 1$. Using the chain rule from differential calculus, the partial derivatives in x-direction can be expressed by

$$\frac{\partial}{\partial x} = \frac{\partial}{\partial \xi} \frac{\partial \xi}{\partial x} + \frac{\partial}{\partial \eta} \frac{\partial \eta}{\partial x} + \frac{\partial}{\partial \zeta} \frac{\partial \zeta}{\partial x}. \quad (4.6)$$

4. NUMERICAL METHODS

In matrix notation for all components this becomes

$$\begin{pmatrix} \frac{\partial}{\partial x} \\ \frac{\partial}{\partial y} \\ \frac{\partial}{\partial z} \end{pmatrix} = \begin{pmatrix} \xi_x & \eta_x & \zeta_x \\ \xi_y & \eta_y & \zeta_y \\ \xi_z & \eta_z & \zeta_z \end{pmatrix} \begin{pmatrix} \frac{\partial}{\partial \xi} \\ \frac{\partial}{\partial \eta} \\ \frac{\partial}{\partial \zeta} \end{pmatrix} \quad (4.7)$$

and the inverse transformation can be obtained by

$$\begin{pmatrix} \frac{\partial}{\partial \xi} \\ \frac{\partial}{\partial \eta} \\ \frac{\partial}{\partial \zeta} \end{pmatrix} = \begin{pmatrix} x_\xi & y_\xi & z_\xi \\ x_\eta & y_\eta & z_\eta \\ x_\zeta & y_\zeta & z_\zeta \end{pmatrix} \begin{pmatrix} \frac{\partial}{\partial x} \\ \frac{\partial}{\partial y} \\ \frac{\partial}{\partial z} \end{pmatrix}, \quad (4.8)$$

where the subscripts denote the respective derivative and the metric coefficients are given by

$$\begin{aligned} \xi_x &= J^{-1}(y_\eta z_\zeta - y_\zeta z_\eta), & \eta_x &= J^{-1}(y_\zeta z_\xi - y_\xi z_\zeta), & \zeta_x &= J^{-1}(y_\xi z_\eta - y_\eta z_\xi), \\ \xi_y &= J^{-1}(z_\eta x_\zeta - z_\zeta x_\eta), & \eta_y &= J^{-1}(z_\zeta x_\xi - z_\xi x_\zeta), & \zeta_y &= J^{-1}(z_\xi x_\eta - z_\eta x_\xi), \\ \xi_z &= J^{-1}(x_\eta y_\zeta - x_\zeta y_\eta), & \eta_z &= J^{-1}(x_\zeta y_\xi - x_\xi y_\zeta), & \zeta_z &= J^{-1}(x_\xi y_\eta - x_\eta y_\xi). \end{aligned}$$

The Jacobian J is the determinant of the metric coefficients matrix, such that

$$\begin{aligned} J &= x_\xi y_\eta z_\zeta + y_\xi z_\eta x_\zeta + z_\xi x_\eta y_\zeta - x_\xi y_\zeta z_\eta - y_\xi z_\zeta x_\eta - z_\xi x_\zeta y_\eta \\ &= (\xi_x \eta_y \zeta_z + \xi_y \eta_z \zeta_x + \xi_z \eta_x \zeta_y - \xi_x \eta_z \zeta_y - \xi_y \eta_x \zeta_z - \xi_z \eta_y \zeta_x)^{-1}. \end{aligned} \quad (4.9)$$

4.2 Transformation to Curvilinear coordinates

As a result, the transformed governing equations can be written as (cf. eq. 3.4)

$$\begin{aligned}
& \frac{\partial \mathbf{Q}}{\partial t} + \xi_t \frac{\partial \mathbf{Q}}{\partial \xi} + \eta_t \frac{\partial \mathbf{Q}}{\partial \eta} + \zeta_t \frac{\partial \mathbf{Q}}{\partial \zeta} \\
& + \xi_x \frac{\partial \mathbf{E}}{\partial \xi} + \eta_x \frac{\partial \mathbf{E}}{\partial \eta} + \zeta_x \frac{\partial \mathbf{E}}{\partial \zeta} \\
& + \xi_y \frac{\partial \mathbf{F}}{\partial \xi} + \eta_y \frac{\partial \mathbf{F}}{\partial \eta} + \zeta_y \frac{\partial \mathbf{F}}{\partial \zeta} \\
& + \xi_z \frac{\partial \mathbf{G}}{\partial \xi} + \eta_z \frac{\partial \mathbf{G}}{\partial \eta} + \zeta_z \frac{\partial \mathbf{G}}{\partial \zeta} = 0.
\end{aligned} \tag{4.10}$$

The geometric properties of every grid point are determined by the metric coefficients and the Jacobian can be interpreted as the control volume of the grid cell. In case of a non-moving grid, the metric coefficients are required to be calculated only once at the solver start-up. The covariant velocities \mathbf{v} in the Cartesian directions are transformed to the contravariant velocities $\mathbf{U} = (u, v, w)$ on the curvilinear grid, such that

$$\begin{aligned}
U &= \xi_x u + \xi_y v + \xi_z w, \\
V &= \eta_x u + \eta_y v + \eta_z w, \\
W &= \zeta_x u + \zeta_y v + \zeta_z w.
\end{aligned} \tag{4.11}$$

However, since equation 4.11 is a weak conservative form mathematical discontinuities cannot be treated accurately. Thus, a strong conservation- law is applied, using the Jacobian J . This approach is introduced by Viviand [26] and Vinokur [27], such that

$$\frac{\partial \hat{\mathbf{Q}}}{\partial t} + \frac{\partial \hat{\mathbf{E}}}{\partial \xi} + \frac{\partial \hat{\mathbf{F}}}{\partial \eta} + \frac{\partial \hat{\mathbf{G}}}{\partial \zeta} = 0, \tag{4.12}$$

where

$$\hat{\mathbf{Q}} = J\mathbf{Q} \quad \text{and, e. g.:} \quad \hat{\mathbf{E}} = J(\xi_x \mathbf{E} + \xi_y \mathbf{F} + \xi_z \mathbf{G}). \tag{4.13}$$

4. NUMERICAL METHODS

Using the split fluxes the strong convection-law form of the governing equations can be expressed by

$$\frac{\partial \hat{\mathbf{Q}}}{\partial t} + \frac{\partial \hat{\mathbf{E}}_{inv}}{\partial \xi} + \frac{\partial \hat{\mathbf{F}}_{inv}}{\partial \eta} + \frac{\partial \hat{\mathbf{G}}_{inv}}{\partial \zeta} = \frac{\partial \hat{\mathbf{E}}_{vis}}{\partial \xi} + \frac{\partial \hat{\mathbf{F}}_{vis}}{\partial \eta} + \frac{\partial \hat{\mathbf{G}}_{vis}}{\partial \zeta}, \quad (4.14)$$

where the transformed fluxes are given by

$$\hat{\mathbf{E}}_{inv} = \begin{pmatrix} \rho u \\ \rho U u + \xi_x p \\ \rho U v + \xi_y p \\ \rho U w + \xi_z p \\ U(\rho e + p) \end{pmatrix}, \quad \hat{\mathbf{E}}_{vis} = \frac{1}{Re_0} \begin{pmatrix} 0 \\ \xi_x \tau_{xx} + \xi_y \tau_{yx} + \xi_z \tau_{zx} \\ \xi_x \tau_{xy} + \xi_y \tau_{yy} + \xi_z \tau_{zy} \\ \xi_x \tau_{xz} + \xi_y \tau_{yz} + \xi_z \tau_{zz} \\ \xi_x \beta_x + \xi_y \beta_y + \xi_z \beta_z \end{pmatrix}, \quad (4.15)$$

$$\hat{\mathbf{F}}_{inv} = \begin{pmatrix} \rho v \\ \rho V u + \eta_x p \\ \rho V v + \eta_y p \\ \rho V w + \eta_z p \\ V(\rho e + p) \end{pmatrix}, \quad \hat{\mathbf{F}}_{vis} = \frac{1}{Re_0} \begin{pmatrix} 0 \\ \eta_x \tau_{xx} + \eta_y \tau_{yx} + \eta_z \tau_{zx} \\ \eta_x \tau_{xy} + \eta_y \tau_{yy} + \eta_z \tau_{zy} \\ \eta_x \tau_{xz} + \eta_y \tau_{yz} + \eta_z \tau_{zz} \\ \eta_x \beta_x + \eta_y \beta_y + \eta_z \beta_z \end{pmatrix}, \quad (4.16)$$

$$\hat{\mathbf{G}}_{inv} = \begin{pmatrix} \rho w \\ \rho W u + \zeta_x p \\ \rho W v + \zeta_y p \\ \rho W w + \zeta_z p \\ W(\rho e + p) \end{pmatrix}, \quad \hat{\mathbf{G}}_{vis} = \frac{1}{Re_0} \begin{pmatrix} 0 \\ \zeta_x \tau_{xx} + \zeta_y \tau_{yx} + \zeta_z \tau_{zx} \\ \zeta_x \tau_{xy} + \zeta_y \tau_{yy} + \zeta_z \tau_{zy} \\ \zeta_x \tau_{xz} + \zeta_y \tau_{yz} + \zeta_z \tau_{zz} \\ \zeta_x \beta_x + \zeta_y \beta_y + \zeta_z \beta_z \end{pmatrix}. \quad (4.17)$$

4.3 Discretization of the inviscid fluxes

4.3.1 AUSM

The inviscid flux is discretized by a second-order advection upstream splitting method (AUSM) by Liou and Steffen [28], which provides a high numerical stability. The ASUM also offers the simplicity of the flux-vector splitting methods [29] and the accuracy of the flux-difference splitting methods [30]. A node-centered control volume is applied and the eight vertices of the control volume are identified, i.e., the eight points at $i \pm \frac{1}{2}, j \pm \frac{1}{2}, k \pm \frac{1}{2}$ [2].

4.3 Discretization of the inviscid fluxes

Furthermore, the fluxes are considered at the face center of the control volume in the ξ -direction at $i \pm \frac{1}{2}, j, k$, such that

$$\left. \frac{\partial \hat{\mathbf{H}}_{inv}}{\partial \xi} \right|_{i,j,k} = \hat{\mathbf{H}}_{inv,i+\frac{1}{2},j,k} - \hat{\mathbf{H}}_{inv,i-\frac{1}{2},j,k}. \quad (4.18)$$

Subsequently, the inviscid flux $\hat{\mathbf{H}}_{inv}$ is split into a convective term $\hat{\mathbf{H}}_{inv}^C$ and a pressure term $\hat{\mathbf{H}}_{inv}^P$ due to the different propagation speed of pressure and convective properties in the physical domain, i.e., the discretized inviscid flux in the x-direction is given by

$$\hat{\mathbf{E}}_{inv}^C = J \begin{pmatrix} \rho U \\ \rho U u \\ \rho U v \\ \rho U w \\ U(\rho e + p) \end{pmatrix}, \quad \hat{\mathbf{E}}_{inv}^P = J \begin{pmatrix} 0 \\ \xi_x p \\ \xi_y p \\ \xi_z p \\ 0 \end{pmatrix} \quad (4.19)$$

and accordingly for the other two physical directions (y,z). The convective flux at the cell surface is computed using the local speed of sound, such that

$$\hat{\mathbf{E}}_{inv}^C|_{i \pm \frac{1}{2},j,k} = Ma_{\frac{1}{2}} J |\nabla \xi| \begin{pmatrix} \rho a \\ \rho a u \\ \rho a v \\ \rho a w \\ a(\rho e + p) \end{pmatrix}_{L/R}, \quad (4.20)$$

where the subscript $(.)_{\frac{1}{2}}$ denotes the cell surface and the subscript $(.)_{L/R}$ implies the left and right states on the cell surface. The Mach number at the interface of the cell is

4. NUMERICAL METHODS

computed by an average of the left and right state, i. e.:

$$Ma_{\frac{1}{2}} = \frac{1}{2}(Ma_L + Ma_R) \quad (4.21)$$

The split Mach number can be computed using van Leer splitting [28], such that

$$Ma_{L/R} = \begin{cases} \pm \frac{1}{4}(|Ma| \pm 1)^2, & |Ma| \geq 1 \\ \frac{1}{4}(Ma \pm |Ma|), & |Ma| < 1 \end{cases} \quad (4.22)$$

The pressure at the interface is then computed by

$$p_{\frac{1}{2}} = p_L^+ + p_R^-, \quad (4.23)$$

where the pressure on the left and right side is given by

$$p_L^\pm = p_{L/R} \left(\frac{1}{2} \pm \chi Ma_{L/R} \right) \quad (4.24)$$

where the parameter χ represents the ratio between the change rate of the pressure and the change of the local Mach number, and set to $\chi = 1/64$ in this work.

4.3.2 MUSCL scheme

The left and right states of the flow variables in the AUSM is approximated by the monotone upstream centered scheme for conservation laws (MUSCL) by Van Leer [31]. The conservative variables $\mathbf{Q} = (\rho, \rho \mathbf{v}, \rho e)^T$ are interpolated at the interface between the cells and the interpolated variables are used for the reconstruction of the flux. In contrast

to Godunov's method, which assumes constant variables, the MUSCL assumes a linear distribution. This increases the first order of Godunov's method to second-order. The left and right states on the surfaces of the cells are given by

$$\begin{aligned}\hat{\mathbf{Q}}_{i+\frac{1}{2},j,k}^L &= \hat{\mathbf{Q}}_{i,j,k} + \psi_i \frac{l_{i+\frac{1}{2},j,k}}{\left(l_{i+\frac{1}{2},j,k} + l_{i-\frac{1}{2},j,k}\right)^2} \left(l_{i-\frac{1}{2},j,k} \Delta_{i+\frac{1}{2},j,k}(\hat{\mathbf{Q}}) + l_{i+\frac{1}{2},j,k} \Delta_{i-\frac{1}{2},j,k}(\hat{\mathbf{Q}})\right) \\ \hat{\mathbf{Q}}_{i+\frac{1}{2},j,k}^R &= \hat{\mathbf{Q}}_{i+1,j,k} + \psi_{i+1} \frac{l_{i+\frac{1}{2},j,k}}{\left(l_{i+\frac{1}{2},j,k} + l_{i-\frac{3}{2},j,k}\right)^2} \left(l_{i+\frac{1}{2},j,k} \Delta_{i+\frac{3}{2},j,k}(\hat{\mathbf{Q}}) + l_{i+\frac{3}{2},j,k} \Delta_{i+\frac{1}{2},j,k}(\hat{\mathbf{Q}})\right)\end{aligned}\tag{4.25}$$

where the Δ operator denotes the difference between the values of the variables at the left and right cell-center, such that

$$\Delta_{i\pm\frac{1}{2},j,k}(\hat{\mathbf{Q}}) = \pm \hat{\mathbf{Q}}_{i+\frac{1}{2},j,k} \mp \hat{\mathbf{Q}}_{i,j,k}\tag{4.26}$$

and the distance between the left and right cell center is given by

$$l_{i\pm\frac{1}{2},j,k} = \sqrt{\left(\Delta_{i+\frac{1}{2},j,k}(x)\right)^2 + \left(\Delta_{i+\frac{1}{2},j,k}(y)\right)^2 + \left(\Delta_{i+\frac{1}{2},j,k}(z)\right)^2}.\tag{4.27}$$

The variable ψ denotes a given limiter function used for the treatment of discontinuities, hence, it is set to $\psi = 1$ due to no discontinuities expected in this work.

4.4 Discretization of the viscous fluxes

The viscous flux containing stress and energy equations, governing the viscous forces of the fluid in the NSE, is discretized by a second order modified cell-vertex scheme (MCV) [32]. The flux at a cell face $(i + \frac{1}{2}, j, k)$ is averaged from the four vertices $(i + \frac{1}{2}, j \pm \frac{1}{2}, k \pm \frac{1}{2})$

4. NUMERICAL METHODS

of the face and the derivative of the viscous flux $\widehat{\mathbf{E}}_{vis}$ in the ξ -direction is given by

$$\begin{aligned} \left. \frac{\partial \widehat{\mathbf{E}}_{vis}}{\partial \xi} \right|_{i,j,k} &= \frac{1}{4} \left(\widehat{\mathbf{E}}_{vis,i+\frac{1}{2},j+\frac{1}{2},k+\frac{1}{2}} + \widehat{\mathbf{E}}_{vis,i+\frac{1}{2},j-\frac{1}{2},k+\frac{1}{2}} \right) \\ &\quad + \frac{1}{4} \left(\widehat{\mathbf{E}}_{vis,i+\frac{1}{2},j+\frac{1}{2},k-\frac{1}{2}} + \widehat{\mathbf{E}}_{vis,i+\frac{1}{2},j-\frac{1}{2},k-\frac{1}{2}} \right) \\ &\quad - \frac{1}{4} \left(\widehat{\mathbf{E}}_{vis,i-\frac{1}{2},j+\frac{1}{2},k+\frac{1}{2}} + \widehat{\mathbf{E}}_{vis,i-\frac{1}{2},j-\frac{1}{2},k+\frac{1}{2}} \right) \\ &\quad - \frac{1}{4} \left(\widehat{\mathbf{E}}_{vis,i-\frac{1}{2},j+\frac{1}{2},k-\frac{1}{2}} + \widehat{\mathbf{E}}_{vis,i-\frac{1}{2},j-\frac{1}{2},k-\frac{1}{2}} \right) \end{aligned} \quad (4.28)$$

4.5 Temporal discretization

In eq. 4.4 only the temporal derivatives are still in continuous form, whereas the spatial derivatives were discretized using appropriate methods. The temporal derivatives are discretized by an explicit multi-stage Runge-Kutta method [33], which is a multiple corrector explicit time scheme to advance the solution from t^n to t^{n+1} . In this work a five-stage Runge-Kutta scheme [34] is applied. Grouping the spatial discretization as RHS $\widehat{\mathbf{Q}}$, the governing equations (eq. 3.3) can be expressed by

$$\frac{\partial \widehat{\mathbf{Q}}}{\partial t} = RHS(\widehat{\mathbf{Q}}). \quad (4.29)$$

The propagation of $\widehat{\mathbf{Q}}$ from n to $n+1$ is given by

$$\begin{aligned} \widehat{\mathbf{Q}}^0 &= \widehat{\mathbf{Q}}^n \\ &\vdots \\ \widehat{\mathbf{Q}}^l &= \widehat{\mathbf{Q}}^n - \alpha_l \Delta t RHS(\widehat{\mathbf{Q}}^{l-1}), \quad l = 1, \dots, 5 \\ &\vdots \\ \widehat{\mathbf{Q}}^{n+1} &= \widehat{\mathbf{Q}}^5 \end{aligned} \quad (4.30)$$

4.6 Turbulence model for large-eddy simulations

where l and n denotes the step index and the time index, respectively, and α_l are the coefficients, which control the order and stability of the scheme. The coefficients α_l is given by

$$\alpha_1 = \frac{6}{24} \quad \alpha_2 = \frac{4}{24} \quad \alpha_3 = \frac{9}{24} \quad \alpha_4 = \frac{12}{24} \quad \alpha_5 = \frac{24}{24}, \quad (4.31)$$

for maximum stability. The magnitude of the time step $\Delta t = t^{n+1} - t^n$ must be restricted in order to maintain the numerical stability. It is iteratively computed over all cells and set to a minimum value based on the CFL condition [35], which applies a maximum CFL-number 2.5, such that

$$\Delta t_i = \frac{CFL_{max}}{\left(\frac{|U|+a|\nabla\xi|}{\Delta\xi} \right) + \left(\frac{|V|+a|\nabla\eta|}{\Delta\eta} \right) + \left(\frac{|W|+a|\nabla\zeta|}{\Delta\zeta} \right)} \quad (4.32)$$

in curvilinear coordinates for each cell i with the speed of sound a . The velocity components U, V, W are in computational direction ξ, η, ζ , respectively. The intermediate-step solution $\hat{\mathbf{Q}}^l$ in eq. 4.30 is obtained by the $RHS(\hat{\mathbf{Q}}^{l-1})$ at the foregoing step $l - 1$.

4.6 Turbulence model for large-eddy simulations

In sec. 3.2.1 the spatial filtering operation yielded a the large-eddy simulation (LES) formulation of the governing equations, but required unknown variables such as the subgrid-scale(SGS) stress term τ_{x_i, x_j} and the SGS energy term $\bar{\rho}(\widetilde{eu_i} - \tilde{e}\tilde{u}_i)$ in eq. 3.32 to close the system of equations. The main purpose of turbulence modeling for LES is to remove energy from the large scale turbulent structures, mimicking the drain of energy from large scales to small scales, related to the turbulent energy cascade [2]. A classical turbulence model using explicit modeling of the unresolved scales is that by Smagorinsky [36]. It applies an eddy-viscosity approach to balance the dissipation rate at the unresolved scales instead of directly transferring the energy from larger to smaller scales. The eddy-viscosity ν_t is responsible for the turbulent scale effects and can be treated with the mixed model (MM) of Bardina *et al.* [37] such that a non-eddy viscosity approach is applied.

In this work, a monotonically intergrated LES (MILES) [38] method using implicit modeling is introduced. The SGS stress term τ_{x_i, x_j} and the SGS energy term $\bar{\rho}(\widetilde{eu_i} - \tilde{e}\tilde{u}_i)$ are assumed to be zero, preserving the monotonicity of the integral form of the Navier-Stokes equations to transfer the energy correctly [2]. Compared to the explicit modeling

4. NUMERICAL METHODS

by Smagorinsky, it was proven that MILES can be applied to the simulation of complex flow problems [39] [40].

4.7 Turbulence model for Reynolds-averaged Navier-Stokes equations

In sec. 3.2.2 the system of the RANS equations was derived, however, leaving more unknowns than equations due to the appearance of additional terms, i.e., Reynolds stress-tensor τ_t and the turbulent heat transfer term q_t . In order to close the system of the equations, the turbulent viscosity is introduced by Boussinesq [41]. The turbulent Reynolds stress term can then be computed by

$$\tau_t = -\langle \rho \mathbf{u}'' \mathbf{u}'' \rangle = \mu_t \left(\frac{\partial u_i}{\partial x_j} + \frac{\partial u_j}{\partial x_i} \right) - \frac{2}{3} \mu_t \delta_{i,j} \frac{\partial u_i}{\partial x_j}, \quad (4.33)$$

where μ_t is the turbulent viscosity. Note that the viscous shear stress of a Newtonian fluid is similarly computed as the stress term in RANS equations. The turbulent heat transfer term can be computed by

$$q_t = \langle \rho \mathbf{u}'' e'' \rangle = -\frac{\mu_t c_p}{Pr_t} \nabla T \quad (4.34)$$

where Pr_t is the turbulent Prandtl number, set to 0.9. Finally, the unknown variables are reduced to only the eddy viscosity $\nu_t = \mu_t / \rho$. The Boussinesq approach assumes turbulent equilibrium [8] [42], balancing between the turbulent production and dissipation. In spite of the restrictions and disadvantages for the non-equilibrium state, this is still valid for many aerodynamic applications, yielding reliable results. The approach to estimate the eddy viscosity is introduced in the following subsection.

4.7.1 Spalart-Allmaras one-Equation turbulence model

In order to estimate the eddy viscosity ν_t , which is only the unknown variable in the RANS equation, the one-equation by spalart-allmaras (SA) [43] is used in this work. This approach is composed of four different stages requiring additional terms, which increases the numerical complexity. The highest stage is applied, and as a result, an artificial

4.7 Turbulence model for Reynolds-averaged Navier-Stokes equations

turbulent viscosity $\tilde{\nu}$ in a transport equation is computed by

$$\frac{\partial \tilde{\nu}}{\partial t} + U_i \frac{\partial \tilde{\nu}}{\partial x_i} = \underbrace{c_{b1} \tilde{S} \tilde{\nu}}_{\text{production}} - \underbrace{c_{w1} f_w \left(\frac{\tilde{\nu}}{d} \right)^2}_{\text{destruction}} + \underbrace{\frac{1}{\sigma} \left[\nabla \cdot ((\nu_t + \tilde{\nu}) \nabla \tilde{\nu}) + c_{b2} (\nabla \tilde{\nu})^2 \right]}_{\text{diffusion}} \quad (4.35)$$

with

$$\nu_t = \tilde{\nu} f_{v1}. \quad (4.36)$$

The closure functions and coefficients for equation (4.35) and (4.36) are determined by

$$f_{v1} = \frac{\chi^3}{\chi^3 + c_{v1}^3}, \quad f_{v2} = 1 - \frac{\chi}{1 + \chi f_{v1}}, \quad \chi = \frac{\tilde{\nu}}{\nu}, \quad (4.37)$$

$$f_w = g \left[\frac{1 + c_{w3}^6}{g^6 + c_{w3}^6} \right]^{\frac{1}{6}}, \quad g = r + c_{w2}(r^6 - r), \quad r = \frac{\tilde{\nu}}{\tilde{P} \kappa^2 d^2}, \quad (4.38)$$

where the parameters are set to

$$c_{b1} = 0.1355, \quad c_{b2} = 0.622, \quad c_{v1} = 7.1, \quad \sigma = \frac{2}{3}, \quad (4.39)$$

$$c_{w1} = \frac{c_{b1}}{\kappa_2} + \frac{1 + c_{b2}}{\sigma}, \quad c_{w2} = 0.3, \quad c_{w3} = 2, \quad \kappa = 0.41. \quad (4.40)$$

The production term \tilde{P} is a normalized function of the rotation tensor $|\Omega| = \frac{1}{2} |(\nabla \mathbf{u} - (\nabla \mathbf{u})^T)|$ or the magnitude of the vorticity $|\nabla \times \mathbf{u}|$, such that

$$\tilde{P} = P + \frac{\tilde{\nu}}{\kappa^2 d^2} f_{v2} \quad \text{with} \quad P = |\Omega| = |\nabla \times \mathbf{u}|. \quad (4.41)$$

4. NUMERICAL METHODS

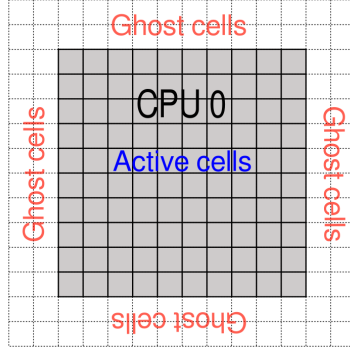


Figure 4.2: Active cells and ghost cells in a CPU

4.8 Additional treatments for the simulation

In order to implement the numerical schemes, additional computational procedures are necessary. First, a ghost-cell approach is introduced. Then, the boundary conditions are described.

4.8.1 Ghost-cell approach

The ghost-cell approach is applied to compute the flux of cells which are located near the boundaries of the computational domain, depicted in Fig. 4.2. Two supplementary layers of cells (called ghost cells) are added to all sides of the domain. The temporal and spatial integration is not carried out on these ghost-cells. That is, only the active cells are used by the temporal and spatial integration, leaving two ghost-cell stencils to be extrapolated in all directions. The values of the ghost cells can be retrieved from overlapping active cells in neighboring domains or from appropriate boundary conditions.

In order to compute the governing equations at high Reynolds numbers, i.e., a large number of cells is used, it is necessary to split the computational domains into numerous smaller domains to speed up the computation by means of multiple CPUs. This requires a communication between CPUs, since each split domain has only partial data and needs the information of neighboring domains. As a result, the ghost layers of the neighboring domain are overlapped over the active cells, and then the variables of ghost cells are transferred into the the active cells. This exchange approach is performed once for each Runge-Kutta step. For the zonal method a special exchange method is necessary, explained in detail, in sec. 5.2.3. A zonal exchange procedure is also performed as explained in sec. 5.2.3.

4.8.2 Boundary conditions

Due to the finite size of the physical domain boundary conditions need to be applied to accurately define the physical problem under consideration in the computational space. The boundary conditions are applied using the ghost-cell approach at the boundary surface.

The no-slip condition is a physically important boundary condition for the flow over a wall. The velocity in the direction tangential to the wall must be zero due to the effect of friction. The gradient of the pressure and the density have to be zero on the wall. That is, the mathematical boundary conditions are given by

$$u|_{wall} = 0 \quad , \quad \frac{\partial p}{\partial n}|_{wall} = 0 \quad \text{and} \quad \frac{\partial \rho}{\partial n}|_{wall} = 0. \quad (4.42)$$

To satisfy such mathematical conditions, the velocities of ghost-cells beyond the wall are set to negative values which are equal to the same absolute values of active cells. Thus, the velocities on the wall are set to zero at the boundary surface. Having the same gradient of the ghost-cells beyond the wall as the gradient of the active cells, the temperature and pressure gradient on the wall become zero. The SA transport variable $\tilde{\nu}_t$ on the wall is set to zero, as introduced by P. R. Spalart [44], leading to non-turbulent viscosity. The no-slip boundary condition is computed by

$$\begin{pmatrix} \rho \\ \rho \mathbf{v} \\ \rho e \\ -\rho \tilde{\nu} \end{pmatrix}_g = \begin{pmatrix} \rho \\ -\rho \mathbf{v} \\ \rho e \\ \rho \tilde{\nu} \end{pmatrix}_a \quad (4.43)$$

where the $(.)_a$ and $(.)_g$ denote the index of active cell and ghost cell, respectively.

At the inflow of the domain a set of different boundary conditions is used.

- Rescaling

4. NUMERICAL METHODS

- Given profile BC

The profile is obtained from a previous RANS computation. Solutions for a pure RANS and a pure LES solution (see chap. 6) are obtained using a rescaling method, where a slice of the flow downstream of the inflow is rescaled appropriately and prescribed at the inflow. For more details on the rescaling method, see subsec. 5.1.1. By means of the rescaling method, the desired boundary layer thickness at the inflow of the domain can be approximately obtained. The flow quantities at the inflow can be computed by

$$\begin{pmatrix} \rho \\ \rho \mathbf{v} \\ \rho \tilde{v} \end{pmatrix}_g = \begin{pmatrix} \rho \\ \rho \mathbf{v} \\ \rho \tilde{v} \end{pmatrix}_{RANS(\theta)}. \quad (4.44)$$

A zero-pressure and zero-density gradient is prescribed at the inflow of the domain. Therefore, the energy term at the inflow is computed by

$$(\rho e)_g = \frac{p_a}{\gamma - 1} + \frac{1}{2}(\rho_g \mathbf{v}_g^2). \quad (4.45)$$

At the outflow boundaries of the domain characteristic outflow conditions are applied, such that

$$\begin{pmatrix} \rho \\ \rho \mathbf{v} \\ \rho e \end{pmatrix}_S = \begin{pmatrix} \rho_a + \frac{p_\infty - p_a}{a_a^2} \\ \mathbf{v}_a + \xi_{x,S} \left(\frac{p_a - p_\infty}{\rho_a a_a} \right) \\ \frac{p_S}{\gamma} + \frac{\rho}{2} \mathbf{v}_S^2 \end{pmatrix} \quad (4.46)$$

where $a_a = \sqrt{\gamma \rho / p_a}$ is the local speed of sound in the active cells and $(.)_S$ is the index of variables at the boundary surface. The flow quantities of the active cells are extrapolated

onto the ghost-cells at the boundary surface, such that

$$\begin{pmatrix} \rho \\ \rho \mathbf{v} \\ \rho e \end{pmatrix}_g = \begin{pmatrix} \rho_a + (\rho_S - \rho_a) \frac{d_g}{d_S} \\ (\rho \mathbf{v})_a + (\rho_{b.s.} \mathbf{v}_S - (\rho \mathbf{v})_a) \frac{d_g}{d_S} \\ (\rho e)_a + ((\rho e)_S - (\rho e)_a) \frac{d_g}{d_S} \end{pmatrix} \quad (4.47)$$

where d_S is the distance between the center of the active cell and the boundary surface and d_g is the distance between the center of the active cell and the center of the ghost cell. However, pressure oscillations occur at the inflow and outflow since the boundary conditions are partially reflecting. Hence, a special dumping treatment, i.e. the sponge layer [1] is used. It can be regarded as a source term $\hat{\mathbf{S}}$ added to the right-hand side of eq. 4.4, to remove the pressure oscillations. The source term $\hat{\mathbf{S}}$ is computed by

$$\hat{\mathbf{S}} = \sigma_{sp} \left(\begin{pmatrix} \rho(\xi, t) \\ 0 \\ 0 \\ 0 \\ \rho e(\xi, t) \end{pmatrix} - \begin{pmatrix} \rho(\xi, t) \\ 0 \\ 0 \\ 0 \\ \rho e(\xi, t) \end{pmatrix}_{ref} \right) \quad (4.48)$$

where σ_{sp} denotes the damping factor. The factor is large at the boundary surface, but reduced in normal direction away from the surface.

To deal with three dimensionality numerically, a periodic boundary condition is applied to the computational domain. The z-direction can be extended to an infinite space due to the statistically 2D boundary layer. The flow quantities of the active cells at the periodic boundary are exchanged with the cells at the opposing side and vice versa.

4. NUMERICAL METHODS

5

Zonal RANS-LES Method

As explained in the previous chapter, DNS and also high-resolution LES of a turbulent flow at high Reynolds numbers consumes high computational power and time due to the necessary fine grid resolution. Numerical stability has to be maintained when applying an explicit time integration scheme, and thus, the numerical time step is limited to small values. However, a turbulent flow problem in non-equilibrium state occurs only in a specific area. Applying LES throughout the domain is therefore not an efficient way to solve the turbulent flow. Therefore, it would be elegant to perform a RANS simulation for non-interesting areas in the flow field, while using the LES simultaneously in the important regions where a higher grid resolution is required. This allows a much cheaper simulation of turbulent flow at high Reynolds numbers and saves computational memory, resulting in a reliable solution, yet efficient without large differences to DNS.

The present work pursues the concept of a fully coupled zonal RANS-LES approach [45] using multiple RANS and LES zones. The term *fully coupled* indicates the zonal RANS-LES simulation type in which the flow data is transferred from the RANS zone to the LES zone and vice versa at every time step [2]. The zonal RANS-LES method takes advantage of the strength of both a pure RANS or a pure LES. In the RANS zone, a coarse mesh and time-averaged variables are applied, while a fine mesh and a proper subgrid model are used in the LES zone. Hence, each flow field of RANS and LES are appropriately dealt with for suitable turbulence modeling. The main issue with the zonal method is transferring variables between the zonal interfaces, considering the applied method in the upstream and downstream direction; e.g., synthetic turbulence generation method. To exchange such reliable flow quantities, the zones must sufficiently overlap and the exchange of variables is performed using a suitable interpolation procedure.

First, zonal boundary conditions are derived. The proper treatments at the zonal interfaces are the most challenging part of the zonal RANS-LES method in this work. Subsequently, numerical implementation of the exchange procedure is explained in detail, embedded into the Zonal Flow Solver (ZFS).

5. ZONAL RANS-LES METHOD

5.1 Zonal boundary conditions

There are two different zonal interfaces in a zonal RANS-LES method. The zonal interfaces have to be treated with computationally distinct approaches, since RANS and LES apply different numerical methods, leading to a different number of variables. The first zonal interface is a RANS-to-LES transition boundary condition at the inflow of the LES domain. Secondly, the zonal interface occurs at the outflow of RANS domain, transferring only the mean pressure into an upstream RANS. The zonal boundary conditions are always positioned at the beginning or the end of the computational domain of each RANS or LES zone (see Fig. 5.1).

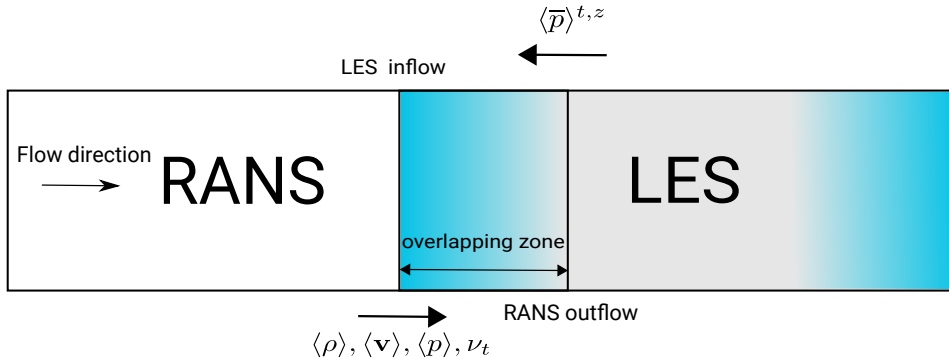


Figure 5.1: Sketch of the zonal RANS-LES method.

5.1.1 First zonal interface

The first zonal interface is a RANS-to-LES transition boundary condition at the inflow of the LES domain. In this case variables from the RANS domain are transferred onto the LES domain. However, the flow field in the RANS zone is lacking any turbulent fluctuations, since a much coarser resolution is used. That is, only the Reynolds-averaged variables are only available at the LES inflow interface, whereas the LES needs turbulent fluctuations to represent the dissipative structure of the flow. Without any additional treatment, the transition into a fully developed turbulent flow region would require a distance from the inlet of roughly 20 to 40 boundary-layer thicknesses. This leads to a large overlapping zone. To obtain the LES inflow data at much shorter adaptation lengths, typically two methods, which generate the turbulent fluctuations, are applied: rescaling methods and synthetic turbulence generation methods.

Rescaling method

Rescaling methods are based on similarity assumptions. Inflow data for a simulation of a turbulent boundary layer is rescaled from recycling station downstream of the inflow to a desired boundary layer thickness [44]. Typically, a simultaneous simulation of turbulent boundary layer flow is set up using a rescaling method from which the flow data is extracted and prescribed at the inflow of the domain of interest. The flow behavior of the additional simulations should be analogous to the inflow of the LES zone, guaranteeing similar turbulent inflow data. Periodic effects can be avoided by having a large distance between the rescaling plane and the inflow boundary [46]. That is, the rescaling method requires a minimum rescaling distance of 7-10 boundary layer thicknesses to give a valid solution with accurate first- and second order statistics [2]. However, turbulent boundary layer with a non-zero pressure gradient or three dimensional effects are not captured accurately due to the non-existing self-similarity. Therefore, in this work a synthetic turbulence generation method is preferred for the inflow data of the LES zone.

Reformulated synthetic turbulence generation method

Synthetic turbulence generation methods are regarded as a more reasonable approach to provide inflow data. Velocity fluctuations are prescribed at the inflow of the LES zone. Based on the previous synthetic eddy method (SEM) developed by Jarrin *et al.* [47] and Pamies *et al.* [48], the reformulated synthetic turbulence generation (RSTG) method by Roidl [2] is applied in this work.

The coherent structures are produced over the LES inflow plane via a superposition of the influence of virtual eddy cores in a virtual volume V_{virt} , which is placed at the LES inlet plane. The virtual eddies populate the virtual volume and connect through it in the mean flow direction. The size of the virtual volume V_{virt} is determined by the boundary layer thickness δ_0 at the LES inflow in the streamwise direction (x) and in the wall-normal direction (y), and the width of the computational domain L_z in the spanwise direction (z), i.e., $V_{virt} = L_z \delta_0^2$. The eddies flow in the streamwise direction and once an eddy passes through the virtual box, a new eddy is created again at the inlet of the virtual box.

A shape function is used to describe the spatial and temporal properties of the artificial turbulent eddies, satisfying the normalization condition [2], such that

$$\frac{1}{2^3} \int_{[-1,+1]^3} (f_{l_x,m,p}(\tilde{x}) f_{l_z,m,p}(\tilde{z}) f_{l_x,m,p}(\tilde{x})^2) d\tilde{x} d\tilde{y} d\tilde{z} = 1 \quad (5.1)$$

5. ZONAL RANS-LES METHOD

where f_l is the shape function with a compact support on $[-l, l]$ and l is a length scale on the order of the integral length scale.

The velocity signal u'_m is obtained by the sum of the contributions $u_m^i(x, y, z, t)$ of all eddy cores N to the velocity field. The virtual eddy cores N are located at x^i, y^i, z^i in the virtual volume. The modified velocity fluctuations [2] are given by

$$u'_m(x, y, z, t) = \sum_{p=1}^P \frac{\sqrt{V_{virt}}}{\sqrt{N}} \sum_{i=1}^N \underbrace{\vartheta_m^i f_{l_x, m, p}(\tilde{x}) f_{l_y, m, p}(\tilde{y}) f_{l_z, m, p}(\tilde{z})}_{u_m^i(x, y, z, t)}, \quad (5.2)$$

with

$$\tilde{x} = \frac{x - x^i}{l_{x, p}}, \quad \tilde{y} = \frac{y - y^i}{l_{y, p}}, \quad \tilde{z} = \frac{z - z^i}{l_{z, p}}, \quad (5.3)$$

where $l_{x, y, z, p}$ denotes the length scale of the eddies in the Cartesian directions. The subscript i and the ϑ^i denote a virtual eddy core and the random sign, respectively. Computing the velocity fluctuations u'_m via the eddies at the LES inflow inlet, the final velocity component [2] is determined by

$$u_m(y, z, t) = u_{RANS, m} + \sum_n A_{mn} u'_m(y, z, t) \quad (5.4)$$

where $u_{RANS, m}$ is the mean velocity component from the upstream RANS zone and A_{mn} is a Cholesky decomposition of the Reynolds stress tensor R_{mn} .

The shear-stress component $\langle u'v' \rangle$ of the Reynolds stress tensor [49] is computed by

$$\langle u'_i u'_j \rangle = \nu_t (\sqrt{2S_{ij}S_{ij}}) = \sqrt{c_\mu} k, \quad (5.5)$$

5.1 Zonal boundary conditions

where the turbulent viscosity ν_t is given by the upstream RANS domain and S_{ij} is the norm of the strain tensor. The strain tensor S_{ij} is given by

$$S_{ij} = \frac{1}{2} \left(\frac{\partial u_i}{\partial x_j} + \frac{\partial u_j}{\partial x_i} \right), \quad (5.6)$$

and the definition of the kinetic energy $k = \frac{1}{2} \langle u_i'^2 \rangle$, such that

$$\langle u'^2 \rangle = 2k = \frac{2\nu_t}{c_\mu} \left(\sqrt{2S_{ij}S_{ij}} \right), \quad (5.7)$$

where c_μ is set to 0.09. This turbulent kinetic energy is isotropic and each component for three dimension is equal, such that

$$\langle u'^2 \rangle = \langle v'^2 \rangle = \langle w'^2 \rangle. \quad (5.8)$$

From the scaling law of Pirozzoli [50] the length scale is computed by

$$l_{\frac{1}{2}} \sim (u_\tau \delta_0)^{1/2} \left(\frac{\partial u}{\partial y} \right)^{-\phi} \quad (5.9)$$

5. ZONAL RANS-LES METHOD

where u_τ is the shear velocity and ϕ is set to 0.5 in this work. The strain tensor S_{ij} and $u_{\tau,max}$ are used to obtain the length scale component of Cartesian coordinates, such that

$$\begin{aligned} l_x(y, z) &= \delta_0 \left(\sqrt{S_{ij} S_{ij}} \right)^{-1/2} \left(\frac{u_{\tau,max}}{\delta_L} \right)^{1/2} \\ l_y(y, z) &= \frac{1}{2} \delta_0 \left(\sqrt{S_{ij} S_{ij}} \right)^{-1/2} \left(\frac{u_{\tau,max}}{\delta_L} \right)^{1/2} \\ l_z(y, z) &= \frac{1}{2} \delta_0 \left(\sqrt{S_{ij} S_{ij}} \right)^{-1/2} \left(\frac{u_{\tau,max}}{\delta_L} \right)^{1/2} \end{aligned} \quad (5.10)$$

where δ_0 is the boundary-layer thickness at the LES inflow. The eddies are convected to the new location in the streamwise direction at every time step via the advection velocity, such that

$$x^i(t+1) = u_{adv} \Delta t + x^i(t) \quad (5.11)$$

where u_{adv} is set to u_∞ in this work.

The number of eddies needs to be adjusted to suitable values, such that a fully turbulent flow field is obtained without increasing the computational effort too much.

5.1.2 Second zonal interface

The RANS-LES interface at the outflow of the RANS zone is the second boundary condition. The mean pressure of the LES zone downstream is prescribed at the outflow of the RANS zone. The variables of the LES zone are simultaneously time-averaged by an exponential time window approach [44] and can also be spanwise-averaged due to the two-dimensionality of the flow field. By prescribing the pressure, all low frequency and large scale pressure information of the LES zone is transferred into the upstream flow to balance both methods in term of energy conservation. From these processes, the flow behavior between the RANS zone and the LES zone can be smooth.

5.2 Zonal variable exchange

Most fluid flow problems are solved by means of a parallel computation with a number of CPUs to increase the computation speed and overcome memory limitations. To perform

such a computation, the physical domain is split into a number of smaller computational domains and the numerical scheme is locally applied in each subdomain, exchanging at the boundaries with neighboring domains. However, the zonal method requires overlapping zones composed of grids of different resolution. Thus, a simple exchange procedure cannot be applied, making it necessary to develop a parallel zonal exchange procedure. That is, the coarse grid of RANS zones and the fine grid of LES zones must be connected to each other in an appropriate manner such that correct values are prescribed at the inter-zonal boundary surfaces. Furthermore, the grid lines of the meshes in different zones are not always aligned, such that the exchange variables can not be directly obtained via a simple interpolation. In extremely complex cases the RANS domain and LES domain can tilt in totally different directions leading to a difficulties in a direct data exchange. Several techniques have been developed to solve the difficulty of the connection between two domains. In this work, a modified trilinear interpolation approach is used. As typically a large number of computational domains is used, the data exchange operation between the subdomains should be computationally efficient to maintain the parallel computation efficiency. Therefore, a zonal exchange is developed in this work using a Message Parallel Interface (MPI) operation. Two expressions, a donor and a receiver, are introduced to help understand the procedure. The donor denotes the side sending data, and the receiver denotes the side receiving data. This approach is composed of 4 steps and explained in this last subsection.

5.2.1 Trilinear interpolation

To connect grids of different resolution the grids must overlap to a certain amount. However, in most cases, a perfect match of cells of two grids can not always be ensured due to different cell sizes and orientations and is also not always desirable, e.g., the resolution in RANS zones is much coarser than in LES zones, making it difficult to interpolate directly without treatment (see Fig. 5.2). The grid cells are assumed to have the shape of a warped hexahedron, i.e., a random polyhedron with six faces, but a normal trilinear interpolation must be performed on a regular cuboid. Therefore, each cell, containing flow variables at the cell vertices and surrounding a point for which an interpolation is desired, has to first be transformed to a cube by means of isoparametric mapping of the trilinear interpolation [51]. For the isoparametric mapping the donor cell variables k_j^i at the eight vertices j of a cube, relative to an arbitrary receiver cell i , can be computed by

$$k_j^i = A_1^i + A_2^i(\xi) + A_3^i(\eta) + A_4^i(\zeta) + A_5^i(\xi\eta) + A_6^i(\xi\zeta) + A_7^i(\eta\zeta) + A_8^i(\xi\eta\zeta) \quad (5.12)$$

5. ZONAL RANS-LES METHOD

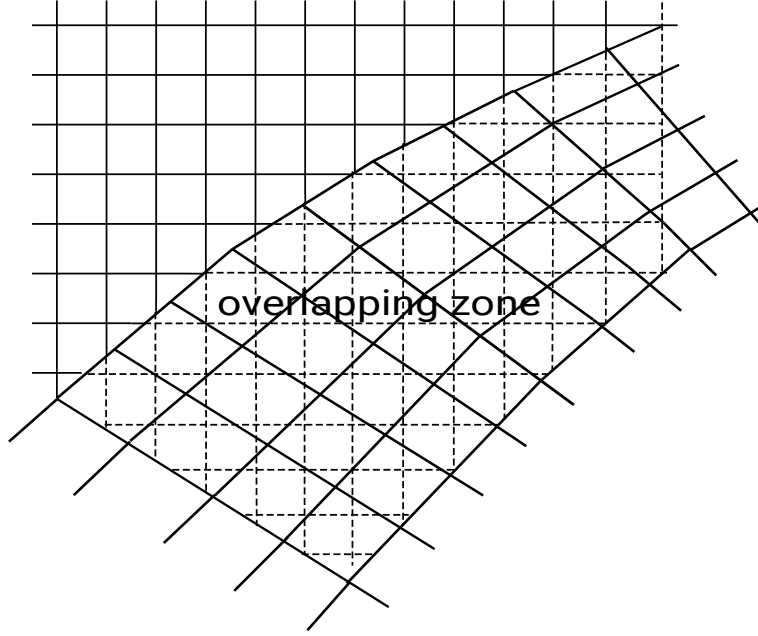


Figure 5.2: Overlapping zone between grids of different resolution. The grids are not perfectly matched due to mesh sizes and orientations.

where A_j , $j = 1, \dots, 8$ are coefficients depending on the variables k_j^i of the donor cells at the vertices of the cube and ξ , η , and ζ are coordinates of the interpolated point P (see Fig. 5.3). The cube is assumed to have a unit edge. As a results, the coordinates in the unit cube are

$$0 \leq \xi, \eta, \zeta \leq 1. \quad (5.13)$$

To simplify a calculation, for instance, an interpolated point at $(\xi, \eta, \zeta) = (0, 0, 0)$ is considered. The donor cell variables for eight vertices can be computed by

$$\begin{aligned} k_1^i &= A_1^i \\ k_2^i &= A_1^i + A_2^i \\ k_3^i &= A_1^i + A_4^i \\ k_4^i &= A_1^i + A_2^i + A_4^i + A_6^i \\ k_5^i &= A_1^i + A_3^i \\ k_6^i &= A_1^i + A_2^i + A_3^i + A_5^i \\ k_7^i &= A_1^i + A_3^i + A_4^i + A_7^i \\ k_8^i &= A_1^i + A_2^i + A_3^i + A_4^i + A_5^i + A_6^i + A_7^i + A_8^i. \end{aligned} \quad (5.14)$$

Then, the coefficients A_j^i corresponding to each vertice are computed by

$$\begin{aligned}
A_1^i &= k_1^i \\
A_2^i &= -k_1^i + k_2^i \\
A_3^i &= -k_1^i + k_5^i \\
A_4^i &= -k_1^i + k_3^i \\
A_5^i &= k_1^i - k_2^i + k_5^i + k_6^i \\
A_6^i &= k_1^i - k_2^i - k_3^i + k_4^i \\
A_7^i &= k_1^i - k_3^i + k_5^i + k_7^i \\
A_8^i &= -k_1^i + k_2^i + k_3^i - k_4^i - k_5^i - k_6^i - k_7^i + k_8^i.
\end{aligned} \tag{5.15}$$

The mapping of the warped hexahedron to a cube can be transformed from (ξ, η, ζ) to (X, Y, Z) which is called a mapping coordinate, such that

$$\begin{aligned}
X &= A_1^i + A_2^i(\xi) + A_3^i(\eta) + A_4^i(\zeta) + A_5^i(\xi\eta) + A_6^i(\xi\zeta) + A_7^i(\eta\zeta) + A_8^i(\xi\eta\zeta) \\
Y &= B_1^i + B_2^i(\xi) + B_3^i(\eta) + B_4^i(\zeta) + B_5^i(\xi\eta) + B_6^i(\xi\zeta) + B_7^i(\eta\zeta) + B_8^i(\xi\eta\zeta) \\
Z &= C_1^i + C_2^i(\xi) + C_3^i(\eta) + C_4^i(\zeta) + C_5^i(\xi\eta) + C_6^i(\xi\zeta) + C_7^i(\eta\zeta) + C_8^i(\xi\eta\zeta)
\end{aligned} \tag{5.16}$$

where the constants, $A_j^i, B_j^i, C_j^i, j = 1, \dots, 8$ are determined by the corresponding values of the coordinates at the vertices in physical space according to eq. 5.15. The eq. 5.16 for the mapping coordinates (X, Y, Z) of P is valid for any point in the interior of the hexahedron, yielding a non-linear system of equations. To solve a problem of the non-linear system, a Newton iteration can be applied. As a result, each component (Φ_1, Φ_2, Φ_3) of the corresponding mapping coordinates (X, Y, Z) can be computed by

$$\begin{aligned}
\Phi_1 &= (C_1^i - X) + C_2^i(\xi) + C_3^i(\eta) + C_4^i(\zeta) + C_5^i(\xi\eta) + C_6^i(\xi\zeta) + C_7^i(\eta\zeta) + C_8^i(\xi\eta\zeta) \\
\Phi_2 &= (D_1^i - Y) + D_2^i(\xi) + D_3^i(\eta) + D_4^i(\zeta) + D_5^i(\xi\eta) + D_6^i(\xi\zeta) + D_7^i(\eta\zeta) + D_8^i(\xi\eta\zeta) \\
\Phi_3 &= (F_1^i - Z) + F_2^i(\xi) + F_3^i(\eta) + F_4^i(\zeta) + F_5^i(\xi\eta) + F_6^i(\xi\zeta) + F_7^i(\eta\zeta) + F_8^i(\xi\eta\zeta).
\end{aligned} \tag{5.17}$$

5. ZONAL RANS-LES METHOD

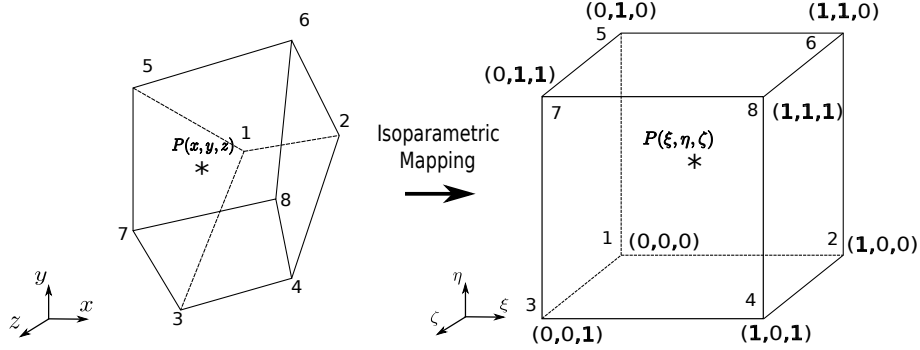


Figure 5.3: Isoparametric Mapping is applied for the trilinear interpolation. The warped hexahedron is remapped onto the cube. The exchange variables at point $P(\xi, \eta, \zeta)$ are interpolated from the variables at the eight points 1, ..., 8 in a neighboring domain.

5.2.2 Grid connection for the zonal method

The modified trilinear interpolation method allows the connection of arbitrarily overlapping grids. The zonal method can be applied to more challenging cases, such as tilted grids or grids with strongly different curvature (see Fig. 5.4). Such complex connections between RANS and LES grids can occur at turbulent flow applications since geometries can be strongly curved.

First, the physical coordinates of the ghost cells in the receiver domain at the zonal boundary surface are gathered and broadcasted to all domains by a communication operation. Since a parallel approach is pursued in this work, the physical coordinates are locally stored for each domain. Each domain will then locally start a lookup for suitable interpolation partners for the received zonal boundary coordinates. After the receiver cell examines the distance from the donor cells (eight points), each receiver cell builds a cube surrounding the donor cells for the eight vertexes. All of the receiver cells find the interpolated donor cells until nearest cells are found via a fallback procedure. Then, the number and locations of donor and receiver domains are identified by help of the trilinear interpolation procedure, since the nearest cells are known for each local receiver domain. It also allows a zonal exchange to set up before a main loop of a computation starts. To avoid a order of the exchange variables to be mixed up, a map-cellId approach is applied. The map-cellIds can keep track of the order of cells and are stored in each receiver domain on zonal boundary conditions. From this procedure the local domains that possess zonal boundary conditions can be connected. The connection procedure for the zonal boundaries is executed only once at the initialization of the solver.

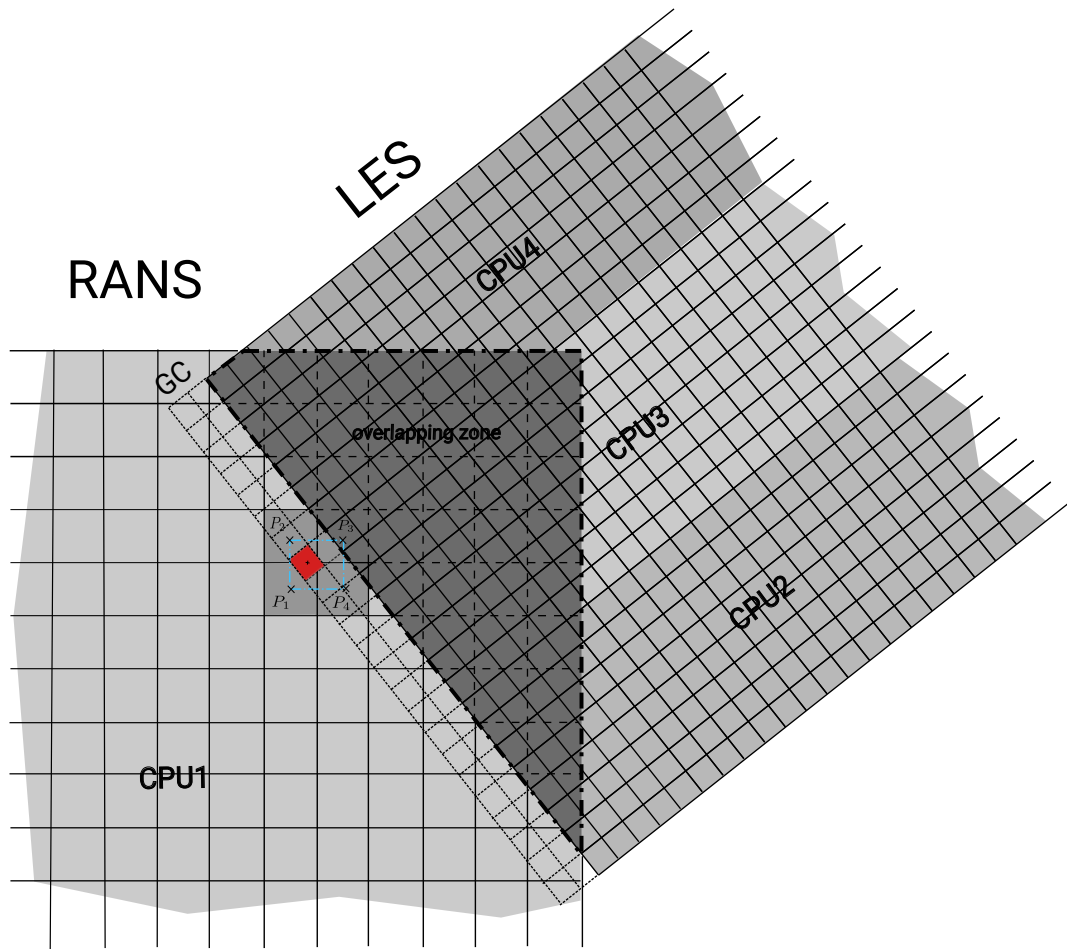


Figure 5.4: Zonal grid connection in a complex case.

5. ZONAL RANS-LES METHOD

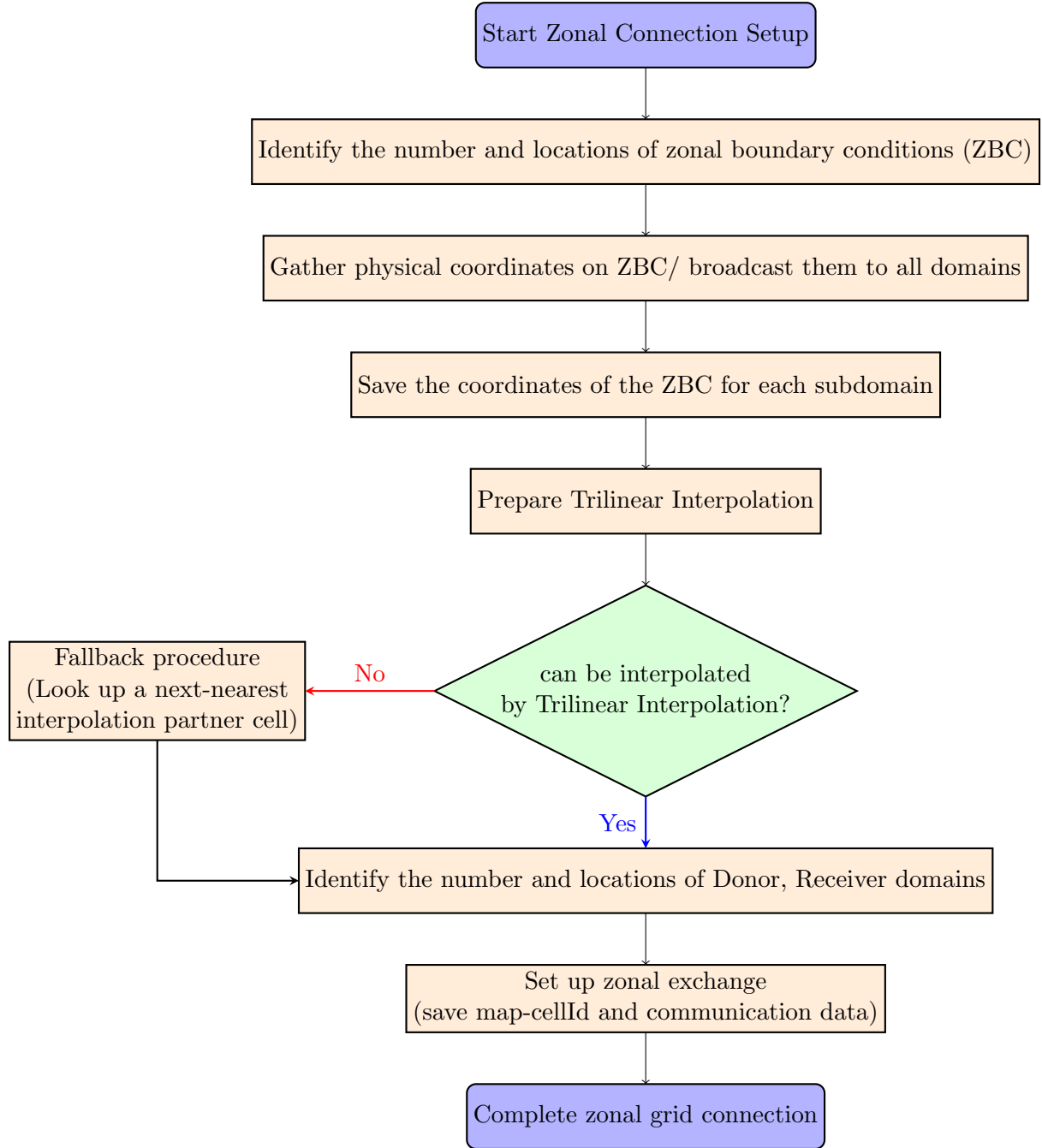


Figure 5.5: Schematic diagram of the zonal grid connection.

5.2.3 Zonal exchange

To avoid high additional computational costs an exchange of data at the zonal boundaries needs to be computationally efficient, such that only the necessary variables are handed over to only the domains that require them. The data exchange should be locally fulfilled in each subdomain. To accurately capture pressure frequency of the flow and simultaneously reflect the flow, zonal exchange should be simultaneously implemented at every time step after the initialization of the computation. To satisfy such a computation for the zonal method, the zonal exchange technique is developed in this work. The zonal exchange approach is composed of the four steps, which are gather, send, receive and scatter. After the grids were connected at the solver start-up, every local domain has the information on which domains belong to the zonal boundary conditions. Previously, the number of receiver cells and donor cells were computed, based on searching via building hexahedrons of the trilinear interpolation. The donor domains eventually obtained the exchange information at the zonal grid connection step; e.g. the number of corresponding receiver domains and the number of required cells of donor domains. The donor domains first interpolate all information on the receiver cells, computing coefficient of the trilinear interpolation, and then gather the receiver cells to prepare the sending of the data to receiver domains. That is, the gathered interpolated variables are sent to the receiver domains, while the receiver domains obtain the variables from donor domains. Due to the computation memory limitation and speed, the use of global MPI operations that require large memory is prohibited; e.g. `MPI_Allreduce`. Finally, the receiver domains obtain the interpolated variables and then scatter the data into the ghost cells to where appropriate further computations to ensure correct boundary values. The zonal exchange is performed only every 5-50 time steps, depending on how quickly the behavior of the RANS zone changes, since it is computationally expensive. A schematic diagram of the zonal exchange procedure is shown in Fig. 5.6.

To enhance the understanding of this zonal exchange procedure, a simplified example is considered using only five ranks (see Fig. 5.7). After the interpolated partners are found and the interpolation coefficients are computed, the interpolated variables PN ($P1, P2, \dots, PN$) in ranks 0, 1, and 2 of the RANS zone are collected in the ghost cells using cell indexes. The variables obtained from each rank of the RANS zone are sent to rank 3 and rank 4 separately. The received variables within the LES zone are scattered to the ghost cells of each rank of the LES zone.

5. ZONAL RANS-LES METHOD

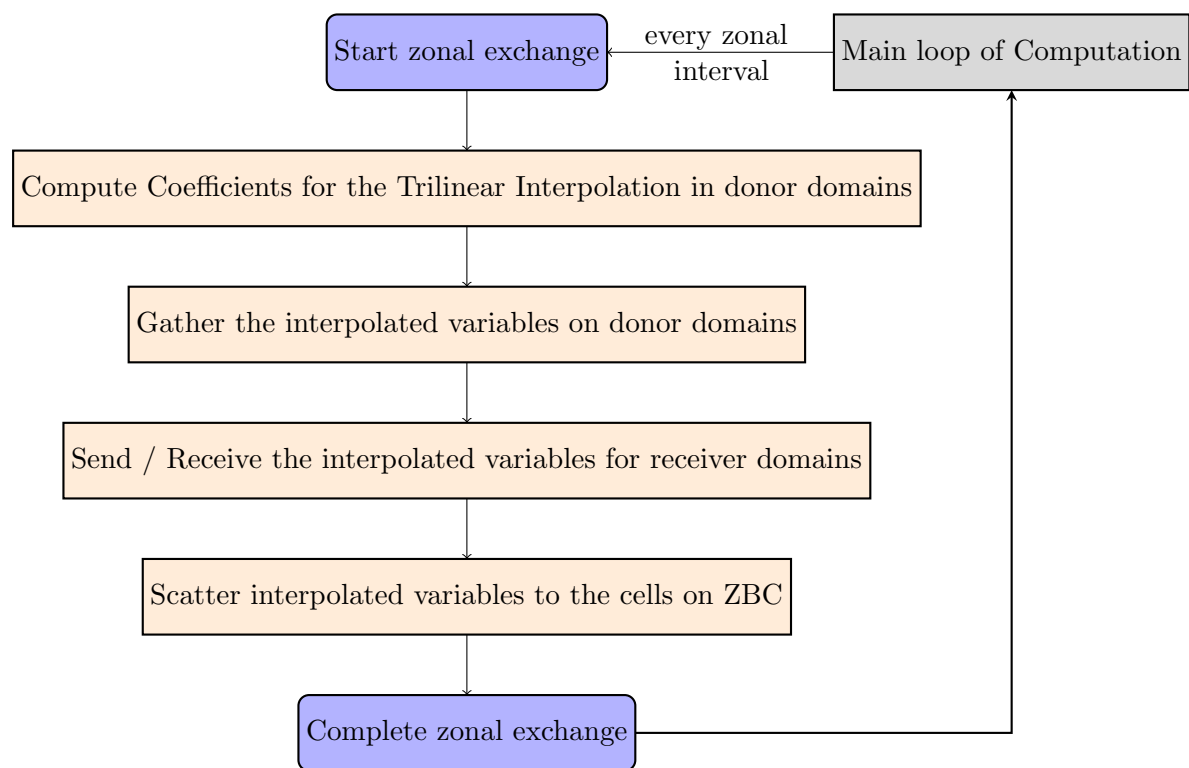


Figure 5.6: Schematic diagram of the zonal exchange procedure.

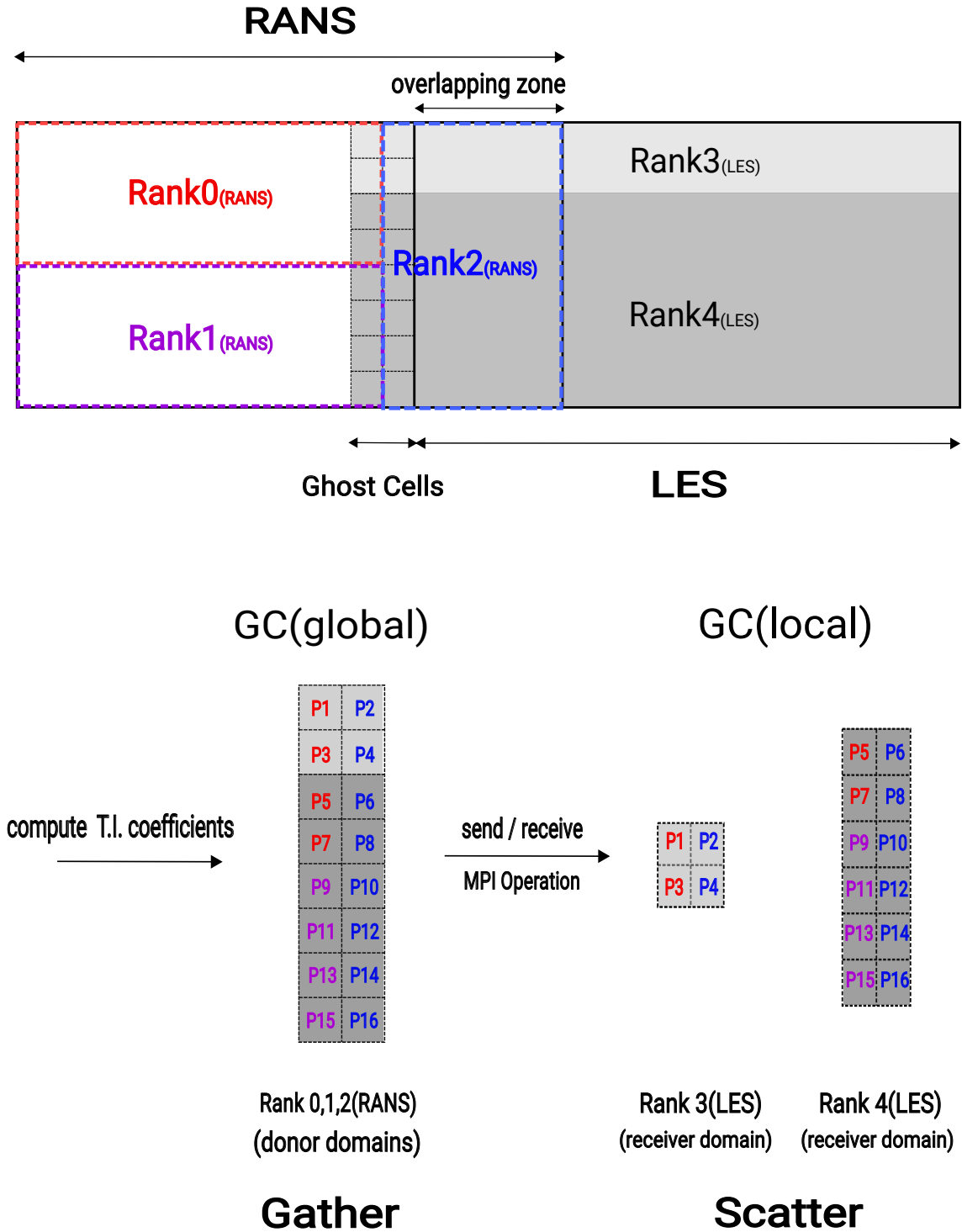


Figure 5.7: zonal exchange procedure which consists of a gather, a send/receive and a scatter in the case of 5 ranks of the zonal method.

5. ZONAL RANS-LES METHOD

6

Results

In this chapter the zonal RANS-LES method is validated in a simulation of a zero-pressure gradient flat-plate turbulent boundary layer flow. To apply the method to a more challenging flow scenario, a simulation of a space launcher is performed. To ensure the accuracy and reliability of the developed zonal method of this work, solutions for a pure RANS and a pure LES are referred to the flat plate flow. In addition, the reference solution with TFS (the flow solver) is compared for the space launcher simulation.

6.1 Validation of the zonal method in a flat plate flow

Validation of the zonal method for a zero-pressure gradient flow is performed in a flat plate. The flat plate flow is universally used to evaluate a fluid flow. First, a computational set-up is described. Then, the results are compared with the pure RANS, the pure LES, theoretical values and DNS data to analyze the developed zonal method.

6.1.1 Computational set-up

Zone	Type	Number of Cells				Δx^+	Δy^+	Δz^+
		i	j	k	Total			
1	RANS	93	141	35	458,955	60	1	20
2	LES	278	141	69	2,704,662	20	1	10

Table 6.1: Grid information of the zonal test case.

A simulation for the validation is performed in the ZFS environment developed at AIA in RWTH university. Two different grids are set up on the flat plate, overlapping two zones, i.e., the RANS zone and the LES zone. To accurately capture all relevant turbulent scales and guarantee an accurate solution of the zonal method, the grid resolution in the

6. RESULTS

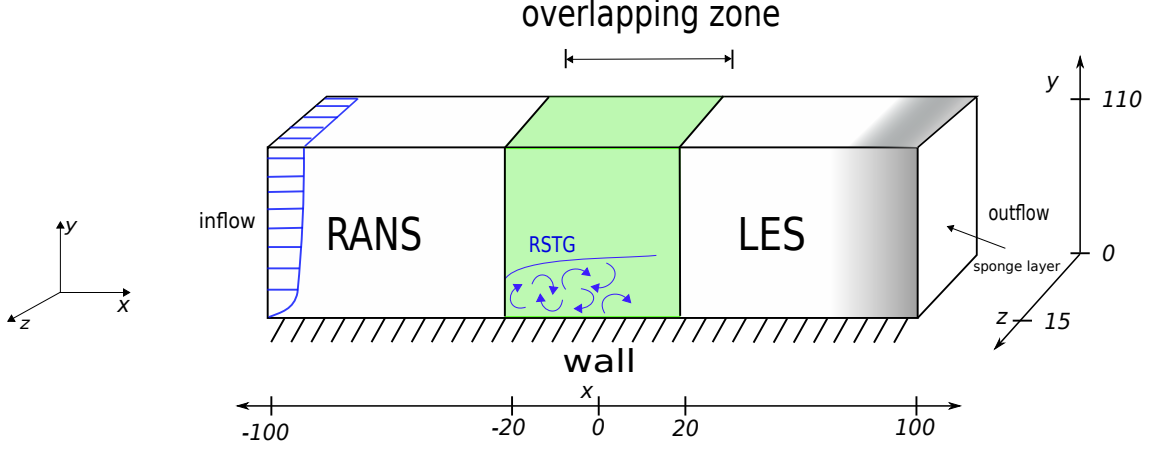


Figure 6.1: Zonal test case setup for the RANS-to-LES transition using the RSTG method.

LES zone has to be finer than in the RANS zone. Furthermore, a higher resolution in wall-normal direction is required near the wall. However, in order to use the box filter function (see Eq. 3.27) a grid size is restricted to be smaller than a specific value. As a result, a more straightforward approach to handle the grid size is that a cell coordinate is based on the momentum thickness Reynolds number using the factor $\Delta S = Re_{\theta}^{-7/8} \sqrt{\frac{2}{0.024}}$, such that

$$x^+ = \Delta x^+ \Delta S, \quad y^+ = \Delta y^+ \Delta S, \quad \text{and} \quad z^+ = \Delta z^+ \Delta S. \quad (6.1)$$

The cell sizes in inner units in the LES zone are set to $\Delta x^+ = 20.0$, $\Delta y^+|_{wall} = 1.0$ and $\Delta z^+ = 10.0$. The cell sizes in the wall-normal direction (y) grow with increasing wall-distance, i.e., $\Delta y_{j+1} = 1.03 \Delta y_j$ from $y = 0$ to the thickness $y = 0.3\delta_0$. In the region between $y = 0.3\delta_0$ and $y = \delta_0$ the growth-factor is 1.05 and above $y = \delta_0$ the factor is set to 1.1, since the far field region from the wall is not necessary to be finely resolved. The cells in the RANS zone are stretched by a factor of three in the streamwise and by a factor of two in the spanwise direction. That is, the total number of cells in the LES zone is $278 \times 141 \times 69 = 2,704,662$ and the total number of cells in the RANS zone is $93 \times 141 \times 35 = 458,955$ in i, j, and k direction, respectively (see Table 6.1). The computational domain grid of the zonal test case is shown in Fig. 6.2.

The RANS profile at the inflow has a displacement thickness of $\delta_1 \approx 1$ and the inflow variables are interpolated from a fully developed RANS profile which is created by a prior simulation using rescaling method. Furthermore, the Reynolds number based on the momentum thickness is set to $Re_{\theta, x=0} \approx 1000$ at $x = 0$. This results in $Re_{\theta, inflow} = 808$ and a boundary layer thickness of $\delta_{0, inflow} = 7.28$. At the outflow of the LES domain, a sponge layer is applied to avoid spurious oscillations. A sponge thickness is set to 20. The RSTG method is used for the generation of velocity fluctuations at the inflow of the LES

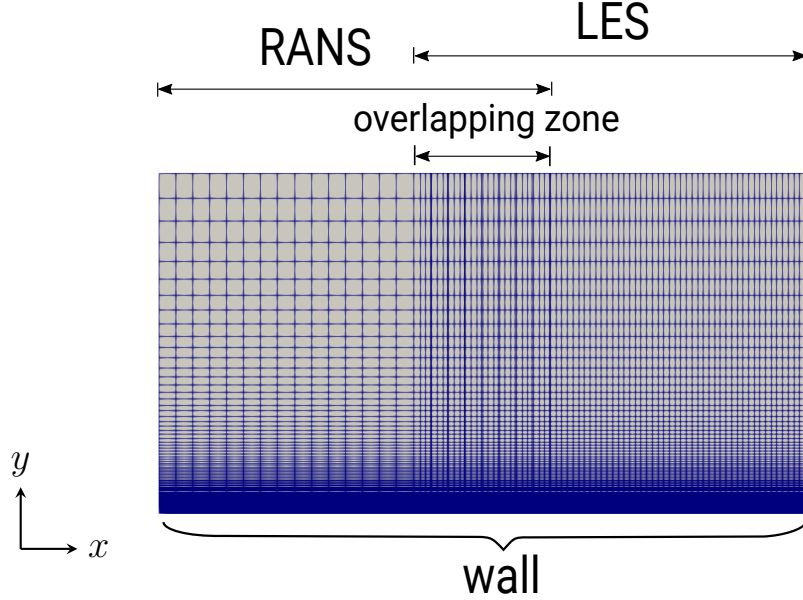


Figure 6.2: Computational domain of the zonal test case; every 4th grid point is shown.

zone with $N = 100$ eddies (see Eq. 5.2) that simultaneously populate the virtual volume $V_{virt} = 1124.65$ and $\psi = 0.5$, for which a quick transition to fully developed turbulent boundary layer flow was found in previous works. The zonal exchange is performed every 5 time steps, as this operation is quite expensive. This Interval should be as long as possible but the result should be reasonable, which can be valid for which the variables are exchanged. The CFL number is related to the time step and causes whether the numerical schemes are divergent or convergent. The CFL number is set to a value of 2.

The time steps of the flow simulation are given in convective units Δt which is defined as a ratio of the characteristic length δ_2 and the streamwise velocity in the freestream, such that $\Delta t_{conv} = \frac{\delta_2}{u_\infty}$ in this work. The average is sampled every 0.01 convective units for a time of 2300 convective units. The temporal average is then spatially averaged in the spanwise direction.

The set-up parameters are summed up in the following table 6.2.

6.1.2 Comparison and analysis of the results

In order to investigate the accuracy and reliance of the zonal RANS-LES method, a pure RANS and a pure LES are used in setups of the same size as the zonal setup. For the pure RANS and the pure LES the same inflow parameters are used. The desired boundary layer thickness at the pure LES inflow is obtained by the rescaling method.

6. RESULTS

Parameter	Value
Ma_∞	0.2
$Re_{\theta, inflow}$	808
CFL	2.0
Number of eddies N for RSTG	100
Virtual box volume	1124.65
Length scale parameter ψ	0.5
Zonal exchange interval(timesteps)	5

Table 6.2: Setup parameters of the zonal test case

Furthermore, DNS data by Schlatter and Orlu [52] is used to evaluate the results. First, the instantaneous velocity u component at the $Re_\theta = 1006$ and the streamwise development of the velocity u component are graphically shown in comparison with pure RANS and pure LES. Subsequently, the skin friction coefficient c_f , and shape factor H are plotted in the streamwise direction are compared to the results from pure RANS, pure LES, DNS data, and the theoretical values. Finally, the mean velocity in the streamwise direction and Reynolds stress tensor components at different streamwise positions are investigated.

Instantaneous velocities generated by RSTG method

The instantaneous velocity streamwise field of the zonal method is compared to the one from the pure RANS simulation and from the pure LES in Fig. 6.3. By means of the zonal exchange technique the mean variables of RANS domains are transferred into the LES domains. Then, velocity fluctuations are superposed on the mean variables of the RANS zone by the RSTG method. As a result, turbulent fluctuations downstream of the LES inflow can be observed (see Fig. 6.3c). Fig. 6.4 shows the fluctuations of the zonal method in the y-z plane at $x/\delta_0 = 1.7$. Fig. 6.14a provides that a fully turbulent flow field can be observed for the pure LES and the zonal simulation, whereas, as expected, a steady flow field is obtained in the pure RANS simulation.

6.1 Validation of the zonal method in a flat plate flow

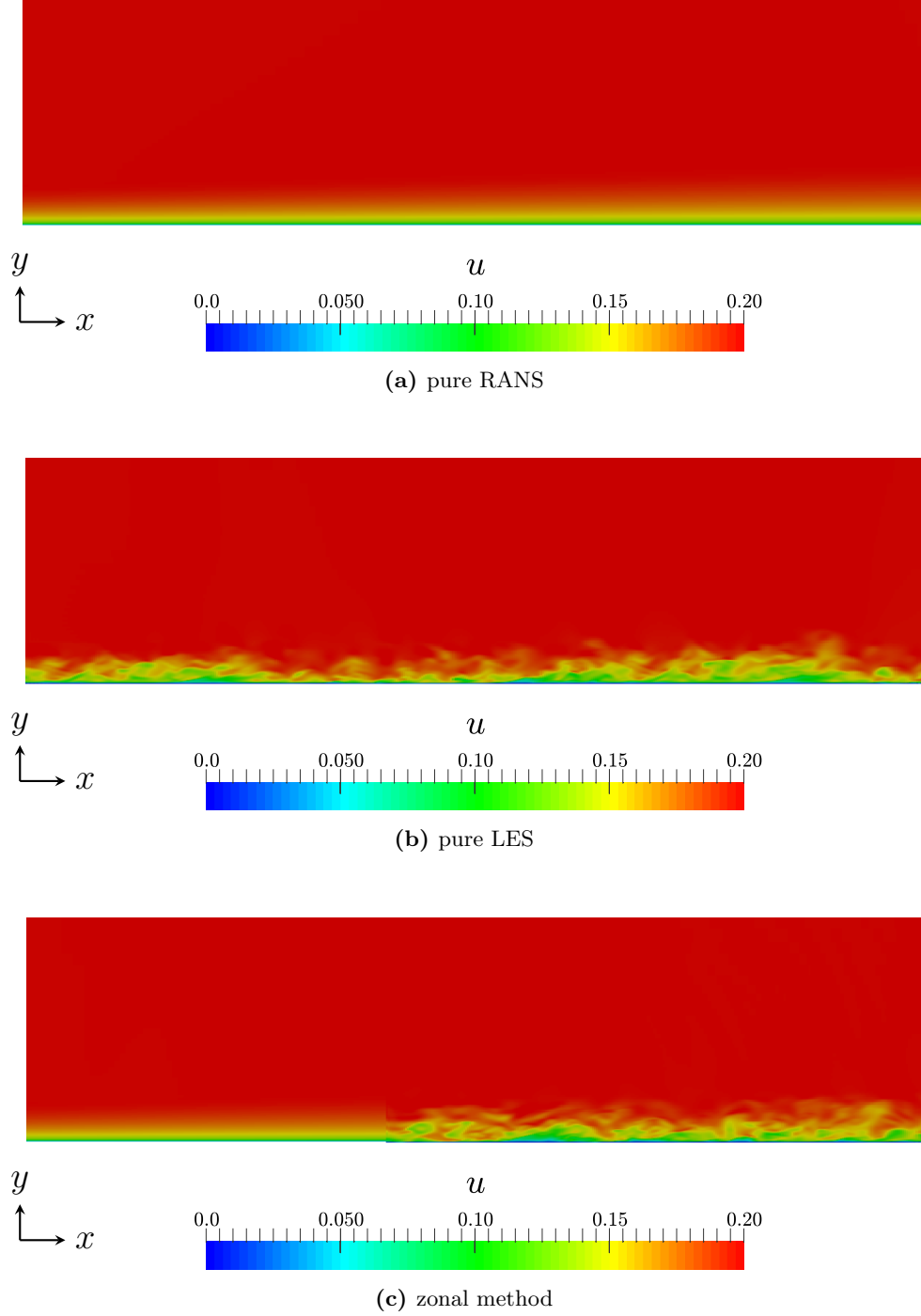


Figure 6.3: Streamwise development of the instantaneous velocity component u for the pure RANS (a), the pure LES (b), and the zonal RANS-LES method (c).

6. RESULTS

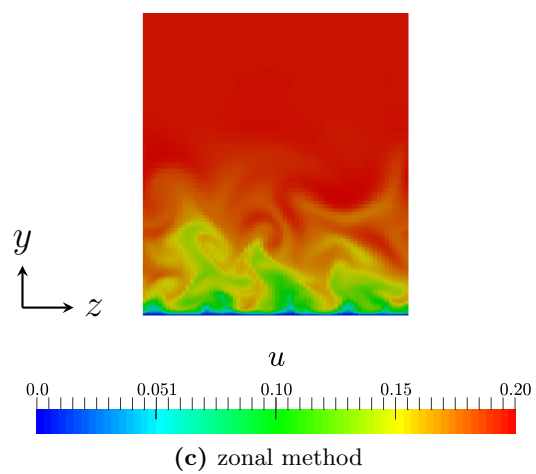
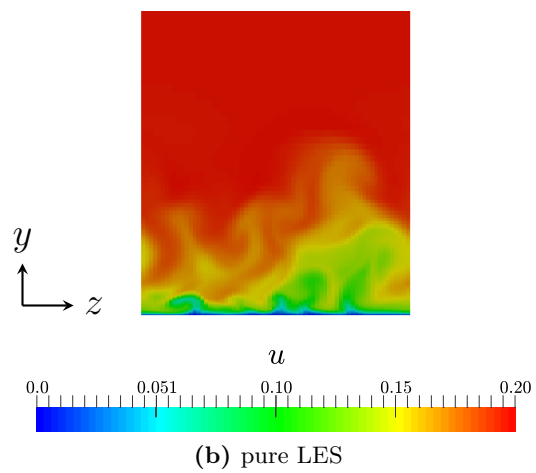
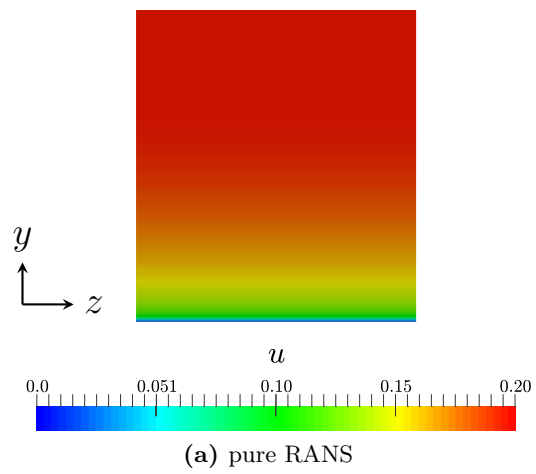


Figure 6.4: Plots of the instantaneous streamwise velocity component u at the streamwise position $x/\delta_0 = 1.7$, where $Re_\theta = 1006$

Momentum thickness Reynolds number

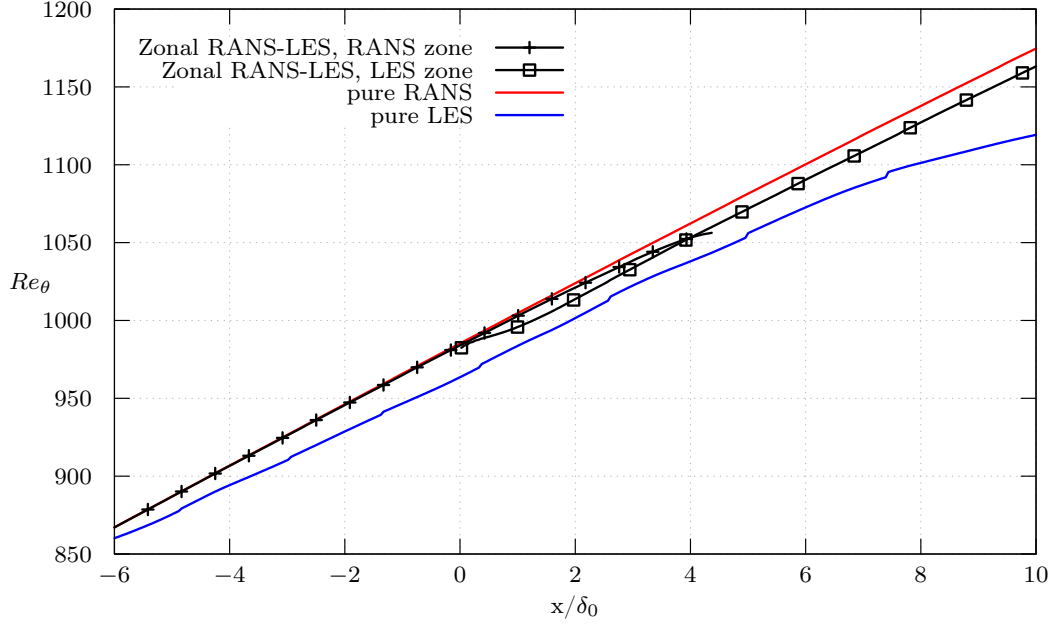


Figure 6.5: Streamwise development of the Reynolds number based on momentum thickness Re_θ vs. x/δ_0 of the zonal method, the pure LES and the pure RANS. The overlapping zone is from $x/\delta_0 = 0$ to $x/\delta_0 = 4.5$.

Different types of the boundary layer thicknesses are used to characterize the height of the turbulent boundary layer. However, only the displacement thickness δ^* and the momentum thickness θ are good quantitative measures, whereas the δ_{99} thickness, i.e., the height where the flow reaches 99 % of the freestream velocity, is rather arbitrary. The momentum thickness θ is computed by

$$\theta = \int_0^\infty \frac{u}{u_\infty} \left(1 - \frac{u}{u_\infty}\right) dy, \quad (6.2)$$

and Reynolds number based on the momentum thickness is defined as

$$Re_\theta \equiv \frac{u_\infty \theta}{\nu}. \quad (6.3)$$

6. RESULTS

Fig. 6.5 shows the streamwise development of the momentum thickness Reynolds number Re_θ for the zonal method and the pure RANS simulation and the pure LES. The flow parameters of the RANS and the LES were set to obtain a boundary layer of similar height as in the zonal setup. In the overlapping zone of the zonal method, both distributions of the RANS zone and the LES zone show very high agreement. The thickness of the pure RANS simulation and the pure LES show the same gradient as the zonal method, however, the distribution in the LES zone of the zonal simulation shows higher agreement over the whole domain. Therefore, it can be assumed that the two zones of the zonal method are smoothly connected and show a high level of agreement with the other methods.

Skin friction coefficient c_f

The skin friction coefficient c_f is a very sensitive parameter that can quantitatively measure the viscous influence of the wall and therefore the drag. The skin friction coefficient is defined as

$$c_f(x) = 2 \frac{\tau_w(x)}{\rho u_\infty^2}, \quad (6.4)$$

where τ_w is the wall-shear stress. A empirical distribution of the skin friction coefficient is given by Smith, based on the momentum thickness Reynolds number, such that

$$c_f(x) = \frac{0.024}{\sqrt[4]{Re_\theta}}. \quad (6.5)$$

Fig. 6.6 shows the streamwise development of the skin friction coefficient for the zonal method, compared to the pure RANS, the pure LES, DNS, and theoretical values. The theoretical values are based on the Eq. 6.4 and the single point is obtained from DNS [52].

The values of c_f in the RANS zone of the zonal method exhibit an almost linear behaviour with a deviation of 2-3% from the theoretical values. The constant deviation in the RANS zone can be caused by the RANS model parameters used. That is why the pure RANS has the same deviation from the theoretical values. Unlike in the RANS zone, due to the RSTG the c_f value rises steeply at the inflow of the LES zone, i.e., $x/\delta_0 = 0$. However, downstream of the inflow of the LES zone, the sudden increase disappears and an average 2-3% deviation from the theoretical value is maintained in the streamwise direction with good agreement with values from the pure LES. The DNS single point at $x/\delta_0 = 1.7$ is well-matched by the LES zone of the zonal method, even though the synthetic turbulence is not fully developed in the LES zone.

To exchange realistic data back to the upstream RANS domain, i.e., the pressure at

6.1 Validation of the zonal method in a flat plate flow

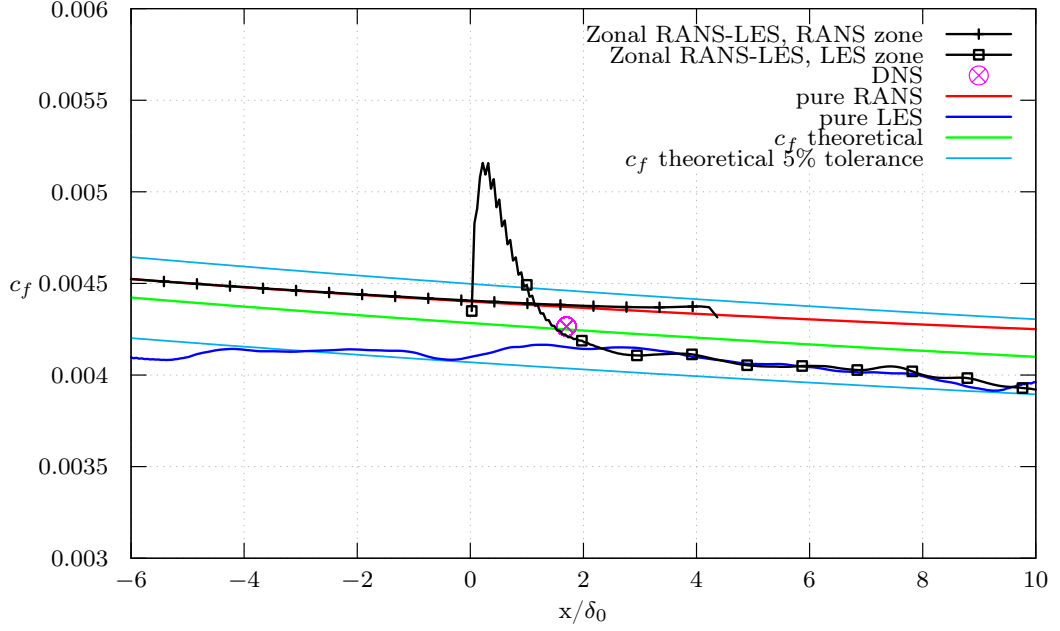


Figure 6.6: Streamwise development of the skin friction coefficient c_f vs. x/δ_0 of the zonal method, the pure RANS, the pure LES, theoretical values, and the DNS at the point $Re_\theta = 1006$ [52]. The overlapping zone is from $x/\delta_0 = 0$ to $x/\delta_0 = 4.5$.

$x/\delta_0 = 4.5$, a sufficient length of the overlapping zone is required. It is observed that the c_f value at the position $x/\delta_0 \approx 2$ in the LES zone of the zonal method is already recovered and has the small derivation from the pure LES. It is concluded that the zonal exchange is implemented with a satisfying agreement.

6. RESULTS

Shape factor

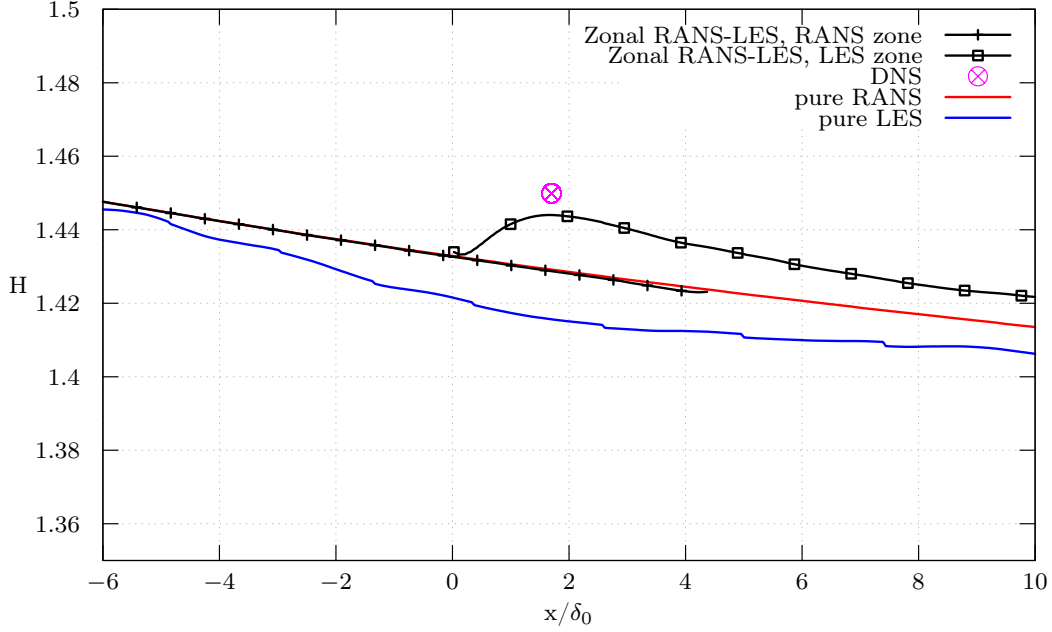


Figure 6.7: Streamwise development of the shape factor H vs. x/δ_0 of the zonal method, the pure RANS, the pure LES, and the DNS single point at the $Re_\theta = 1006$ [52]. The overlapping zone is from $x/\delta_0 = 0$ to $x/\delta_0 = 4.5$.

The shape factor $H = \delta_1/\delta$ reflects the solidity of the wall-normal distribution of the boundary layer. A high shape factor is observed in laminar flows and flows with strong adverse pressure gradients. That is, flow separations show a high shape factor. Here, the shape factor exhibits the low value due to the zero-pressure gradient flow.

Typically, in a zero-pressure gradient flow the value of $H = 2.59$ (Blasius boundary layer) is typical of laminar flows, whereas $H = 1.3 - 1.5$ is typical of turbulent flows [53]. In Fig. 6.7, the shape factor distribution is within typical values of turbulent flows. Furthermore, the plots shows a good collapse in the overlapping zone from $x/\delta_0 = 0$ to $x/\delta_0 = 4.5$. In addition, the similar gradients of the plots show that the flow in two zones behaves in a similar manner. The discrepancy between the pure LES and the LES zone in the zonal method steadily becomes lower in the downstream direction. The value of the LES zone at $x/\delta_0 = 1.47$ deviates slightly from DNS single data at $Re_\theta = 1006$, i.e., only a deviation of 0.7%, even though the position is located only $\Delta x = 1.7\delta_0$ downstream of the inflow LES. Consequently, the shape factor distribution shows a satisfying agreement with results from the pure RANS, the pure LES, and DNS data.

Mean velocity distribution

The mean streamwise velocity distribution in the LES zone is depicted in Fig. 6.8 and is compared to the results of the pure RANS, the pure LES, theoretical values, and DNS data. The velocity is non-dimensionalized by the friction velocity u_τ and plotted in the wall-normal direction, such that $y^+ = \frac{yu_\tau}{\nu}$ in the wall-normal direction and $u^+ = \frac{u}{u_\tau}$ in streamwise direction. In contrast to the laminar boundary layer, the turbulent boundary layer can be split into two different regions, the inner layer and the outer layer (see sec. 2.3). In the region near the wall, i.e., the inner layer the velocity is linearly proportional to the distance from the wall, therefore in the semi-logarithmical plot (Fig. 6.8) it appears curved in the viscous sublayer and behaves linearly in the defect region. The theoretical values are plotted, such that $u^+ = y^+$ in the viscous sublayer region. In the defect region where the viscous effect is not influential in far-field from the wall, it is given by $u^+ = \frac{1}{\kappa} \ln(y^+) + B$ with $\kappa = 0.41$ and $B = 5.5$.

Fig. 6.8 shows the averaged streamwise velocity distribution at the streamwise position

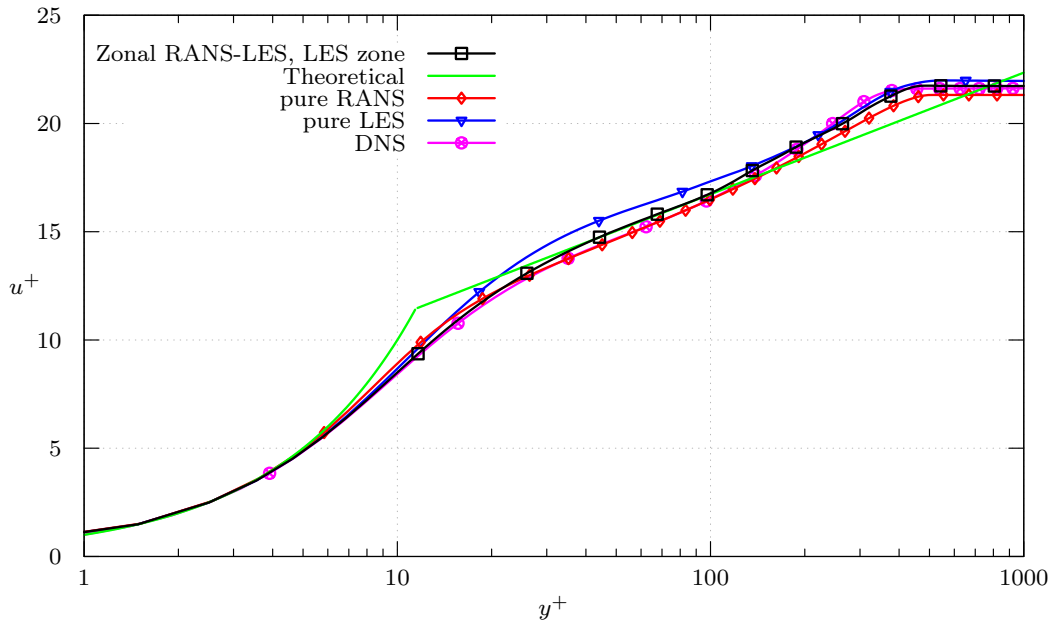


Figure 6.8: Velocity u^+ at the position $x/\delta_0 = 1.7$, $Re_\theta = 1006$ in a logcale of x-axis of the pure LES, the theoretical values at the corresponding Re_θ , and DNS [52].

$x/\delta_0 = 1.7$, which is corresponding to $Re_\theta = 1006$ in order to compare with the available DNS data. The the mean values at the RANS-to-LES transition are appropriately exchange to the LES downstream and the fluctuations imposed by the RSTG method lead to a fully developed turbulent flow field within a short distance, yielding good agreement with a fulfilled zonal exchange technique.

6. RESULTS

In Fig. 6.9, the averaged streamwise velocities are plotted at different positions, compared to the distribution from the pure RANS, the pure LES and theoretical values. The mean velocity in the pure RANS and pure LES are converged in the streamwise direction, due to the rescaling method. The discrepancy between zonal method and the pure LES at $x/\delta_0 = 1$ is small. However, at position $x/\delta_0 = 3$ the mean velocity distribution is already converged to the distribution from pure LES and pure RANS. The RSTG initial effect already vanishes $x/\delta_0 < 3$. It also exhibits that the reasonable values of LES zone downstream at $x\delta_0 = 4.5$, i.e, at the second zonal boundary (RANS outflow), are transferred to the RANS upstream with good agreement.

6.1 Validation of the zonal method in a flat plate flow

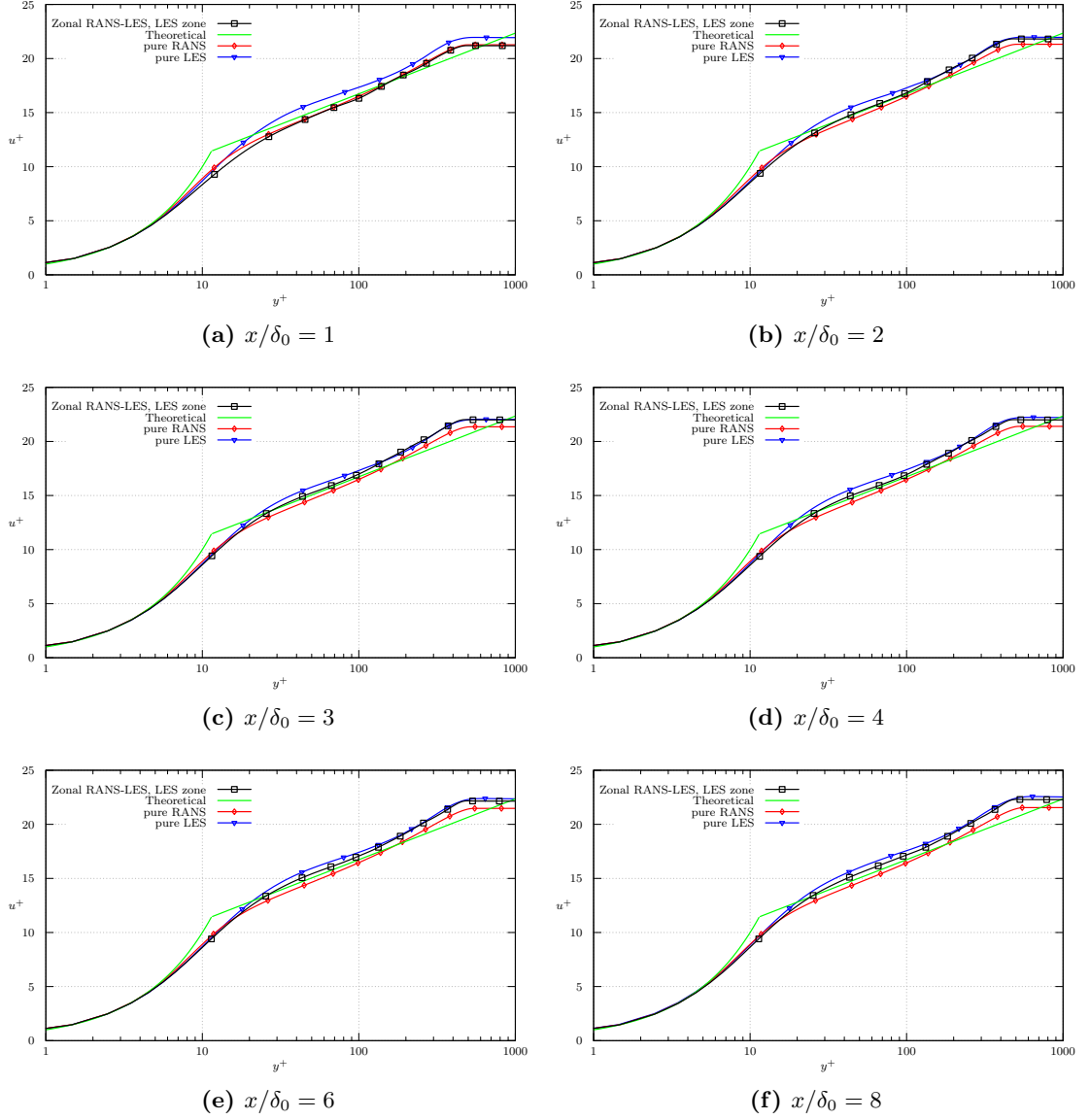


Figure 6.9: Averaged streamwise velocity distribution at different streamwise positions.

6. RESULTS

Reynolds stress distributions

The Reynolds stress components, shown in Fig 6.10, are additional stresses that develop in turbulent flows due to the velocity fluctuations. Here, the Reynolds stresses are normalized by the friction velocity u_τ .

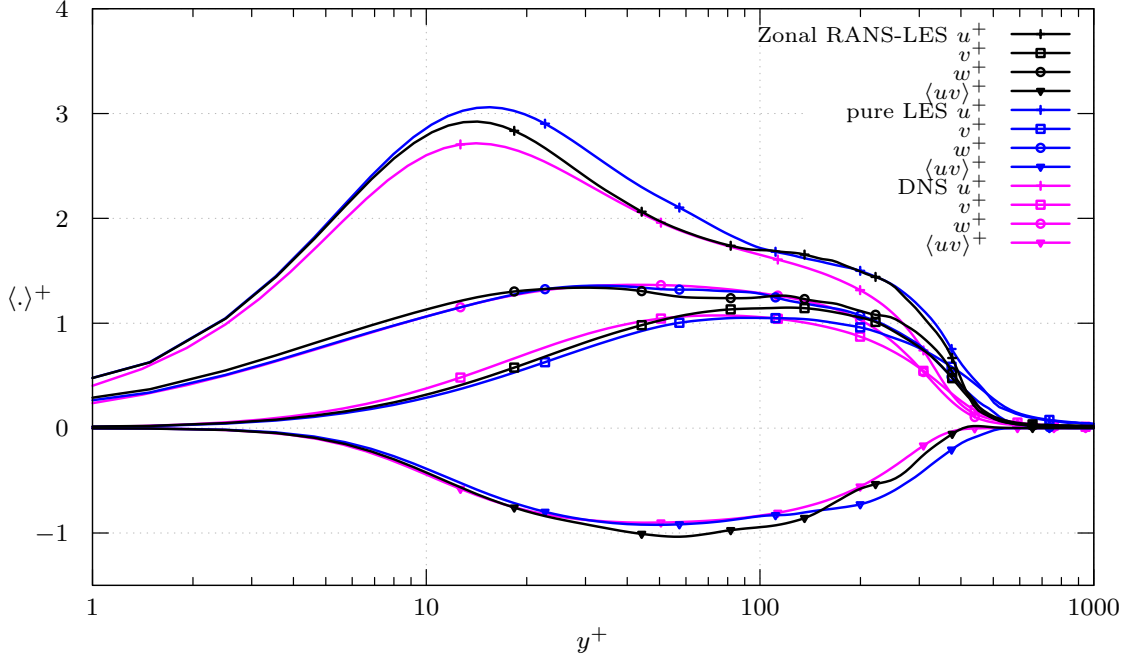


Figure 6.10: Reynolds stress components u_{rms}^+ , v_{rms}^+ , w_{rms}^+ , and $\langle uv \rangle^+$ of the zonal method, the pure LES and the DNS [52] at $Re_\theta = 1006$.

In Fig 6.10, four Reynolds stress components u_{rms}^+ , v_{rms}^+ , w_{rms}^+ , and $\langle uv \rangle^+$ are evaluated at the position $x/\delta_0 = 1.7$, where $Re_\theta = 1006$. The data of the pure LES and DNS is obtained at the corresponding $Re_\theta = 1006$. It can be seen that even distributions from the pure LES show slight derivations from the DNS plot. However, the difference is within an acceptable range and allows for a validation of the zonal method.

In vicinity of the wall, i.e., $y^+ < 100$, the zonal method and the DNS data behave similarly with good agreement with the DNS. However, in the outer region of the turbulent boundary layer the discrepancy between the zonal method and the DNS becomes larger. This might be caused by the short distance downstream of the inflow, thus the larger outer eddies can not sufficiently develop.

Fig. 6.11 exhibits the Reynolds stress components at different streamwise positions. Around the inflow of the LES at $x/\delta_0 = 1$ (Fig. 6.11a) the Reynolds stress components have already slight derivation from the pure LES data. Downstream of the position the position $x/\delta_0 = 2$ the stresses in the zonal method are converged to the distributions of the LES.

6.1 Validation of the zonal method in a flat plate flow

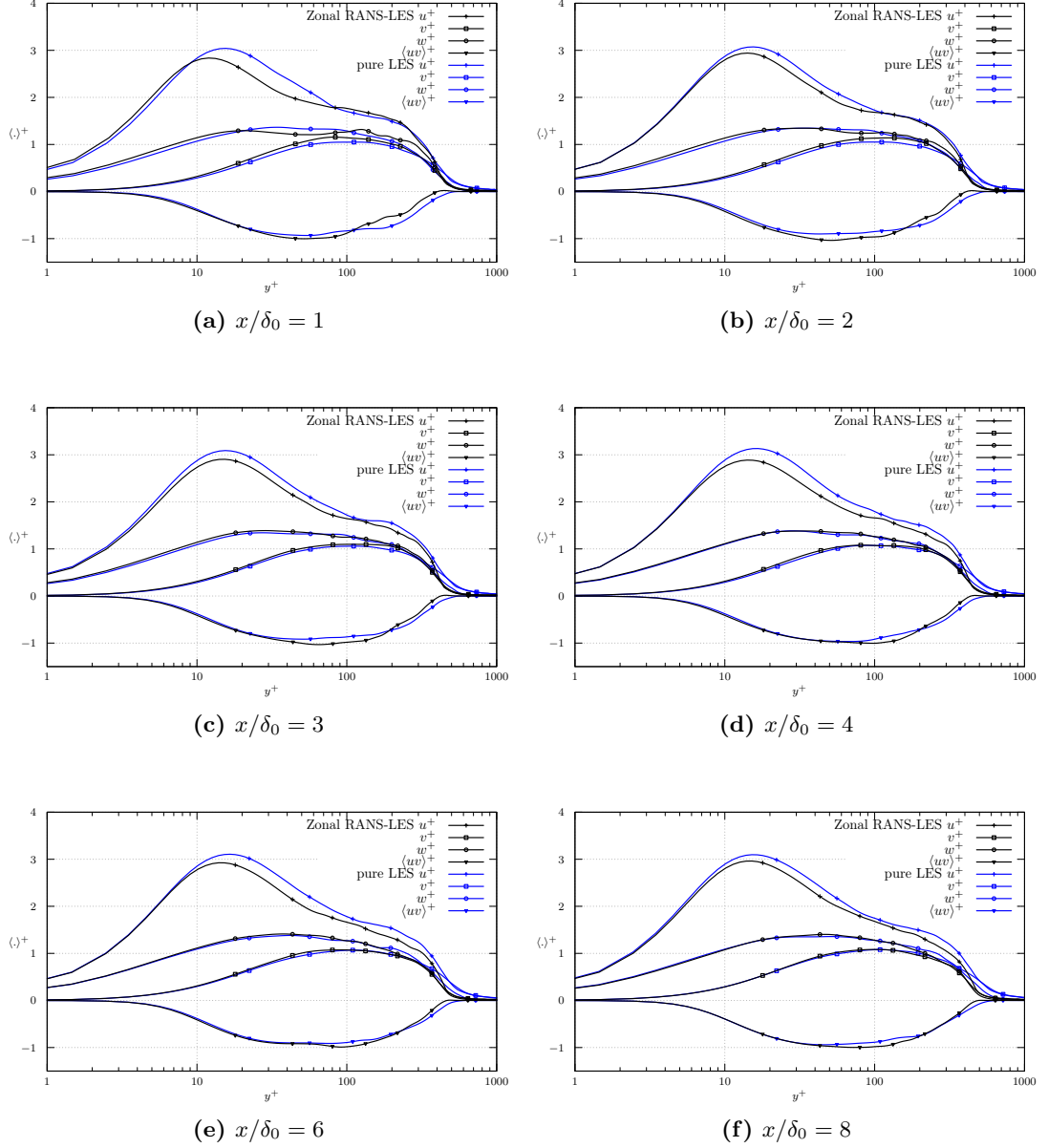


Figure 6.11: Plot of the Reynolds stress components u_{rms}^+ , v_{rms}^+ , w_{rms}^+ , and $\langle uv \rangle^+$ at the different streamwise points. The streamwise positions of the pure LES are at the corresponding Re_θ .

6. RESULTS

6.2 Space launcher simulation

The following space launcher simulation is based on the work by Statnikov *et al.* [54]. However, in this work, the newly implemented zonal RANS-LES method is applied to the same configuration using the ZFS environment.

6.2.1 Computational set-up

Geometry and boundary conditions

The investigated planar generic space launcher is schematically shown in Fig. 6.12. The model is composed of a long shock-free main body and a backward facing step (BFS). The skin of the main body and of the BFS are modelled as walls, therefore, the non-slip condition is applied. The laminar/turbulent transition is triggered at the physical position $x/D^* = -9.02$. Periodic boundary conditions are applied in the spanwise direction. To save computational resources only half of the model in the y-direction is simulated exploiting the axisymmetrical geometry. The zonal boundary conditions are used at the LES inflow and the RANS outflow (see Fig. 6.13). Due to the RSTG method at the LES inflow, the fluctuations are artificially produced and propagate downstream over the backward facing step. The BFS region is important and, therefore, it has to be sufficiently resolved to investigate the small scales of turbulent motions using the LES method. As a result, the BFS region is simulated by an LES, while the front body region where the flow is attached is computed using RANS.

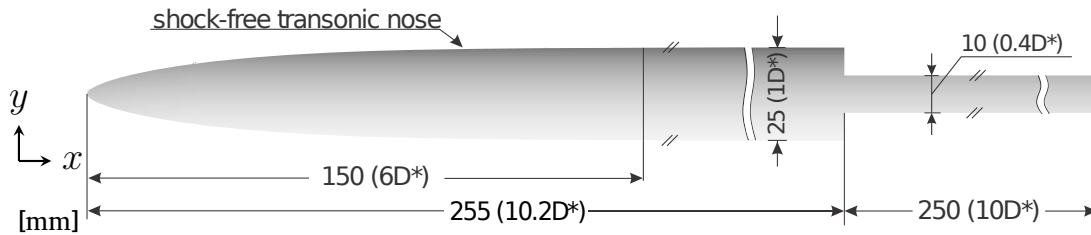


Figure 6.12: Geometry parameters of the investigated generic space launcher configuration [54].

The simulation is conducted on the supercomputer at the Stuttgart High Performance Computing Center using the CRAY XC40 system with a peak performance of 7.42 Petaflops. In this work 50 nodes of the super computer with 24 cores/node are used. For the inflow conditions, a trajectory stage at $Ma_\infty = 0.8$ is prescribed for which strongest buffet loads have been measured on the VULCAIN-2 engine of a full-scale Ariane 5 launcher during the flight [55]. To save the computational costs, the zonal exchange

6.2 Space launcher simulation

Parameter	Value
Ma_∞	0.8
Re	430,000
Pr	0.7
Pr_t	0.9
CFL	1.6
Number of eddies N	600
Zonal exchange interval(timesteps)	50

Table 6.3: Input parameters of the space launcher.

interval should be as long as possible, but also short enough to capture the pressure oscillations that lead to the buffeting phenomenon. The interval was set to 50 timesteps in this simulation. The input parameters for the simulation are summed up in Tab. 6.3.

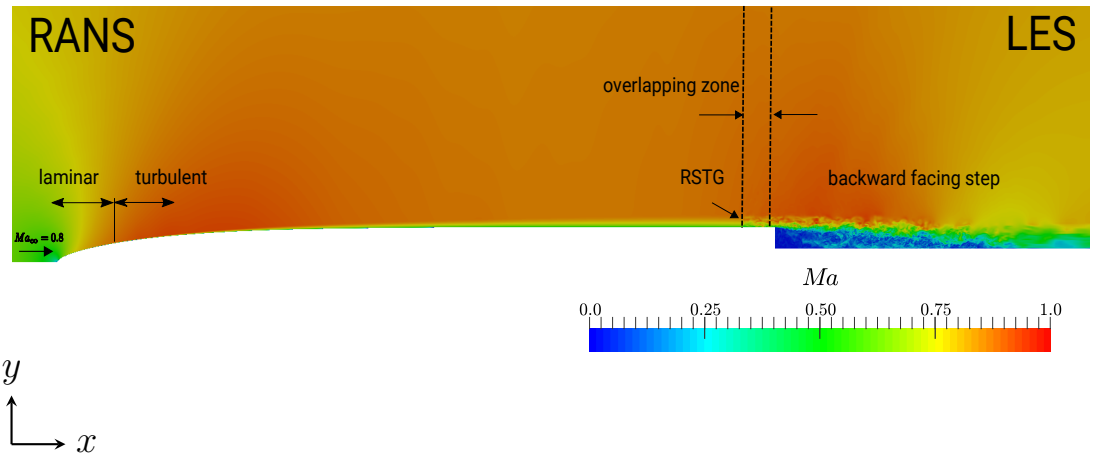


Figure 6.13: Mach number field of the space launcher using the newly implemented zonal RANS-LES method.

Computational grid

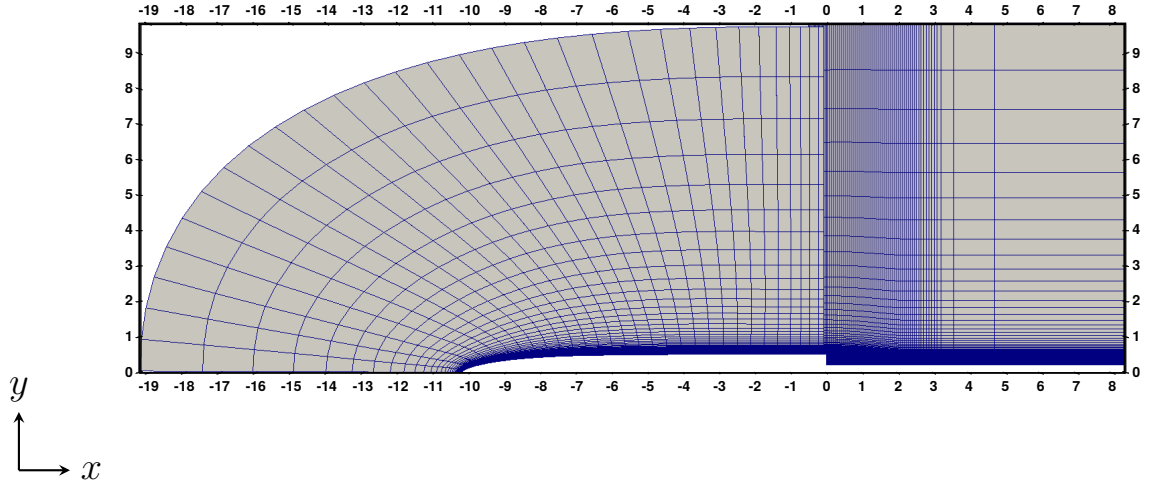
The computational grid is based on the simulation performed by Statnikov *et al.* [54]. The whole computational domain is composed of a RANS grid capturing the flow around the main body and an LES grid for the wake (see Fig. 6.13). In this simulation, the thickness of the main body, D^* is used as a reference length. The RANS zone reaches about $x/D^* = 10.5$ from the front of the main body wall in the wall-normal direction using a curvilinear grid. The end in the streamwise direction of the RANS domain is located at $x/D^* = -0.05$ near the base shoulder (see Fig. 6.15). The backward facing

6. RESULTS

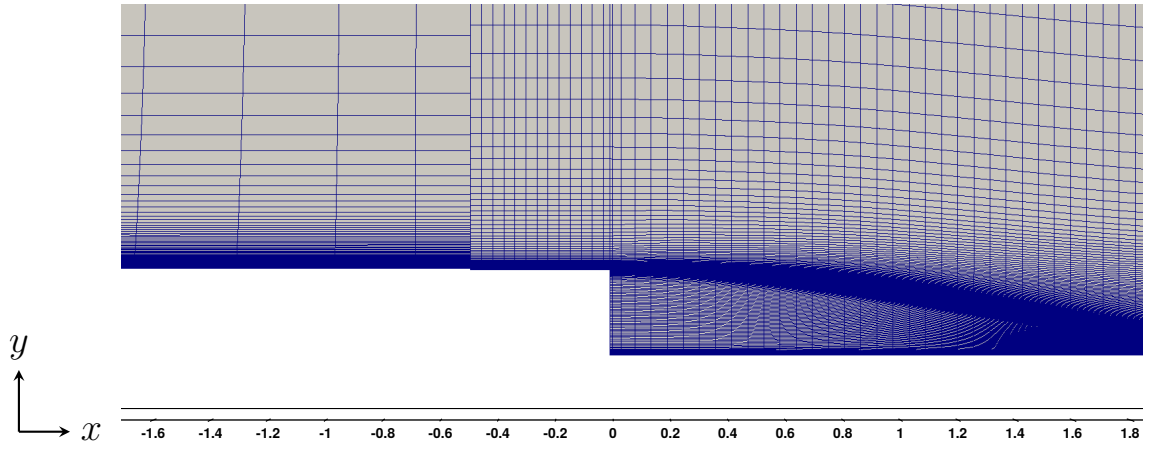
step is located at $x/D^* = 0$. The LES zone extends from $x/D^* = -0.5$ to $x/D^* = 10$ in the streamwise direction and from the surface of the launcher to $x/D^* = 10.5$ in the wall-normal direction. The overlapping zone for the zonal method is positioned from $x/D^* = -0.5$ to $x/D^* = -0.05$ and the overlapping length is $x/D^* = 0.45$. The boundary layer thickness at the backward facing step edge is $\delta = 0.15D^*$. Therefore, a sufficient transition length for a fully developed turbulent flow as required by the RSTG method exists. The spanwise extension of the computational mesh is $z = 0.3D^* = h$, with $h = 0.3D^*$, being the height of the backward facing step. The grid information for each zone is summed up in Table 6.4. In Fig. 6.14a the RANS zone is shown in the overlapping zone, whereas the LES zone is depicted in front of the RANS zone for the overlapping region in Fig. 6.14b.

Zone	Type	Number of Cells			
		i	j	k	Total
Main body	RANS	469	133	17	1,060,409
Backward facing step (wake)	LES	1084	290	402	38,018,748

Table 6.4: Mesh size overview for the computational domain of the space launcher.



(a) Full computational domain



(b) Overlapping zone closed up

Figure 6.14: Computational grid setup for the planar configuration; every 15th grid point only in streamwise direction is shown.

6. RESULTS

6.2.2 Validation of the Zonal RANS-LES method

In this work two different simulations of the same configuration are used to validate the newly implemented zonal RANS-LES method. In the previous simulation ("old"), almost the same numerical methods are used, embedded into TFS (old solver). The main differences are a different numerical dissipation factor of the AUSM scheme in the simulations, and the spanwise extension that is one step height in the new simulation, compared to four step heights in the old setup. Furthermore, the variables of the old solution are computed in the cell nodes, whereas the new solution computed with ZFS is cell centered.

Instantaneous flow field generated by the RSTG method

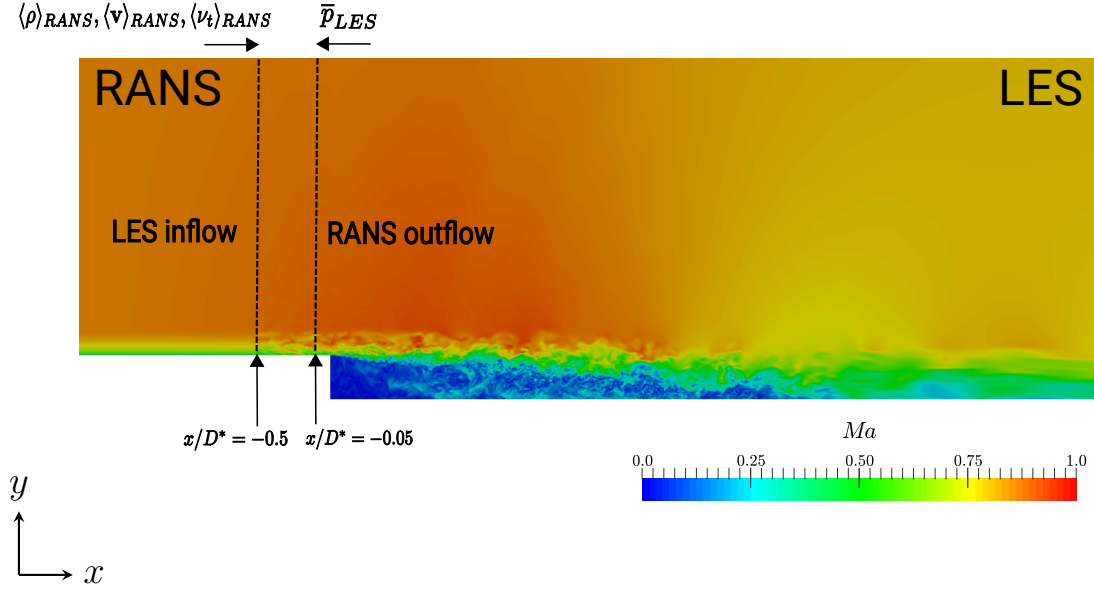


Figure 6.15: Instantaneous Mach number contour of the space launcher around the LES inflow. The backward facing step is located at $x/D^* = 0$.

Fig. 6.15 shows the Mach number contour around the base shoulder. Due to the characteristic of the RANS simulation, time-resolved structures can not be observed in the RANS zone. In contrast, the fluctuations of the LES inlet are generated by the RSTG method [56], superimposing virtual eddy cores which are artificially created in a virtual volume V_{virt} . At the backward facing step further downstream the flow is separated, and a turbulent shear layer sheds from the BFS step. The turbulent shear layer grows further downstream due to turbulent mixing effects and reattaches on the lower wall. At

the reattachment position a part of the shear layer is moving upstream realigning in a recirculation region downstream of the BFS.

6. RESULTS

Mean wall pressure coefficient

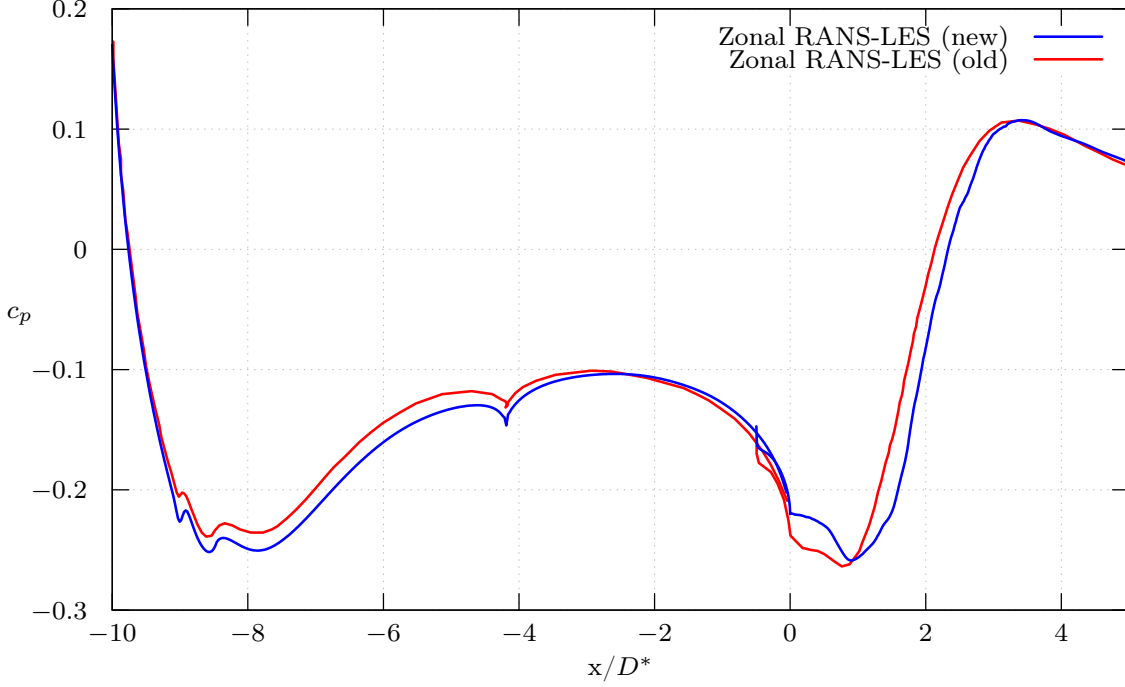


Figure 6.16: Distribution of the mean wall pressure coefficient.

In the following, the wall pressure coefficient $c_p = \frac{p-p_\infty}{\frac{1}{2}\rho_\infty u_\infty^2}$ given in Fig. 6.16 for the two simulations is investigated. There is a good overall agreement between the two solutions, showing only small derivation, except for the wake region ($0 < x/D^* < 3$). This derivation of the wake region might result from that the new solution does not sufficiently consider the three-dimensional effects, due to the smaller spanwise extension (see sec. 2.4). However, the gradient of the plots are similar and the abrupt decline of the c_p value around the point $x/D^* \approx -4$ is well captured in both plots, resulting from the contour jump that changes the gradient of the surface of the launcher's body. This level of discrepancy is within an acceptable range for the comparison of the two simulations. The downstream area of the BFS edge, i.e., $x/D^* > 0$, is an interesting region which is characterized by the buffeting problem. This region needs to be investigated in more details in future work using the newly implemented zonal method.

Skin friction coefficient

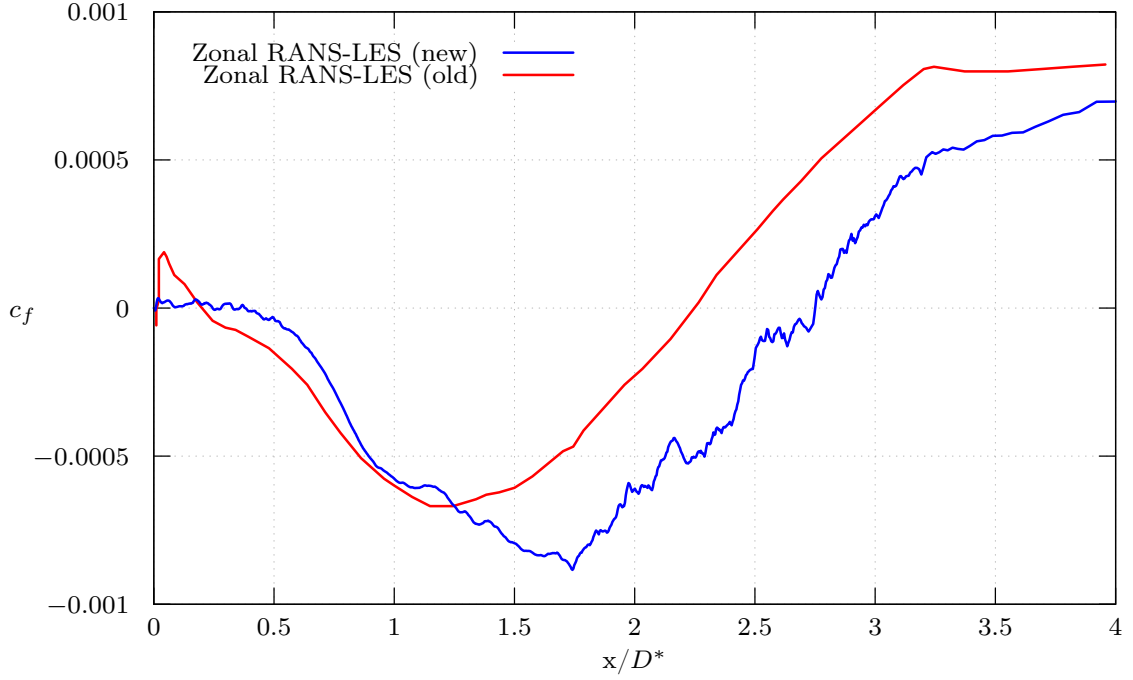


Figure 6.17: Streamwise development of the skin friction coefficient on the lower wall.

The skin friction coefficient distribution allows to quantify the reattachment length and to locate the recirculation zone in the BFS flow. Fig. 6.17 exhibits the streamwise development of the skin friction coefficients along the BFS, i.e., $x/D^* \geq 0$.

The old solution shows a steep increase of the c_f value at $x/D^* = 0$, whereas the new solution exhibits only small positive values. The secondary recirculation zone, indicated by the positive c_f -value directly downstream at the BFS, is well developed in the old solution, between $0.01 < x/D^* < 0.2$. However, in the new solution, it is not certain identifiable. The reattachment can be observed by the zero crossing of the c_f -value. The reattachment length is $x/D^* = 2.75$ in the new solution, whereas the old solution shows a value of $x/D^* = 2.175$. This difference between the two simulations might result from the different numerical dissipation value in the AUSM scheme, which is limited to a maximum of $\chi = 1/64$ in the new solution, an $\chi = 1/128$ in the old solution (see eq. 4.24). Therefore, the solutions might show a slight discrepancy of the streamwise distribution of the skin friction coefficient.

The c_f values downstream of the reattachment zone gradually increase in both cases. Downstream of the reattachment point a new sub-boundary layer is developed within the reattachment zone. The new solution is within an acceptable agreement for a validation of the newly implemented zonal method. For a future work, the simulation using the

6. RESULTS

new zonal method needs to be performed with a smaller numerical dissipation factor χ decreasing the numerical damping.

Velocity fluctuations

Fig. 6.19, Fig. 6.20 and Fig. 6.21 show the velocity fluctuation distributions in the wall-normal direction at different streamwise positions (see Fig. 6.18). In general, the behavior of the velocity fluctuations u'_{rms} , v'_{rms} and w'_{rms} of the new solution shows a very similar tendency compared to the old solution. However, it can be observed that a quantitatively distinct difference between the new and old solution exists. Especially, a significant discrepancy in the area below one step height, i.e., $y/h < 1$, can be recognized, whereas no big differences occur in the region above one step height $y/h > 1$. Note that the discrepancies of the two solutions above one step height are getting larger further downstream of the BFS in all shown components as visible in Fig. 6.19, Fig. 6.20, and Fig. 6.21. This can be caused by the different numerical damping effect in the lower wall region after the flow is separated from the shear layer.

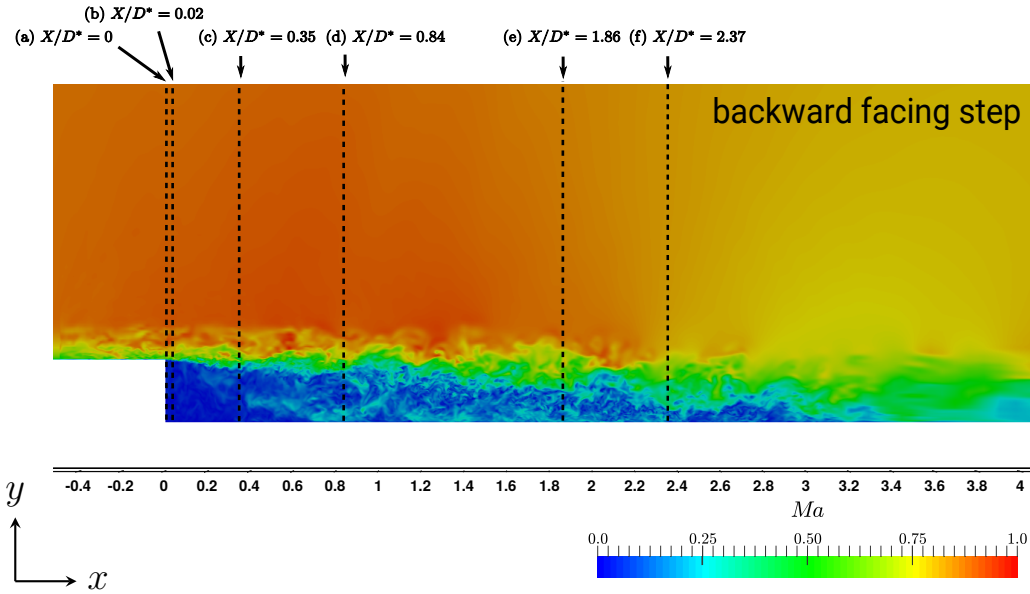


Figure 6.18: Investigated streamwise different locations along the BFS in a Mach number field for the following plots.

The numerical dissipation of the inviscid flux term accumulates after the flow separation. Furthermore, a larger difference of the component w'_{rms} just downstream of the BFS, i.e., $x/D^* = 0$ and $x/D^* = 0.02$, below one step height ($y/h < 1$) can be seen in

Fig. 6.21a and Fig. 6.21b. This large discrepancy might be caused by the three dimensional effects that are not sufficiently resolved in the spanwise direction by the new solution (see sec. 2.4). Yet, due to the good agreement of the velocity fluctuations above one step height for all of the three components with the old solution, it can be concluded that the new developed zonal exchange technique allows to investigate the backward facing step flow.

6. RESULTS

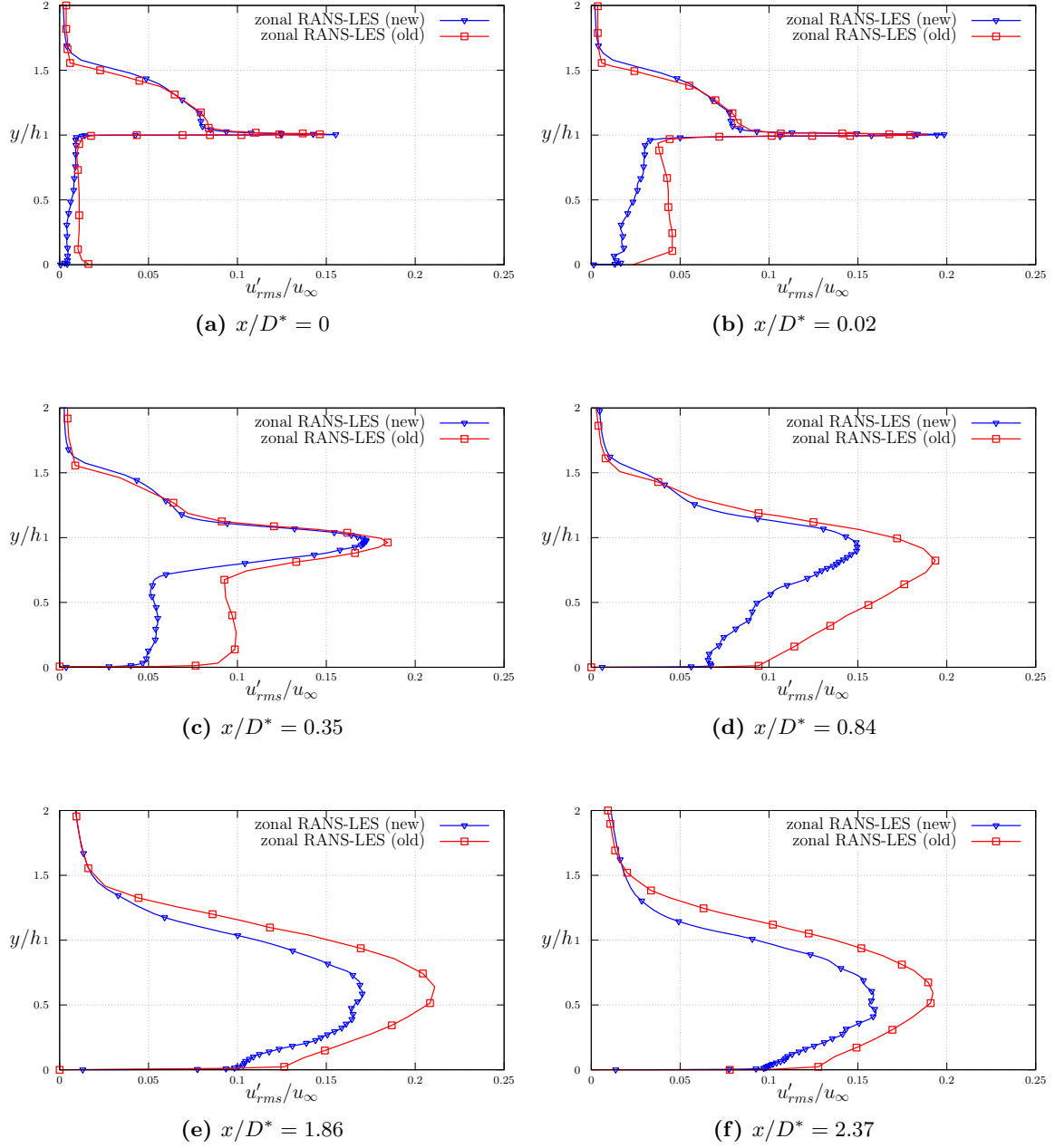


Figure 6.19: Distribution of velocity fluctuation component u'_{rms} in wall-normal direction at different streamwise positions.

6.2 Space launcher simulation

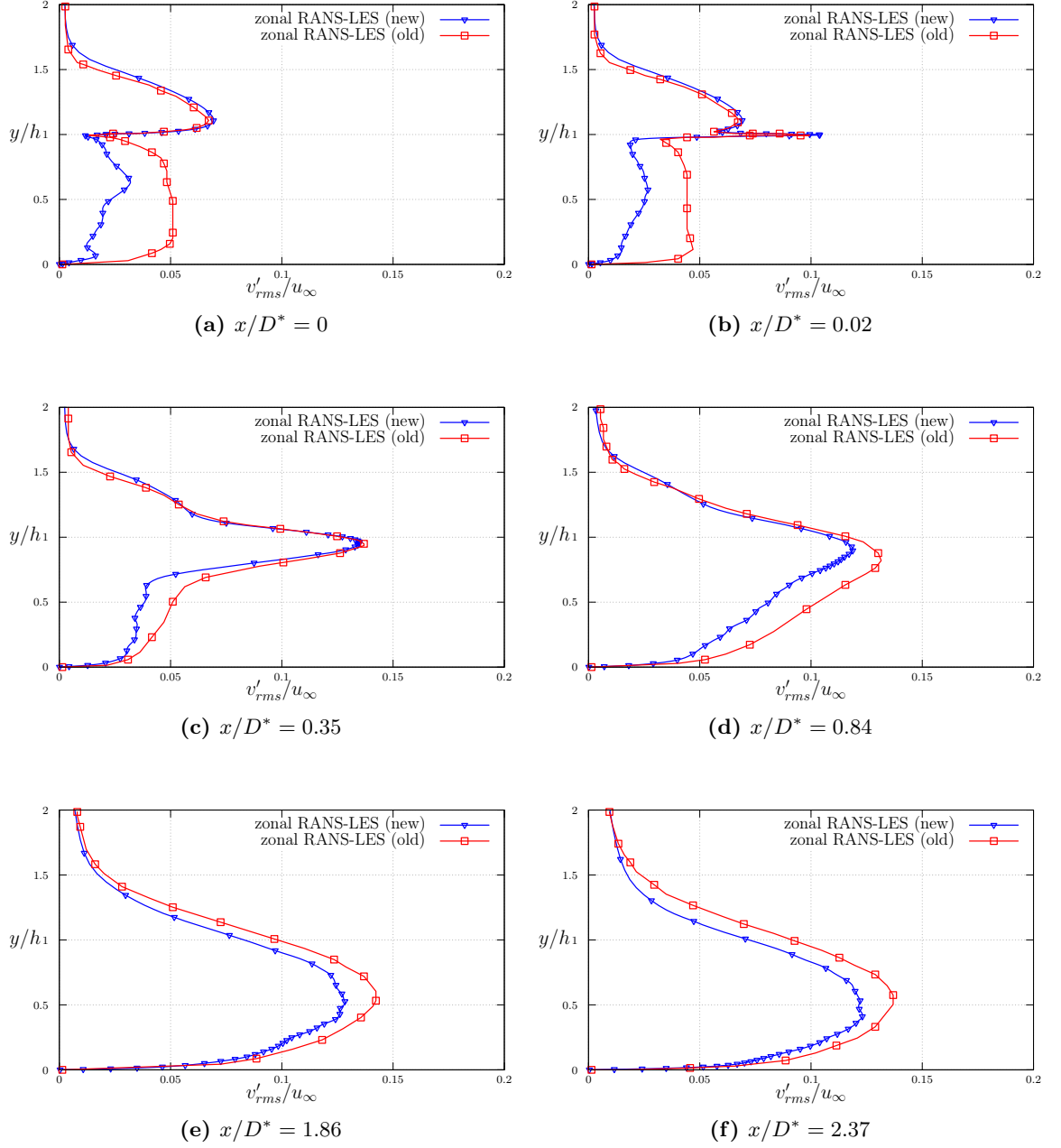


Figure 6.20: Distribution of velocity fluctuation component v'_{rms} in wall-normal direction at different streamwise positions.

6. RESULTS

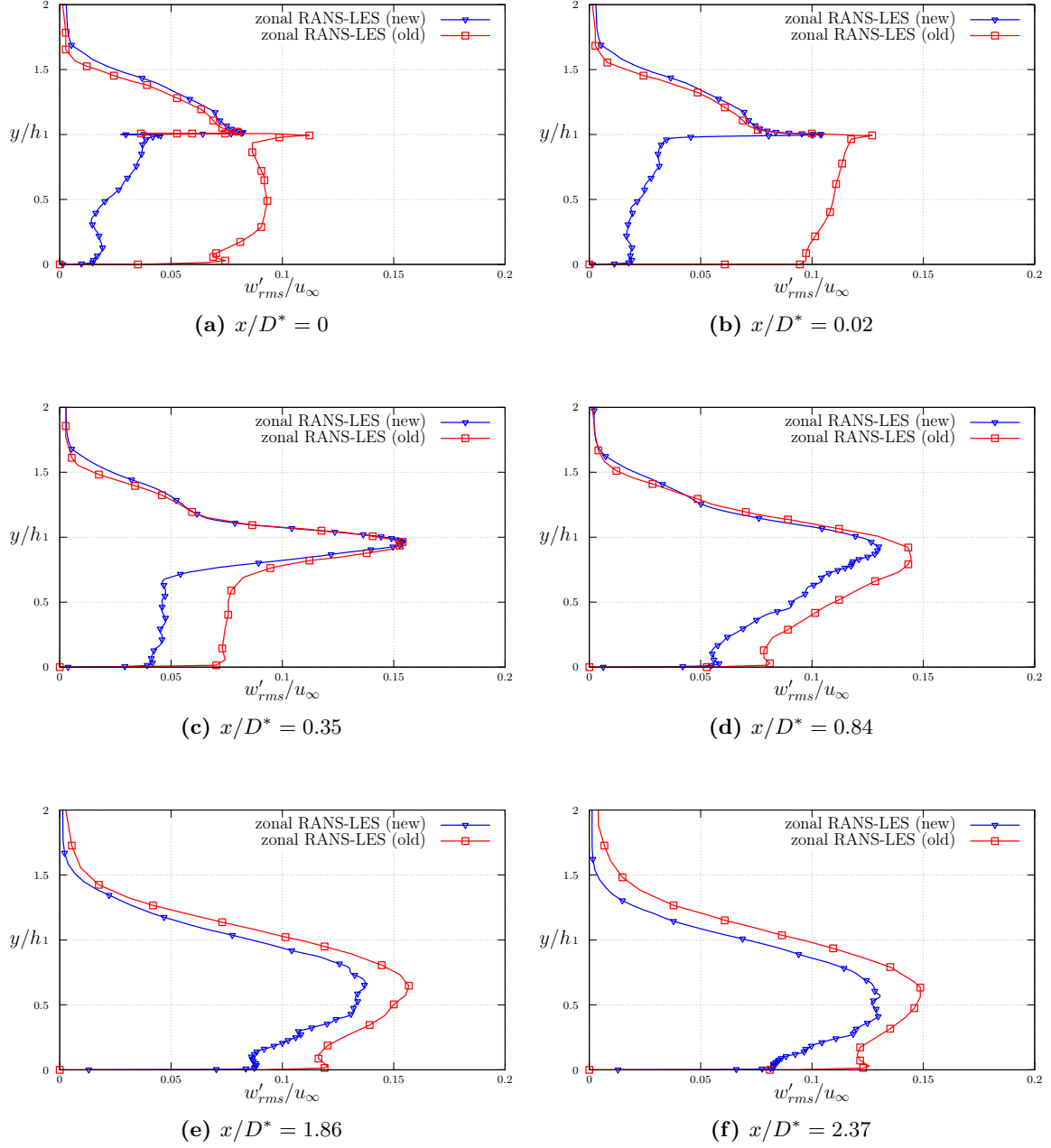


Figure 6.21: Distribution of velocity fluctuation component w'_{rms} in wall-normal direction at different streamwise positions.

Rms pressure fluctuation coefficient

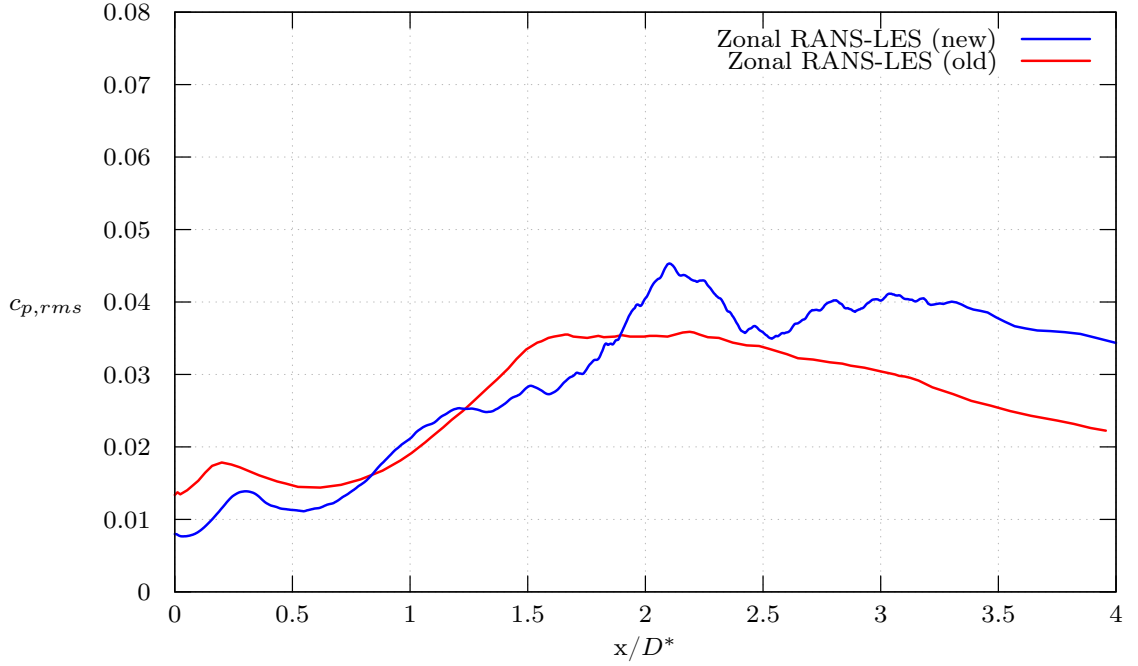


Figure 6.22: Streamwise development of the root-mean-square pressure fluctuation coefficient distribution on the lower wall.

The root-mean-square value of the pressure fluctuation coefficient $c_{p,rms} = \frac{\bar{p}'}{\frac{1}{2}\rho_\infty u_\infty^2}$ plays an important role for the dynamic loads on the wall. In Fig. 6.22 the streamwise development of the $c_{p,rms}$ value on the lower wall downstream of the BFS is presented. Overall, the two solutions have only small discrepancies. However, a larger difference is visible downstream of $x/D^* > 1.86$. Fig. 6.23 shows the $c_{p,rms}$ in the wall-normal direction at different streamwise positions. Until the point $x/D^* = 2.37$, the behavior of the pressure fluctuations for the new solution is in good agreement with the results of the old solution. It can be seen that the new solution allows a validation of the zonal method. Nevertheless, to evaluate the newly implemented method more accurately, the simulation has to be repeated with the same spanwise extension of the grid and an identical numerical dissipation factor χ in the ASUM scheme.

6. RESULTS

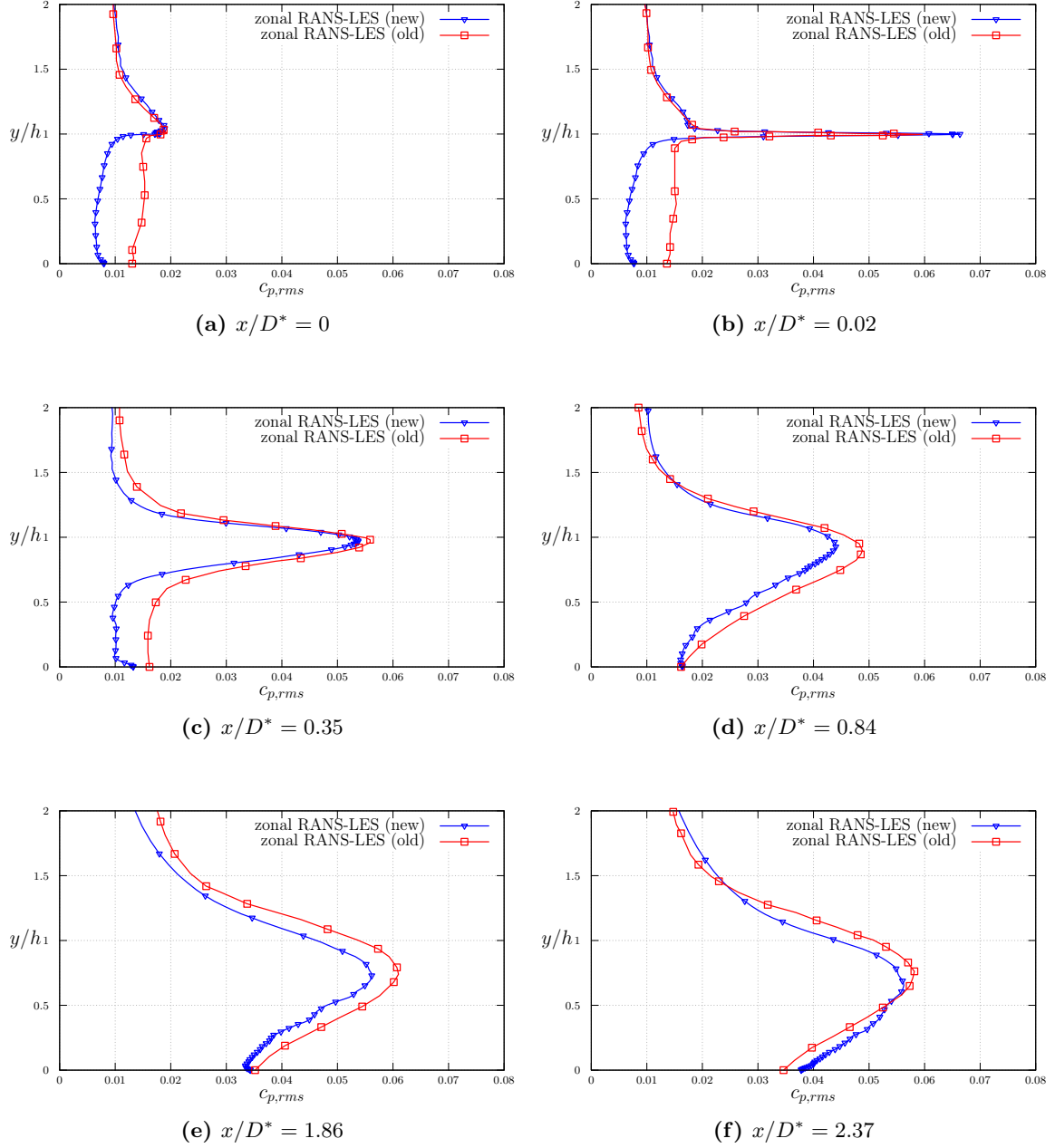


Figure 6.23: Distribution of the pressure fluctuation coefficient in wall-normal direction at the different streamwise positions.

Momentum thickness

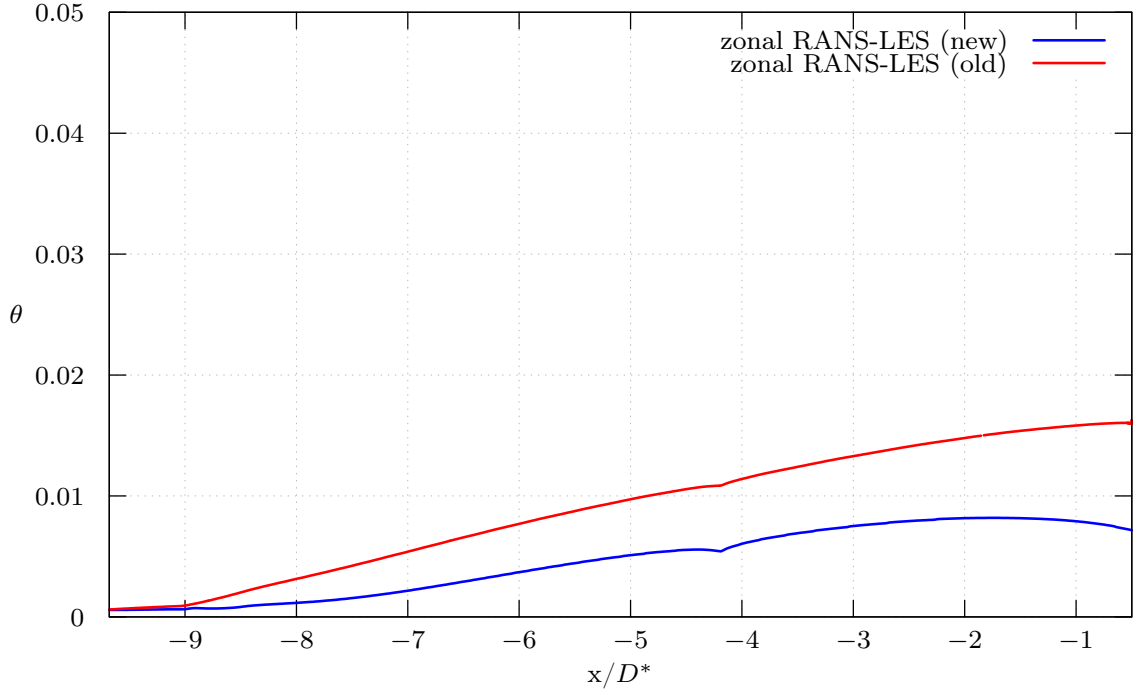


Figure 6.24: Development of the momentum thickness in the RANS zone.

The streamwise development of the momentum thickness is investigated in Fig. 6.24. The specific region in the RANS zone ($-9 < X/D^* < -3$) is an interesting part which has the discrepancy of the pressure coefficient of two solutions (see Fig. 6.16). Downstream of the transition point into turbulent flow, i.e., around the point $X/D^* \approx -9$, the boundary layer of the old solution grows higher in the downstream direction. This might be caused by the bigger spanwise extension, since spanwise turbulent structures can influence the increase of the streamwise velocity. This effect should be investigated more for a future work. Nevertheless, the different momentum thickness is not largely influential to validate the zonal method.

6. RESULTS

Summary and conclusion

In this thesis, a fully coupled simulation of a backward facing step flow is performed using a zonal RANS-LES method for compressible viscous flows at high Reynolds numbers. After the physical characteristics of turbulence are briefly reviewed, the governing equations and mathematical models of the fluid flow are derived. To discretize the mathematical formulations the numerical methods are applied. The zonal boundary conditions at the RANS-to-LES transition and the used RSTG method are described in detail. The zonal variable exchange is developed using the trilinear interpolation which allows to connect the overset meshes between different grid resolutions. For a massive parallel computing with multiple zonal interfaces the zonal exchange procedure is developed. The developed zonal method is applied to a flat plate test case to validate the zonal method, compared to a pure RANS and a pure LES. Then, a space launcher case is simulated and the outcomes are compared to a previous simulation using the same method, but a different solver. The zonal flat plate test case for a zero-pressure gradient flow shows a satisfying agreement with the reference data after a transition length of two boundary layer thickness. The BFS flow simulation also allows a validation of the newly implemented zonal method. However, to prove better reliability of the newly developed zonal method for the backward facing step flow, the simulation has to be repeated with the identical conditions as in the reference configuration. The fully-coupled zonal method implemented newly in this thesis is a continuing work, based on a previous task. The backward facing step investigation is conducted to see the wide-ranging capabilities for a more challenging test case. In the future, the implemented method can be used to simulate much more complex flows including multiple RANS and LES zones.

7. SUMMARY AND CONCLUSION

References

- [1] Q. Zhang, W. Schröder, and M. Meinke. A zonal rans-les method to determine the flow over a high-lift configuration. *Computers & Fluids*, 39(7):1241–1253, 2010. 1, 41
- [2] B. Roidl. A zonal method to efficiently simulate viscous flows. *Ph.D. thesis, RWTH Aachen*, 2012. 1, 3, 8, 30, 35, 43, 45, 46
- [3] Chiu, Jeng-Jiann, Chien, and Shu. Effects of Disturbed Flow on Vascular Endothelium: Pathophysiological Basis and Clinical Perspectives. *Physiological Reviews*, doi:10.1152/physrev.00047.2009. ISSN 0031-9333. PMC 3844671 PMID 21248169(91):327–387. 1
- [4] J.Meiss. Numerical Investigation of Nozzle-Base-Flow Interaction of a Generic Space Vehicle. *Ph.D. thesis, RWTH Aachen University*, 2009. 2
- [5] J. Slotnick, A. Khodadoust, J. Alonso, D. Darmofal, W. Gropp, E. Lurie, and D. Mavriplis. Vision 2030 CFD study: a path to revolutionary computational. *NASA & CR*, (218178), 2014. 2
- [6] H. Tennekes and J. Lumley. A first course in turbulence. *MIT Press*, 1972. 6, 13
- [7] A. N. Kolmogorov. The local structure of turbulence in incompressible viscous fluid for very large Reynolds numbers. *Proceedings of the Royal Society of London*, (434):9–13, 1991. 6
- [8] S. B. Pope. Turbulent Flows. *Cambridge University Press*, volume 7, 2000. 7, 36
- [9] G. I. Taylor. Statistical theory of turbulence. *Proceedings of the Royal Society of London. Series A, Mathematical and Physical Sciences*, (151):421–444, 1935. 7
- [10] T. Cebecci and P. Bradshaw. Momentum transfer in boundary layers. *Hemisphere(McGraw-Hill)*, 1977. 9
- [11] J. Rajasekaran. On the flow characteristics behind a backward-facing step and the design of a new axisymmetric model for their study. *Master thesis, University of Toronto*, 100.1:32–74, 2011. 10
- [12] D. M. Driver, H. L. Seegmiller, and J. G. Marvin. Time-dependent behaviour of a reattaching shear layer. *AIAA Journal*, vol. 25(no. 7):914–919, 1987. 10
- [13] J. K. Eaton and J. P. Johnston. A review of research on subsonic turbulent flow reattachment. *AIAA Journal*, vol. 19:1093–1100, 1981. 10, 11
- [14] E. W. Adams and J. P. Johnston. Effects of the separating shear layer on the reattachment flow structure part 1: Pressure and turbulence quantities. *Experiments in Fluids*, vol. 6:400–408, 1988. 11
- [15] K. Isomoto and S. Honami. The effect of inlet turbulence intensity on the reattachment process over a backward-facing step. *Journal of Fluids Engineering*, vol. 111:87–92, 1989. 11
- [16] M. V. Ötügen. Expansion ratio effects on the separated shear layer and reattachment downstream of a backward-facing step. *Experiments in Fluids*, vol. 111:273–280, 1991. 11
- [17] J. J. Kim. Investigation of separation and reattachment of a turbulent shear layer: flow over a backward-facing step. *PhD thesis, Stanford University*, 1978. 11
- [18] V. Statnikov. Numerical analysis of space launcher wake flows. *Ph.D. thesis, RWTH Aachen*, pages 34–36, 2016. 11
- [19] W. Sutherland. The viscosity of gases and molecular force. *Philosophical Magazine*, 36:507–531, 1893. 16
- [20] A. Leonard. Energy cascade in Large-eddy simulations of turbulent fluid flows. *Advances in geophysics*, 18:237–248, 1975. 19
- [21] A. Favre. Equations des gaz turbulents compressibles. *Journal de Mécanique*, (4):361–390, 1965. 19
- [22] A. Favre. Turbulence: Spacetime statistical properties and behavior in supersonic flows. *Physics of Fluids*, (26):2851–2863, 1983. 19
- [23] O. Reynolds. On the extent and action of the heating surface of steam boilers. *International Journal of Heat and Mass Transfer*, 3(2):163–166, 1961. 21
- [24] S. Hamdi, W. Schiesser, and G. Griffiths. Method of lines. *Scholarpedia*, 2(2859):7, 2007. 25
- [25] D. Hartmann, M. Meinke, and W. Schröder. A strictly conservative cartesian cut-cell method for compressible viscous flows on adaptive grids. *Computer Methods in Applied Mechanics and Engineering*, 9-12(200):1038–1052, 2011. 26
- [26] H. Viviand. Conservation forms of gas dynamic equations. In *its Aerospace Research, Bi-monthly Bull*, pages No. 1974–1 (ESRO-TT-144) p 153–159 (SEE N75–29988 20–99) Transl. into ENGLISH from La Rech. Aerospatiale, Bull. Bimestriel (Paris), no. 1974–1, Jan.– Feb. 1974 p 65–66. Vol. 1974. 1975., 1974-1. 29
- [27] M. Vinokur. Conservation equations of gasdynamics in curvilinear coordinate systems. *Journal of Computational Physics*, 14(2):105–125, 1974. 29
- [28] M. S. Liou and J. C. J. Steffen. A new flux splitting scheme. *Journal of Computational Physics*, (107):23–39, 1993. 30, 32
- [29] B. van Leer. Flux-vector splitting for the Euler equations. *Technical report, Leiden University Observatory, Leiden, The Netherlands*, 1982. 30
- [30] P. L. Roe. Approximate Riemann solvers, parameter vectors, and difference schemes. *Journal of Computational Physics*, 1981. 30

REFERENCES

- [31] B. van Leer. Towards the ultimate conservative difference scheme. v. a second-order sequel to godunov's method. *Journal of Computational Physics*, (32):101–136, 1979. 32
- [32] M. Meinke. Numerische Lösung der Navier-Stokes-gleichungen für instationäre Strömungen mit Hilfe der Mehr-gittermethode. *Ph.D. thesis, Institute of Aerodynamics, RWTH Aachen University*, 1993. 33
- [33] P. S. Meysonnat. Numerical Investigation of Friction Drag Reduction by Spanwise Traveling Surface Waves. *Ph.D. Thesis, RWTH Aachen*, page 33, 2017. 34
- [34] A. Jameson, W. Schmidt, and E. Turkel. Numerical solution of the Euler equations by finite volume methods using Runge-Kutta time-stepping schemes. *AIAA*, pages 81–1259, 1981. 34
- [35] R. Courant, K. Friedrichs, and H. Lewy. Über die partiellen differenzengleichungen der mathematischen physik. *Mathematische annalen*, 100.1:32–74, 1928. 35
- [36] J. Smagorinsky. General circulation experiments with the primitive equations. *Monthly Weather Review*, 3(91):99–164, 1963. 35
- [37] J. Bardina, J. H. Ferziger, and W. C. Reynolds. Improved Subgrid Scale Models for Large Eddy Simulation. *AIAA Journal*, pages 80–1357, 1980. 35
- [38] J. P. Boris, F. F. Grinstein, E. S. Oran, and R. L. Kolbe. New insights into large eddy simulation. *Fluid Dynamics Research*, 4-6(10):199–228, 1992. 35
- [39] C. Fureby and F. F. Grinstein. Monotonically integrated large eddy simulation of free shear flows. *AIAA Journal*, 5(37):544–556, 1999. 36
- [40] F. F. Grinstein and C. Fureby. Recent progress on miles for high reynolds number flows. *AIAA*, page 134, 2002. 36
- [41] J. Boussinesq. Essai sur la theorie des eaux courantes. *Imprimerie Nationale*, 1877. 36
- [42] F. G. Schmitt. About boussinesq's turbulent viscosity hypothesis: historical remarks and a direct evaluation of its validity. *Comptes Rendus Mecanique*, 335(9-10):617–627, 2007. 36
- [43] P. Spalart and S. Allmaras. A one-equation turbulence model for aerodynamic flows. *30th Aerospace Sciences Meeting and Exhibit*, 1992. 36
- [44] P. R. Spalart. Direct simulation of a turbulent boundary layer up to $\text{Re}_{\theta} = 1410$. *J. Fluid Mech.*, 1(187):61, 1988. 39, 45, 48
- [45] J. Fröhlich and D. v. Terzi. Hybrid LES/RANS methods for the simulation of turbulent flows. *Progress in Aerospace Sciences*, (44):349–377, 2008. 43
- [46] M. P. Simens, J. Jimenez, S. Hoyas, and M. Y. A high-resolution code for a turbulent boundary layers. *Journal of Computational Physics*, 228:4218–4231, 2009. 45
- [47] N. Jarrin, S. Benhamadouche, D. Laurence, and R. Prosser. A synthetic-eddy-method for generating inflow conditions for Large-eddy simulations. *International Journal of Heat and Fluid Flow*, 585-593(27), 2006. 45
- [48] M. Pamies, P.-E. Weiss, E. Garnier, S. Deck, and P. Sagaut. Generation of synthetic turbulent inflow data for large eddy simulation of spatially evolving wall-bounded flows. *Physics of Fluids*, 045103(16), 2009. 45
- [49] P. Bradshaw, D. H. Ferriss, and N. P. Atwell. Calculation of boundary-layer development using the turbulent energy equation. *Journal of Fluid Mechanics*, 28(03):593, 1967. 46
- [50] S. Pirozzoli. On the size of the energy-containing eddies in the outer turbulent wall layer. *Journal of Fluid Mechanics*, pages 521–532, 2012. 47
- [51] J. A. B. Calspan, J. L. Steger, F. C. Dougherty, and P. G. Bunting. Chimera: A Grid-Embedding Technique. *Arnold engineering development center*, page Appendix B, 1986. 49
- [52] P. Schlatter and R. Orlu. Assessment of direct numerical simulation data of turbulent boundary layers. *Journal of Fluid Mechanics*, 659:116–126, 2010. 62, 66, 67, 68, 69, 72
- [53] H. Schlichting. Boundary-layer theory. *New York: McGraw-hill*, Vol. 7:1093–1100, 1960. 68
- [54] V. Statnikov, I. Bolgar, S. Scharnowski, M. Meinke, C. J. Kaehler, and W. Schröder. Analysis of characteristic wake flow modes on a generic planar transonic space launcher configuration. *Annual Report*, 2015. 74, 75
- [55] D. C. and R. S. Prediction of buffet loads on the Ariane 5 afterbody. *6th International Symposium on Launcher Technologies Munich. CNES*, 2005. 74
- [56] B. Roidl, M. Meinke, and W. Schröder. Reformulated synthetic turbulence generation method for a zonal rans-les method and its application to zero-pressure gradient boundary layers. *Int. J. Heat Fluid Flow*, 44:28–40, 2013. 78

Appendix A

Reference Values

All of the variables should be non-dimensionalized using the reference value of the stagnation point. That is, the flow problems have different magnitude of values in terms of the relativity and many variables are used with various physical units. Therefore, by means of a non-dimensionalization variables can be independent from situations and the number of the related parameter decreases. Moreover, the orders of the variables are often manifold, which can be conducted numerical analysis inefficiently. For these reasons, a non-dimensionalization is necessary to enhance the speed of a calculation and a fidelity of numerical schemes. The normalized, no-dimensional variables are introduced, denoted by $(\cdot)^*$, such that,

$$\begin{aligned} \mathbf{x} &= \frac{\mathbf{x}^*}{L^*}, & t &= \frac{t^*}{\frac{L^*}{a_0^*}}, & \rho &= \frac{\rho^*}{\rho_0^*}, & \mathbf{u} &= \frac{\mathbf{u}^*}{a_0^*}, & T &= \frac{T^*}{T_0^*}, \\ p &= \frac{p^*}{\rho_0^* a_0^{*2}}, & e &= \frac{e^*}{a_0^{*2}}, & \mu &= \frac{\mu^*}{\mu_0^*}, & \lambda &= \frac{\lambda^*}{\lambda_0^*}, & c_{p,v} &= \frac{c_{p,v}^*}{\rho_{p,v}^* a_0^{*2}}, \end{aligned}$$

A. REFERENCE VALUES

where $a_0^* = \sqrt{\gamma_0 R^* T_0^*}$ is the speed of sound and L^* is length of the flat plate of the test case. Using these normalized variables, the characteristic parameters result in

$$\begin{aligned} \text{Reynolds number} \quad Re_0 &= \frac{\rho_0^* u_0^* L^*}{\mu_0^*}, \\ \text{Prandtl number} \quad Pr_0 &= \frac{\mu_0^* c_p^*}{\lambda_0^*}, \\ \text{Strouhal number} \quad Sr_0 &= \frac{L^*}{u_0^* t_0^*}, \\ \text{Mach number} \quad Ma &= \frac{u_0^*}{a_0^*}, \\ \text{Ratio of specific heats} \quad \gamma_0 &= \frac{c_{p0}^*}{c_{v0}^*}. \end{aligned}$$

Declaration

I herewith declare that the present thesis is the result of my own work without the prohibited assistance of third parties and without making use of aids other than those specified; it includes nothing which is the outcome of work done by other authors, unless for commonly understood ideas or where identified to the contrary. This thesis has not previously been presented in identical or similar form to any other institution, German or foreign, for any degree or any other qualification.

Aachen, 5th July 2018